Method for determination of the softening behaviour of wood and the applicability of a nonlinear fracture mechanics model

Boström, Lars

1992

Total number of authors:
1

Method for determination of the softening behaviour of wood and the applicability of a nonlinear fracture mechanics model

Lars Boström

Method for determination of the softening behaviour of wood and the applicability of a nonlinear fracture mechanics model

Lars Boström

Doctoral Thesis, Report TVBM-1012

Lund, Sweden, 1992

This is not the end.
It is not even the beginning of the end.
But it is, perhaps, the end of the beginning.

Sir Winston Churchill
Manison House, London, 10 nov. 1942

Preface

This investigation has been carried out at the Division of Building Materials at the Lund Institute of Technology in Lund, Sweden, under the supervision of Professor Arne Hillerborg. The project has been financially supported by grants from the Swedish Board for Technical Development and the Swedish Council for Building Research.

I wish to express my gratitude to Professor Arne Hillerborg for his invaluable guidance and encouragement during my education and this investigation. I also wish to express my gratitude to his successor, Professor Göran Fagerlund, who always asked odd but valuable questions.

I wish to thank Per Johan Gustafsson, at the Division of Structural Mechanics, for all the answers he has given to all my strange questions. I also wish to thank Professor Sven Thelandersson, at the Division of Structural Engineering, and Professor Hans Petersson, at the Division of Structural Mechanics, for many valuable discussions.

Thanks to my room-mate, Manouchehr Hassanzadeh, at the Division of Building Materials who has a special place in my heart, not only for his encouragement during hard periods of my life, but also for all help during my studies.

I wish to thank my colleagues at the Division, especially Britt Andersson who made all nice drawings, Bo Johansson for the time consuming, and sometimes boring, laboratory work and Bengt Nilsson for his neverending energy in the laboratory and behind the camera.

Finally, I wish to express my gratitude to my family. Thanks Ingrid and Nathalie for all support during this hardworking period of my life.

Lund, February 1992

Lars Boström

1

Contents

Summary

The main objective of this study was to find a method for determination of the softening behaviour of wood, and to show the applicability of the fictitious crack model in theoretical analysis of different structures. The main effort regarding the experimental investigations has been centered on pure tension failure, and to some extent pure shear failure. The theoretical analysis has been exclusively concentrated on tension failure.

A number of fracture mechanics models are briefly presented, and one non-linear model, the fictitious crack model, is more thoroughly described. In the fictitious crack model the softening behaviour is utilized, and this model has also been applied to the theoretical analysis presented.

Wood is a hygroscopic, orthotropic material, i.e. its mechanical properties vary with moisture content and they are different in different directions. Therefore the influence of moisture content and grain orientation has been examined for the pure tension mode. Only one species, Scots pine (*Pinus Sylvestris*), has been examined.

It is shown that the softening behaviour of wood can be measured by means of direct tension or shear tests. However, there are a number of difficulties involved in these experiments.

The size of the specimen has to be very small in order to avoid instabilities during the test.

The specimen is glued into the testing arrangement, and accordingly the choice of glue is important. The glue can affect the results in many ways, for example, if the strength of the glue is too low the glueline will fail and not the wood; if the glue is improperly cured the glue can affect the results (the measured displacements are displacements of the glue and not the wood).

The testing machine and testing arrangement must be very stiff both in translation and rotation direction in order to get a stable test.

In order to show the applicability of the softening behaviour, two examples are presented. The first example is an analysis of the Compact Tension specimen, which is one of the most commonly used specimens for determination of fracture mechanics properties. The second example is a very simplified calculation of the formation of drying cracks in wood, which is a very serious problem in practice.

Notations

All symbols are explained where they first appear. However, some symbols will briefly be presented here.

A	area
A_0	cross sectional area of the fracture process zone
a	length of notch or crack
B	thickness
C	compliance
D	stiffness matrix
d	characteristic size of a structure, for example depth of a beam
E	modulus of elasticity
E_L	modulus of elasticity in the grain direction
E_R	modulus of elasticity in radial direction
E_T	modulus of elasticity in tangential direction
E_{RT}	modulus of elasticity perpendicular to the grain
E^*	orthotropic stiffness
F	mass flow
f_t	tensile strength
f_v	shear strength
G_F	fracture energy
$G_{F,I}$	fracture energy in Mode I
$G_{F,II}$	fracture energy in Mode II
G_I	strain energy release rate, Mode I
G_{IC}	critical strain energy release rate, Mode I
G_{xy}	modulus of rigidity
g	evaporable moisture concentraiton
I	moment on inertia
K_I	stress intensity factor for Mode I
K_{IC}	critical stress intensity factor for Mode I
k	spring constant
l	length
l_{ch}	characteristic length $= EG_F/f_t^2$
m	mass
P	force
RH	relative humidity
S_{nm}	translation stiffness of testing arrangement

S_{rm}	rotational stiffness of testing arrangement
S_{ns}	translation stiffness of specimen
S_{rs}	rotational stiffness of specimen
S_{ntot}	translation stiffness of complete test system including specimen
S_{rtot}	rotational stiffness of complete test system including specimen
t	time
u	moisture content
V	volume
v	widening of fracture process zone in Mode II
v_C	maximum widening of the fracture process zone in Mode II
W	ligament length
w	widening of fracture process zone in Mode I
w_C	maximum widening of the fracture process zone in Mode I
β	diffusion coefficient
γ	shear displacement
Δ	increment
δ	normal displacement
ϵ	strain
ν	Poisson's ratio
ρ	density
σ	tension stress
τ	shear stress
ψ	shrinkage

1 Introduction

Throughout the history of mankind, wood has been a material of vital importance. The field of applications for wood and woodbased products has been very wide. The first constructions in which wood was used as a structural material were probably shelters. Before that, wood had been used for weapons like clubs and spears, and as firewood. Later on, more than three thousand years ago, the Egyptians produced veneers, laminates and paper from wood. Accordingly, wood had and still has a very wide area of applications and is also one of the oldest materials still in use, together with stone and bricks.

Through the years, the use of wood as a structural material has expanded greatly. There were and still are many various types of constructions where wood is the main raw material. Houses, bridges and vehicles for transportation, such as boats, can be mentioned as examples.

Wood has many advantages compared to other materials. It is easily workable, and only small amounts of energy are required to improve it, i.e. it does not pollute as much as many other materials do. Furthermore, it is a beautiful material that certainly should be used in buildings for more than formwork timber.

Timber is dominant in many fields of application. The most important fields for sawn wood as well as for woodbased boards are building, carpentry, furniture and box making industries. Of these the building industry has the greatest demand for wooden products. However, in Sweden, during the past few years other materials have taken parts of the market from wooden products, especially materials like steel, aluminum, plastics and concrete.

Although wood has been used for thousands of years, there still is a great lack of knowledge about the behaviour of wood. The knowledge regarding making use of different species properties such as durability, strength, toughness etc., is insufficient because of neglected research and education in wood technology.

To summarize, there are great needs regarding research in the timber industry, if it is going to keep its share of the market. The products have to be improved, and better knowledge about the material has to be acquired.

One scientific area that has lagged behind in connection with wood, but more and more researchers now find interesting, is fracture mechanics. Why the interest in fracture mechanics has been smaller for applications on wood than for other materials like concrete and metals, is difficult to answer. However, there are a number of possible explanations that may reveal the shortage of research regarding fracture mechanics applied to wood.

Firstly, fracture mechanics is a rather young science. Generally it is said to have been born

by the publication of Griffith (1921), although there are earlier publications, i.e. Inglis (1913). Fracture mechanics was applied to wood during the sixties, especially in Australia where it was utilized in the codes. But universally, fracture mechanics has had no success.

Secondly, fracture mechanics is looked upon by wood researchers and wood scientists as a very theoretical and complicated tool, that only a few understand. And consequently, it cannot be utilized in the design codes. Fracture mechanics is an unexplored field for designers, but it gives the researchers a tool to make new and better codes, that must not necessarily be complicated. By utilizing fracture mechanics, many drastic damages may be prevented, as exemplified by notched glulam beams that have broken under relative low loads.

When a solid body is extremely loaded, it undergoes large deformations and/or fracture. The topic of primary interest in this report is the fracture, which means loss of contact between parts of the body. Today there is no common definition for fracture mechanics, but one which is often found in literature is "the mechanics when new surface areas are formed in a body".

Generally when fracture mechanics is applied to wood, linear elastic fracture mechanics (LEFM) is used. This is apparently the most suitable model today, when working with larger wooden structures. But there are some disadvantages with linear elastic fracture mechanics. The model demands an existing crack or notch, and the fracture process zone has to be small compared to both the thickness of the body, length of the crack propagation path in the body or specimen and length of the crack.

Usually, at least for normal and large sized structures, these disadvantages do not influence the results, but there are cases when linear elastic fracture mechanics cannot be applied. As an example, calculations of the formation of drying cracks in timber can be mentioned. In that case there are no cracks when the drying process starts, and consequently no stress or displacement singularities; hence linear elastic fracture mechanics cannot be employed.

Another case when other models than linear elastic fracture mechanics can be an advantage is when calculations are made on small bodies, like specimens for determination of material properties. Here the fracture process zone can be of such large size that it influences the results if linear elastic fracture mechanics is utilized directly, without modifications regarding the fracture zone.

Since the birth of fracture mechanics, numerous fracture mechanics and other models have been developed that can be used to determine the behaviour of a structure when a crack develops and/or propagates. The models most frequently described in textbooks on fracture mechanics are linear elastic fracture mechanics, and two nonlinear models, the Dugdale model and the J-integral. The Dugdale model, that is a plasticity model, was developed by Dugdale (1960). The J-integral, or Rice integral, which is a non-linear model, was developed by Eshelby (1956) and then further improved by Rice (1968).

2

But there are also other models that were more recently developed. In this report two models which are applicable to wood will be described, the finite small area model, Landelius (1989) and the fictitious crack model, Hillerborg et al. (1976). These models are not yet found in introductory books on fracture mechanics.

The finite small area model, Landelius (1989), calculates a mean stress with linear elastic theory over a certain area and compares this mean stress with the strength of the material. With this model it is possible to make calculations even on structures without any initial cracks.

The model mainly used in this thesis is the fictitious crack model (FCM), which was developed by Hillerborg et al. (1976). The main purpose of the model was to investigate the fracturing process of concrete. However, the model is independent of material, as long as it is a non-yielding material, so it may be a useful tool for calculations on wood, which will be shown later in this thesis.

Before any model can be employed to simulate the behaviour of a body, different properties of the material must be known. These properties are fundamental for the simulation to coincide with the real behaviour of the body. The property concentrated upon here is the complete stress-displacement curve.

1.1 Objective

The main objective of this thesis is to demonstrate an experimental method to study the complete stress-displacement behaviour of wood, and especially the softening behaviour, and to show the applicability of a nonlinear fracture mechanics model, the fictitious crack model. A softening material here is characterized as a material in which, when it is subjected to a monotonous increasing displacement or strain, the stress in the material will increase to a maximum value, thereafter decrease until it is zero and the body is broken.

An extensive experimental series has been carried out to find a suitable experimental setup for determination of the complete stress-displacement relation for wood in pure tension and in pure shear. During the time of the experiments, a number of calculations have been made to show the advantages of the fictitious crack model. Therefore, not all material properties used in the computations presented in Chapters 4 and 5, coincide with the results presented in Chapter 3. However, the objective has not been to provide material properties, but to show a method with which the softening behaviour can be determined, and to show that nonlinear fracture mechanics is a useful tool for fracture predictions.

When fracture mechanics is utilized on wood, the model generally employed is linear elastic fracture mechanics. Therefore, as far as possible, the results obtained have been compared

with linear elastic fracture mechanics.

With a knowledge of the softening behaviour, the fictitious crack model can be applied for simulation of crack formation and propagation in wood. However, the softening behaviour is not the only material property needed for the model. Different stiffness and strength parameters are also material properties that are fundamental for the model. But in this report only the complete stress-displacement curve has been determined, and hence only the parameters fracture energy, tension strength, shear strength and shape of the softening curve. Other properties used here, such as the different stiffness properties, were usually collected in literature. However, from the determined load-displacement curves an approximative modulus of elasticity was determined. This modulus of elasticity was used to calculate the critical stress intensity factor from the determined fracture energy.

A method for direct determination of the softening behaviour of wood is presented. Even if there are great difficulties involved in direct measurements of the complete stress-displacement curve, it is possible with specimens designed for the tests and with a proper experimental setup.

In order to demonstrate theoretical applications where the fictitious crack model is applied, two examples are presented. The first example is a study of the Compact Tension specimen, Chapter 4, which is one of the most widely used experimental methods for determination of fracture mechanics properties of wood, Boström (1990). In addition to the theoretical study an experimental series was made. These experiments were mainly made in order to investigate the size-dependencies of the specimen, but also to determine some of the material properties used in the computations. It should be noted, however, that the material used in these tests is not the same material as the material used in the experiments presented in Chapter 3.

The second example is a simplified study of the formation and growth of drying cracks in wood, Chapter 5. In this study the main effort has been put into the fracture calculations and hence the moisture and shrinkage calculations have been made as simple as possible, Boström (1987a) and Boström (1987b).

To summarize, the ambition of this study has not been to obtain material properties, but to present a method with which the softening behaviour of wood can be determined, and to reveal the applicability of nonlinear fracture mechanics, especially the fictitious crack model.

1.2 Limitations

When experimental studies are made on wood, it is unavoidable to make great limitations. In this experimental study only one species, Scots pine (*Pinus silvestris*), has been examined. Furthermore, when examining the fracture mechanics parameters, there are six different main orientations of the grain direction in relation to the crack, and in addition all orientations in between these six main directions, see Figure 1.1. However, when measuring fracture energy by means of a direct tension test, i.e. the fracture develops simultaneously over the whole cross section, the number of orientations reduces to only three, because the fracture energy is equal in TL and TR, RL and RT and finally LR and LT orientation, i.e. $G_{F,TL}=G_{F,TR}$, $G_{F,RL}=G_{F,RT}$ and $G_{F,LR}=G_{F,LT}$. If the fracture energy is a material property, no differences would be found between measurements in a direct tension test or a test with a propagating fracture. The studies presented in this report are concentrated on the RL and TL orientation, and some experiments have been made in one orientation between RL and TL.
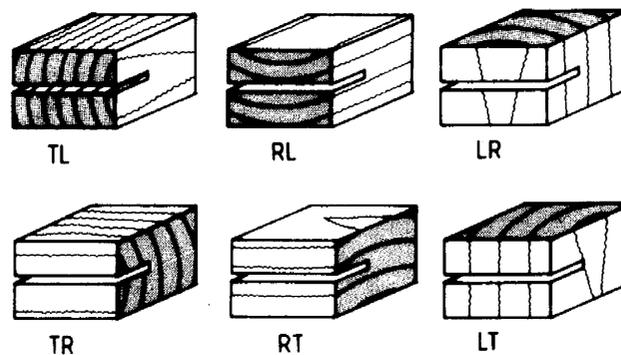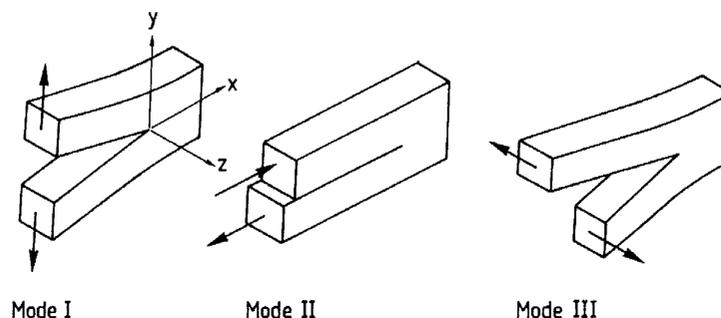
Figure 1.1 Main orientations for wood.

Figure 1.2 Different modes of failure.

5

In addition to this, the failure can occur in three different modes, see Figure 1.2. These three modes represent the pure tension failure, Mode I, the forward shear failure, Mode II, and finally the transverse shear failure, Mode III. And again, there are also failures in between these main modes, the so-called Mixed Mode failures. The main effort has been put into Mode I and Mode II experiments that probably are the most important modes together with the Mixed Mode I & II failure.

Wood is a strongly hygroscopical material, and thus very sensitive to moisture. The mechanical properties of wood change, and sometime dramatically, with changing moisture content. Therefore the effect of moisture content was also investigated to some extent. Specimens were conditioned in four different relative humidities, 33%, 59%, 75% and 97% RH, and thereafter tested. Thus all experiments were made with a moisture content under the fiber saturation point.

It has not been possible to determine the moisture content and density for each specimen, so special specimens were made for these measurements. The reason why neither density nor moisture content was measured on each specimen was the very small size of the specimens. Moreover, the specimens had to be glued in the loading arrangement, and it was impossible after the experiment to remove a specimen from the arrangement without completely destroying it. Therefore special specimens were made in order to measure the moisture content and density of the material.

Another climate factor that may affect the fracture energy, and the shape of the stress-displacement curve, is temperature. However, in this investigation the temperature has been constant at around 20°C during both conditioning and experiment.

All experiments were made on small clear specimens, i.e. all specimens with any defect, such as knot or crack, were excluded from the investigation. A serious problem with the experimental method was the glue used to attach the specimen to the loading arrangement. The glue had to have a sufficient strength in order to transfer the load to the specimen, and different types of glue were examined. Furthermore, no plastic deformations could be allowed in the glueline. Some examples where the glue has influenced the results will be shown. However, in the main results presented, all tests where the glue influenced the result have been excluded.

The time dependency on the material properties has not been considered, either in the experiments or the theoretical calculations. It is well-known that the long-time behaviour of wood is quite different from the short-time behaviour. However, it was not possible in this study to cover the long-time behaviour, and consequently the experiments are fully concentrated on the short-time behaviour.

In the theoretical analysis, only the pure Mode I failure has been taken into account.

6

However, the fictitious crack model can be used for calculations in other modes of failure and also on the Mixed Mode failure. In the present studies, the failure is in Mode I and hence only tension stresses have been analyzed. Furthermore, the material has been assumed homogeneous, i.e. the material has identical properties in all infinitesimal parts.

Because of the strong orthotropic behaviour of wood, the crack propagation path can easily be determined before the calculation. For other materials, like concrete, there can be problems because the crack propagation path is not known, and to get good results, remeshing of the finite element mesh is inevitable. Furthermore, it is always possible that more than one crack forms, and consequently alters the stress distribution. However, in this study it is assumed that only one crack forms, which makes the calculations much easier to carry out.

The material has been assumed to behave linear elastic before fracture, and the stiffness properties used have usually been collected in the literature. No direct measurements of the elastic properties have been carried out, except on the material used in the study of the Compact Tension specimen.

In the calculations the theory of small strains and small global displacements has been adopted and the material has been considered to be in a state of plane stress.

It should, however, be noted that the calculations on the Compact Tension specimen and on the formation and growth of drying cracks were made before most of the experimental results concerning the softening behaviour were complete. Therefore, the softening behaviour was assumed in accordance with the preliminary experimental results, which does not completely coincide with the final results regarding the shape of the stress-displacement curve and the fracture energy. Nevertheless, the theoretical examples do demonstrate the applicability of the fictitious crack model.

Note also, that the material used for determination of the softening behaviour is not the same material as that used for the Compact Tension series.
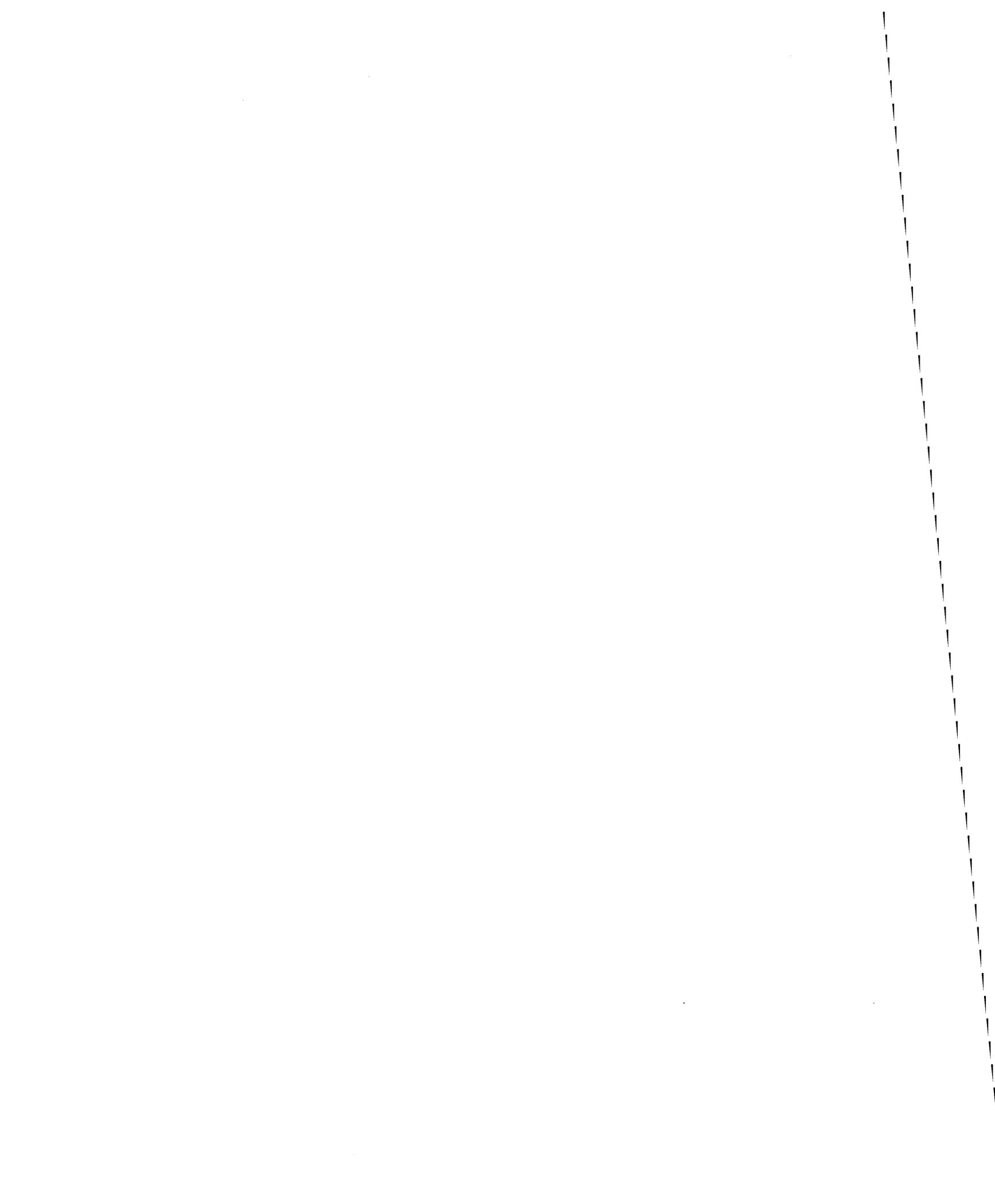
2   Fracture mechanics models

The objective this chapter is to give a brief presentation of different fracture mechanics models used by wood scientists and researchers today. Consequently no complete definitions or derivations of the formulas and equations are given. However, there is one exception, regarding the fictitious crack model, which is more thoroughly described. Nevertheless, there are several publications in which derivations of most of the fracture mechanics formulas can be found, especially concerning the linear elastic fracture mechanics; see for example Hellan (1984) or Knott (1973).

There are plenty of textbooks dealing with fracture mechanics, and especially linear elastic fracture mechanics, for example Carlsson (1976) and Bäcklund (1982). Usually these books are specialized on metals and in a few cases on concrete. There are very few books on fracture mechanics where wood is analyzed. In Bodig and Jayne (1982) there is a brief presentation of fracture mechanics applied to wood.

Usually when fracture mechanics is applied to wood, the linear elastic approach is employed. In fact, the model gives relatively good results in many situations where large structures with cracks are analyzed. However, there are situations where other models have to be applied.

In order to give an insight into some fracture mechanics models suitable for wood, three different models are described. These models today are more or less applied to wood by different researchers. The models described are:
- fictitious crack model (FCM)
- linear elastic fracture mechanics (LEFM)
- finite small area theory (FSAT)

Of these models linear elastic fracture mechanics and finite small area theory are linear elastic approaches, while the fictitious crack model is a nonlinear model. However, since finite small area theory is a mixture of linear elastic fracture mechanics and conventional stress criteria it can be applied on structures without singularities.

2.1   Introduction to fracture mechanics

Even if the science of fracture mechanics is not widely known, the phenomenon of stress concentrations is. For instance, when a piece of cloth is to be torn apart, a small notch is usually made, with for example scissors. By making a small notch, the cloth can be easily torn apart. This very familiar example is a typical fracture mechanics application.
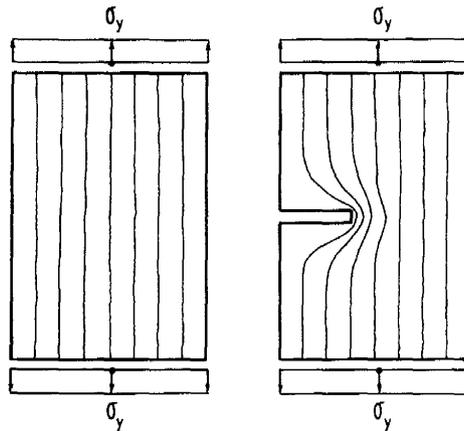
Figure 2.1 Stress-lines in a body without a notch and in a body with a notch.

By introducing a notch in the material, the stress distribution in the material will be changed. There will be stress concentrations around the notch, i.e. stresses around the notch will be much higher than in other parts of the material, see Figure 2.1. Therefore, the applied load necessary to reach failure is much smaller for a body with a notch than for a body without a notch.

If a material is considered linear elastic, and isotropic, and an infinitely large plate of this material is subjected to a uniform tensile stress σ_y, the stress distribution will naturally be even, equal to σ_y. But if a hole is made in the plate, the stress distribution will be disturbed. Figure 2.2 shows a plate with a circular hole, an elliptical hole and a crack. For a circular hole the stress will reach three times the applied stress at the most critical point of the hole, i.e. $\sigma = 3\sigma_y$, regardless of the size of the hole. Consequently, if irregularities exist in the material, the strength of the material will be considerably reduced.

A circular hole can be considered as an ellipse with the major and minor axis equal (a=b, see Figure 2.2). And for an elliptical hole the stress at the tip of the ellipse will become 1+2a/b times the applied stress; see for example Knott (1973). For a crack, the minor axis, b, is much smaller than the major axis, a, i.e. b<<a. In this case, the stress at the crack tip grows toward infinity if the ratio a/b approaches infinity. Therefore ordinary stress criteria cannot be applied, due to the fact that the material would fail as soon as the material becomes loaded. Fortunately no materials are perfectly linear elastic and crack tips are never infinitely sharp, which is one explanation why materials can exist at all.

10
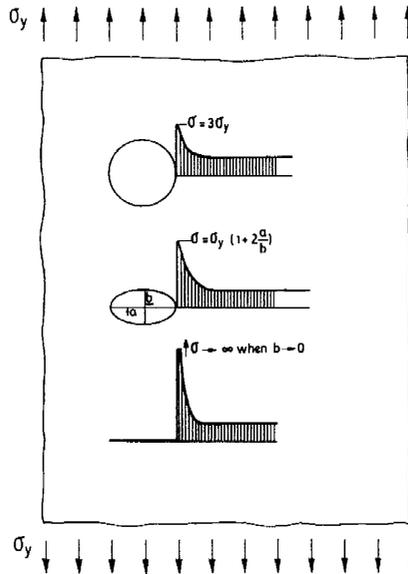
Figure 2.2 The stress distributions near different types of holes in an infinitely large plate uniformly loaded by a stress σ_y, Petersson (1981).

In order to make calculations on structures with notches, conventional stress criteria cannot be applied, because of the stress singularity in the vicinity of the crack tip, and as a result fracture mechanics was developed. With fracture mechanics it is possible to analyze structures with cracks or notches.

2.2 The fictitious crack model

The fictitious crack model was first published by Hillerborg, Modéer and Petersson (1976), and numerous papers and reports have been published on the subject since that time. The basic idea was to develop a fracture mechanics model suitable for analyzing the fracture of plain and reinforced concrete and similar materials. As a result, most of the publications where the fictitious crack model is applied are discussing fracture of concrete. However, the model has been utilized on other materials as well. Aronsson (1984) investigated fibre-reinforced plastics and laminates. There are also some reports dealing with fracture of wood, for example Gustafsson (1985), where a notched beam is analyzed, and Boström (1987a) where the formation of drying cracks is studied.

11

2.2.1 Description of the fictitious crack model

To describe the fictitious crack model, a hypothetical experiment is used. A prismatic specimen without any cracks or notches is loaded in pure tension. If the specimen is tested in a very stiff testing machine, or a fast closed-loop machine, it is theoretically possible to determine the complete load-deformation curve. Nevertheless, this kind of experiment is very difficult, if not impossible, to carry out on wood in practice, as will be discussed later. The complications involved in this category of experiments are material dependent, and also reliant on which mode of failure the tests are made in, and finally dependent on the equipment used in the experiment. However, in this imaginary experiment on wood perpendicular to the grain, the result from the test would resemble the diagram in Figure 2.3.
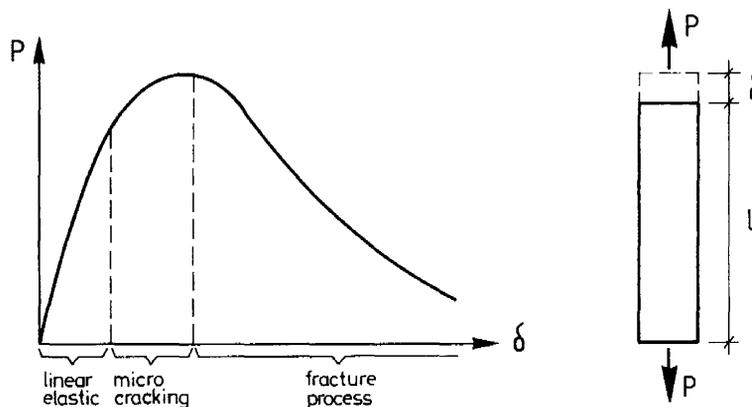
Figure 2.3 Example of a stress-deformation curve in tension for a material like wood, perpendicular to the grain, or concrete.

The figure displays that the material behaves practically linear elastic in the first part of the ascending branch of the curve. But when the load increases and approaches the ultimate load, the curve becomes non-linear because of some sort of damage which is distributed along the whole specimen. When the stress reaches the tensile strength of the specimen, a localized fracture process zone forms. For concrete, experiments made by Heilmann et al. (1969) have shown that the fracture localizes on one cross-section, and all further deformation takes place in this zone. It is then satisfactory to assume that the development of damage will be concentrated on a small material volume close to one cross-section when the specimen is further deformed after the maximum stress has been achieved. This is assumed to be true for wood too, because of the similar behaviour of wood regarding the form of the complete

12

stress-displacement curve. Note, however, that this has never been verified experimentally.

This means, when the maximum stress is reached, all additional deformation in the specimen will take place in the damaged zone, or the fracture process zone, and the material outside the fracture process zone will be elastically unloaded. The stress decreases after the first fracture process zone has begun developing, and consequently only one fracture process zone will be formed in a pure tension test.

Before the peak load, the deformations along the specimen are assumed uniformly distributed along the whole specimen. The total elongation can thus be written

$$\delta = l \epsilon \tag{2.1}$$

where δ is the total displacement, l is the length over which the displacement has been measured, and ϵ is the strain.

When the load reaches the peak value, a localized fracture process zone is assumed to start developing. The stress distribution is presumed to be uniform over the cross-section, and thus the fracture process zone develops simultaneously across the entire cross-section.

After the peak load is reached, and when the specimen is subjected to further total displacement, the specimen is unloaded, i.e. the stresses along the specimen decrease, and the strain outside the fracture process zone decreases corresponding to the stress-strain diagram for the actual material. In the localized fracture process zone the stresses also decrease, but the displacements increase. In other words, the fracture process zone is softening, the stresses decrease during increasing displacement.

The total displacement after the peak load is reached is thus the sum of the uniform displacement along the specimen, plus the additional localized displacements in the fracture process zone, w.

$$\delta = l \epsilon + w \tag{2.2}$$

Note that the widening of the fracture process zone is equal to zero, $w=0$, until the fracture process zone starts developing.

To define the mechanical properties of the material, two relations are used. For the material outside the fracture process zone a regular stress-strain relation is employed, and for the material in the fracture process zone a relation between stress and displacement is used. Consequently the two relations σ vs. ϵ and σ vs. w define the mechanical properties of the material in uniaxial tension; see Figure 2.4.

13

Localized
deformations [1]

a)

Concentrated
fracture surface [1]

b)

$\delta = l\epsilon + w$ 1)
$\delta = l\epsilon$ 2)

σ, MPa

σ, MPa

c)

ϵ, %

w, mm

1) After peak stress
2) Before peak stress
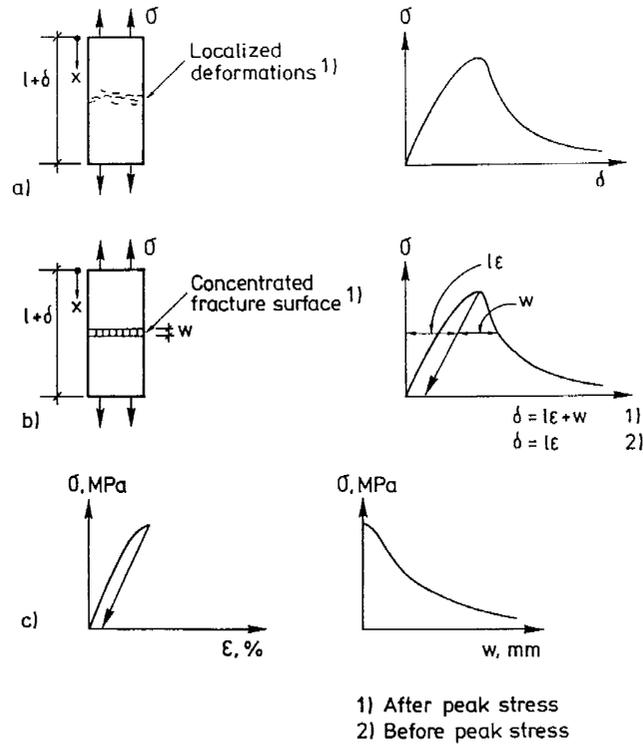
*Figure 2.4 Main characteristics of the fictitious crack model description of tensile
fracture, Gustafsson (1985).*

    a) Possible realistic structural behaviour

    b) Model of structural behaviour

    c) Model for description of the properties of the material

The fracture energy, G_F, now can be defined as the area under the stress-displacement curve for the fracture process zone, the σ-w curve.

$$G_{F,I} = \int_0^{w_c} \sigma \, dw \qquad (2.3)$$

where w_c is the displacement within the fracture process zone when the stress has decreased

to zero and a new crack surface has developed. In other words, the fracture energy is the amount of energy required to form a unit area of new crack in the material.

The same type of characteristics are used for pure shear, or Mode II. Hence the mechanical properties are described by a τ-γ relation outside the fracture process zone, and a τ-v relation in the fracture process zone, where v is the additional displacements in the fracture process zone. The fracture energy for Mode II can thus be determined by the following relation.

$$G_{F,II} = \int_0^{v_c} \tau \, dv \tag{2.4}$$

As noted before, this kind of tension and shear experiment for some materials can be very troublesome to carry out. A comparison can be made between different materials regarding the magnitude of difficulty by using a material property called the characteristic length, l_{ch}. The characteristic length is not a material property in the sense that it is a length that can be measured, but it is derived from three different material properties and therefore it can be regarded as a material property. The characteristic length is defined as

$$l_{ch} = \frac{E \, G_F}{f_t^2} \tag{2.5}$$

where E = modulus of elasticity
G_F = fracture energy
f_t = tensile strength

The characteristic length is a property that controls the extension of the fracture process zone for materials with the same form of softening curve. If linear elastic bulk behaviour is assumed, the characteristic length can be rewritten as

$$l_{ch} = \frac{1}{2} \frac{2 E}{f_t \, f_t} G_F = \frac{1}{2} \frac{2}{\epsilon_0 \, f_t} G_F = \frac{1}{2} \frac{G_F}{\gamma_0} \tag{2.6}$$

and

$$l_{ch} = \frac{E \; G_F}{f_t \; f_t} = \frac{\overline{w}}{\epsilon_0}$$ (2.7)

where ϵ_0 = strain at maximum stress

γ_0 = strain energy density at maximum stress (taking into account only the uniaxial tensile stress)

$\overline{w}$ = average displacement of the σ-w diagram

Hence the characteristic length is proportional to the ratio between fracture energy and maximum elastic strain energy that can be stored in the material per unit volume, equation (2.6). Moreover, the characteristic length also expresses the ratio between average displacement of the σ-w curve and the maximum strain of the material, equation (2.7).

By means of the fictitious crack model, a brittleness number can be defined as d/l_{ch} where d represents a characteristic size of the structure, for instance depth of a beam. Since l_{ch} controls the extension of the fracture process zone, the brittleness number is an indirect comparison between the size of the structure and the extension of the fracture process zone. According to Petersson (1981) and Gustafsson (1985) it has been revealed that when the brittleness number approaches infinity, that is a short fracture process zone compared to the size of the structure, linear elastic fracture mechanics applies. On the contrary, when the brittleness number approaches zero, elastic-plastic models can be utilized.

Because the brittleness number indirectly relates the displacement and the stored elastic energy of the bulk to the displacement and fracture energy of the fracture process zone, the brittleness number measures the brittleness of the structure.

Table 2.1 Typical examples of fracture mechanics properties for some materials, Hillerborg et al. (1986)

Material	Modulus of elasticity E (MPa)	Tension strength f_t (MPa)	Fracture energy G_F (N/m)	Characteristic length l_{ch} (mm)
Steel	200000	1000	100000	20
Concrete	35000	3.5	140	400
Wood	400	4	400	10
Glass	75000	30	5	0.5

In Table 2.1 some fracture mechanics material parameters used in the fictitious crack model are summarized for some materials. Note, however, that the values provided in the table may

be significantly different for different qualities of the same type of material, and that for wood the given values are for a direction perpendicular to the grain.

2.2.2 Simulation of crack propagation using the fictitious crack model

When utilizing the fictitious crack model in simulations of crack formation and/or crack propagation, a numerical method is required. In this report the finite element method is used, but there are other means, such as the boundary element method, the finite difference method and other less general methods. Furthermore, there are two different approaches that can be used for modelling the softening behaviour, the discrete crack approach and the smeared crack approach. However, the fictitious crack model is a material model that clearly belongs among the discrete models, and hence the discrete approach has been utilized in this report.

In order to carry out calculations with the finite element method, the material outside the fracture process zone is modelled in the same way as for an ordinary linear elastic calculation. That is, the material is modelled with a linear σ-ϵ curve. In the calculations presented in this report, four node isoparametric orthotropic elements have been chosen, with the exception of Chapter 5, where isotropic elements were used.

The fracture process zone, on the other hand, is modelled with springs that have a negative spring constant according to the σ-w curve, (the curve slope is negative). It is therefore advisable to approximate the σ-w curve to a straight line or a step-wise linear relation; see Figure 2.5.

$$G_F = \frac{1}{2} f_t w_c \qquad\qquad G_F = \int_0^{w_c} \sigma \, dw$$
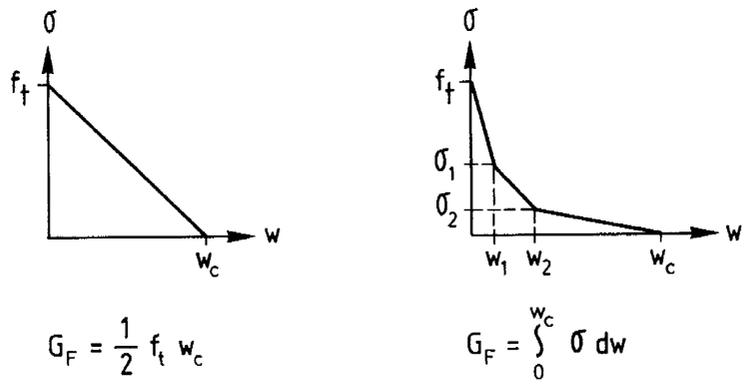
Figure 2.5 Approximated σ-w curves.

17

There are substantial differences between simulating fracture in wood as compared to concrete. Wood is a strongly orthotropic material, and consequently the crack propagation path is usually known in advance. For concrete, however, the crack propagation path is normally unknown and consequently the finite element mesh has to be remeshed during the calculation in order to get satisfactory results. This fact makes calculations on concrete more time consuming and difficult. The fracture of concrete is commonly assumed to be initiated only by pure tension stresses. However, after a fracture process zone has developed, Mixed Mode has to be considered.

For wood, with its orthotropic characteristics, the fracture is usually initiated in Mixed Mode. In other words, there are both tension and shear stresses and displacements. And consequently there are other categories of difficulties involved when analyzing wooden structures than when analyzing concrete structures.

To simulate a normal tension failure with the fictitious crack model is relatively uncomplicated. Figure 2.6 shows a three-point bending test, and in the simulation the crack propagation path is modelled with springs.

STEP 1

STEP 2
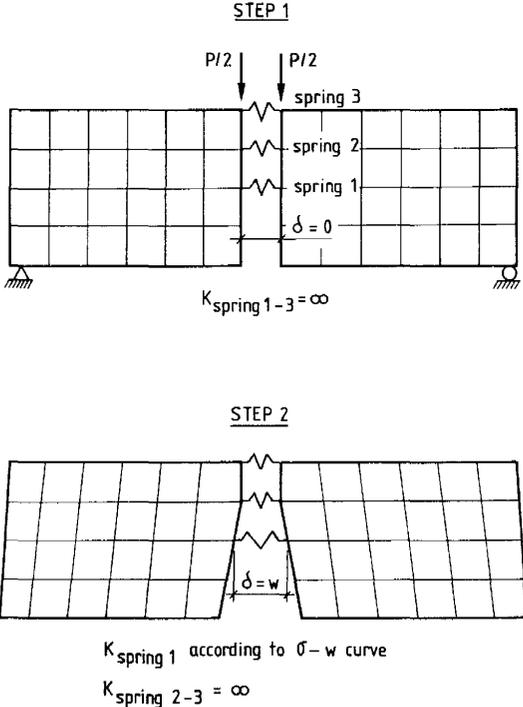
Figure 2.6 Simulated fracture of a three-point bending test on a notched beam.

18

In the mesh, spring elements with a very high stiffness can be attached from the start of the calculation. It is, however, important that the stiffness chosen does not influence the calculation. If the stiffness is too low, there will be deformations in the springs. On the other hand, if the stiffness is too high, there might be numerical problems in the computations. In Figure 2.6 spring elements have been mounted along the assumed crack propagation path.

There are of course different methods that can be employed for the computation, and the method showed here is the one used for all calculations presented in Chapters 4 and 5. The calculations are made stepwise. A unit load, P_{unit}, is applied on the specimen and the system of equations is solved. From the finite element solution forces and displacements in the springs can be determined.

Now a load can be calculated that would provide a force in the most stressed spring corresponding to the strength of the material, i.e. that node has reached the maximum stress according to the stress-strain curve, or the stress at zero displacement in the fracture process zone according to the stress-displacement curve for the fracture process zone. A proportionality factor $\Delta_{step\ 1}$ is thereafter calculated

$$\Delta_{step\ 1} = \frac{f_t}{\sigma_{spring\ 1,\ step\ 1}} = \frac{f_t\ A_{spring\ 1}}{P_{spring\ 1,\ step\ 1}}$$

(2.8)

where f_t = tensile strength

$\sigma_{spring\ 1,\ step\ 1}$ = stress in the most stressed spring in the first step of the computation

$A_{spring\ 1}$ = area over which the spring is acting, see Figure 2.7

$P_{spring\ 1,\ step\ 1}$ = force in the most stressed spring in the first step of the computation

$$A_{spring\ 1} = B \cdot l_1$$

$$A_{spring\ 2} = B \cdot l_2$$

$$A_{spring\ 3} = B \cdot l_3$$

$$A_{spring\ 4} = B \cdot l_4$$
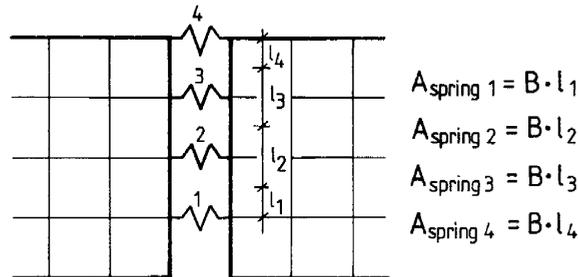
Figure 2.7 Area over which the springs are acting.

Note that the area over which the spring is acting can be different during the computation. In Figure 2.7, the area to be used is explained.

A fracture process zone has now begun developing in the material, and the stiffness of the spring where the tensile strength was achieved has to be exchanged according to the σ-w curve. The stiffness of the spring is now determined as

$$k_{spring\ 1} = \frac{\Delta\sigma}{\Delta w} A_{spring\ 1} \qquad (2.9)$$

where $k_{spring\ 1}$ = spring stiffness
$\Delta\sigma$ = change in stress
Δw = change in displacement
$A_{spring\ 1}$ = area over which the spring is acting

Note that the spring constant, $k_{spring\ 1}$, is negative due to the negative slope of the σ-w curve. A new calculation is made, and a new proportionality factor $\Delta_{step\ 2}$ is determined. In contrast to the first step, there are now two possible incidents: 1) another spring reaches the tensile strength, or 2) a spring modelling the fracture process zone reaches a break-point in the σ-w curve. Both these possibilities must be examined, and the event giving the lowest absolute proportionality factor is chosen.

First a proportionality factor, $\Delta_{step\ 2}$, is calculated so the tensile strength is reached in the most stressed spring.

$$\frac{\Delta_{step\ 1} P_{spring\ 2,\ step\ 1} + \Delta_{step\ 2} P_{spring\ 2,\ step\ 2}}{A_{spring\ 2}} = f_t \qquad (2.10)$$

or

$$\Delta_{step\ 2} = \frac{f_t A_{spring\ 2} - \Delta_{step\ 1} P_{spring\ 2,\ step\ 1}}{P_{spring\ 2,\ step\ 2}} \qquad (2.11)$$

Equation (2.11) can be rewritten so it is valid for all further steps of the computation and is thus

$$\Delta_{\text{step m}} = \frac{f_t A_{\text{spring k}} - \sum_{n=1}^{m-1} \Delta_{\text{step n}} P_{\text{spring k, step n}}}{P_{\text{spring k, step m}}} \qquad (2.12)$$

Now a proportionality factor has been determined so the stress in the second spring is equal to the tensile strength. But, it is possible that the spring modelling the fracture process zone, spring 1, reaches a break-point in the σ-w curve before the tensile strength is obtained in spring 2. Therefore it is essential to check either the stress or the displacement in spring 1. In order to control the stress in the spring, another proportionality factor, $\Delta_{\text{step 2}}$, is calculated that gives a stress equal to the stress in the next break-point in the σ-w curve.

$$\frac{\Delta_{\text{step 1}} P_{\text{spring 1, step 1}} + \Delta_{\text{step 2}} P_{\text{spring 1, step 2}}}{A_{\text{spring 1}}} = \sigma_1 \qquad (2.13)$$

Note that equation (2.13) is equal to equation (2.12) except that instead of the ultimate stress we have the stress in the actual break-point. It is, however, also possible to check the displacement in the spring instead of the stress, and in that case the proportionality factor is determined by

$$\Delta_{\text{step 1}} \delta_{\text{spring 1, step 1}} + \Delta_{\text{step 2}} \delta_{\text{spring 1, step 2}} = w_1 \qquad (2.14)$$

which can be rewritten as

$$\Delta_{\text{step m}} = \frac{w_1 - \sum_{n=1}^{m-1} \Delta_{\text{step n}} \delta_{\text{spring k, step n}}}{\delta_{\text{spring k, step m}}} \qquad (2.15)$$

Now two different proportionality factors, $\Delta_{\text{step 2}}$, have been calculated, one that gives a stress equal to the tensile strength in the most stressed spring outside the fracture process zone, and one that makes a spring in the fracture process zone to reach the next break-point in the σ-w curve. Naturally the smallest proportionality factor is chosen. Note, however, that the sign of the proportionality factor is not regarded here, i.e. the smallest absolute value of the proportionality factor is selected. When a spring reaches zero load or a displacement equal to w_c, the spring is uncoupled or the spring constant is set at zero.

It is important that all springs in the fracture process zone are examined in each step of the computation, especially if there are many break-points in the σ-w curve or the geometry of

the specimen and crack propagation path is complex. In the procedure presented here, a monotonous increased displacement of the springs is assumed. However, this is not always the case; unloading can occur in the springs, and then routines have to be created in order to model this behaviour.

The results are usually presented as a load-displacement curve corresponding to the experimentally determined curve, where the load is the applied load in the loading point and the displacement in the same point or some other point. The applied load is then calculated as

$$P_{applied,\ step\ m} = \sum_{n=1}^{m} \Delta_{step\ n} P_{unit} \qquad (2.16)$$

and the corresponding displacement

$$\delta_{chosen\ node,\ m} = \sum_{n=1}^{m} \Delta_{step\ n} \delta_{chosen\ node,\ step\ n} \qquad (2.17)$$

According to the computations made, it is found that a minimum of five springs should be in the fracture process zone at maximum load, in order to get satisfactory results. The length of the elements can also be expressed as $l_{element} < 0.2 \cdot l_{ch}$. That gives, for ordinary specimens of Scots pine used for determination of fracture mechanics properties in RL and TL orientation, an element length of maximum 2 mm.

2.3 Linear elastic fracture mechanics

Fracture mechanics is a young science, and the birth of it is usually credited to Griffith (1921). If there are sharp notches or cracks in a material, a stress criterion cannot be used, as mentioned before, and hence fracture mechanics has to be applied. There are mainly two different techniques to approach the crack problem in linear elastic fracture mechanics, an energy criterion and a stress intensity criterion. The definitions and derivations of the formulas used here are well known and can be found, for example, in Knott (1973) or Hellan (1984). It should be noted that the following discussions are made only for Mode I.

2.3.1 Definition of linear elastic fracture mechanics formulas

The stress in a plane in front of a crack can be written with the dominant term as

$$\sigma = \frac{K_I}{\sqrt{2\pi r}} \qquad (2.18)$$

where r is the distance from the crack tip, see Figure 2.8, and K_I the stress intensity factor. For an infinitely large plate with a through crack with a length of 2a, uniaxially loaded by a stress σ perpendicular to the crack orientation, the stress intensity factor is

$$K_I = \sigma \sqrt{\pi a} \qquad (2.19)$$

For other geometries and loading, a dimensionless function, f, of geometry and loading is used.

$$K_I = \sigma \sqrt{\pi a} \, f \qquad (2.20)$$

These functions can be found in different handbooks, and in Chapter 4, equation (4.2), the equation is given for a Compact Tension specimen.
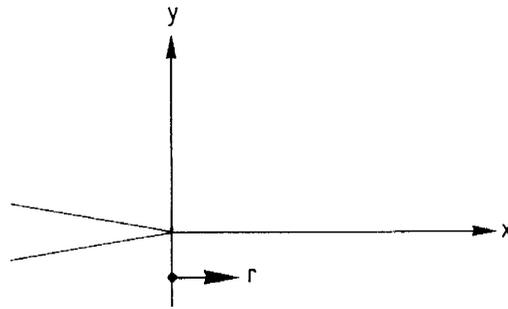
Figure 2.8 Definition of coordinate system at the notch tip.

Irwing (1958) introduced the notation K_{IC} for the critical value of K_I. The failure criterion could thus be written as

$$K_I = K_{IC} \qquad (2.21)$$

23

As previously noted, stresses at a sharp crack tip are infinite, and consequently ordinary local stress criteria cannot be utilized to determine failure. Griffith, who studied brittle failure in glass, proposed an energy criterion to predict an unstable failure from a crack. Griffith noticed that if an existing crack in a body extends, while the points where the loads are applied does not move, the elastic energy of the body decreases. This change in elastic energy when the crack extends from the length a to $a + \Delta a$ can be written

$$\Delta W = -G_I B \Delta a \qquad (2.22)$$

where ΔW = change in elastic energy
G_I = strain energy release rate
B = thickness
Δa = length of the created crack

This is valid for a plate with thickness B and a crack through the plate. When the crack grows, the atomic layers which will form the crack are torn apart. This demands that work is provided. If the work per unit new surface is termed θ, it implies for a growth of the crack Δa that the work

$$\Delta \Gamma = 2 \theta B \Delta a \qquad (2.23)$$

is applied to the crack tip because the new surface is $2B\Delta a$, where $\Delta \Gamma$ represents the work supplied to the notch tip.

Hypothetically it can be assumed that the crack will only grow if the total energy in the body is unchanged or reduced, that is

$$\Delta W + \Delta \Gamma \le 0 \qquad (2.24)$$

and the following fracture criterion for energy is obtained.

$$G_I = 2 \theta \qquad (2.25)$$

When Griffith wrote the energy relation, he had studied an infinitely large plate with a crack. The length of the crack was 2a, and the plate was subjected to a stress σ perpendicular to the crack. According to these conditions Griffith found

$$\sigma = \sqrt{\frac{2\theta E}{\pi a}} = \sqrt{\frac{G_I E}{\pi a}} \qquad (2.26)$$

By using equation (2.19) and (2.26) a relation between stress intensity factor and strain energy release rate can be established.

$$K_I = \sqrt{G_I E} \qquad (2.27)$$

Consequently the failure criterion can be written

$$G_I = G_{IC} \qquad (2.28)$$

where G_{IC} is the critical strain energy release rate. In other words G_{nc} can be defined as the energy required to extend a crack a unit area, where subscript n is the particular mode of the fracture (n=I,II,III).

When linear elastic fracture mechanics is applicable, the fracture energy and the critical strain energy release rates are equal.

$$G_{F,I} = G_{IC} \qquad (2.29)$$

Both K_{IC} and G_{IC} are considered as material properties that reveal something about when a crack starts propagating. To experimentally determine these properties, there are a number of different specimens and loading arrangements that can be employed. There are, however, no studies made to thoroughly study the behaviour of the different specimens when the material is wood. Most specimens were developed for experimental determination of the fracture toughness, K_{IC}, of metals, and these specimens are now used in the same manner for wood.

2.3.2 Aspects regarding use of linear elastic fracture mechanics on wood

The equations shown so far are derived for isotropic materials. For strongly orthotropic materials it has been shown that an isotropic assumption is not valid, Walsh (1972) and Valentin and Adjanohoun (1991). Walsh examined a cleavage specimen according to Figure 2.9 with different sizes, or more precisely different values on a/c. However, the relation between notch length, a, ligament length, W, and height, 2c, was constant, (a+W)/c=12.

25
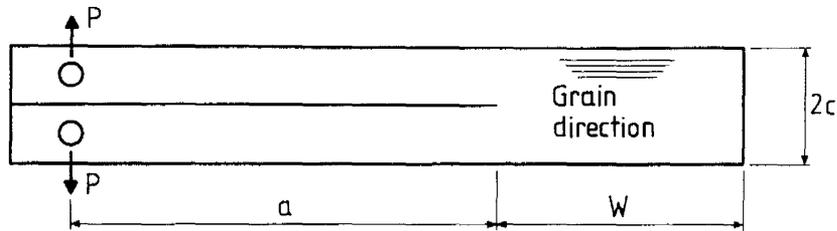
Figure 2.9 Cleavage specimen analyzed by Walsh (1972).

In Table 2.2 the results from Walsh are summarized. For the actual specimen the ratio between the orthotropic and isotropic result can be as low as 0.3, i.e. the stress intensity factor if orthotropic behaviour is used is only 30% of the case when isotropic behaviour is assumed. This example shows the necessity of using the orthotropic stiffness parameters when calculations are made on wood.

Table 2.2 Computed stress intensity factors for a cleavage specimen, Walsh (1972). Note that $\sigma = 6Pa/c^2$

| | $K/\sigma a^{1/2}$ | | Ratio of orthotropic to |
a/c	Isotropic	Orthotropic	isotropic result
1.75	0.496	0.178	0.36
3.50	0.311	0.099	0.32
5.25	0.243	0.074	0.30
7.00	0.206	0.078	0.37

The comparatively most frequently used specimens for determination of the fracture mechanics properties of wood are the Compact Tension (CT) and the Single Edge Notched (SEN) specimens, presented in Figure 2.10. The determined parameter is typically the critical stress intensity factor, K_{IC}, but there are also some references where the critical strain energy release rate, G_{IC}, or the fracture energy, G_F, has been measured. In a State-of-the-Art report, made by Valentin et al. (1991), different specimens and a comprehensive list of results are presented.

26

| 0.3B | | | 1.20(W+a) |
| 0.25B | | | |

a   W

1.25(W+a)

Compact Tension Specimen   Single Edge Notched Specimen

a   W
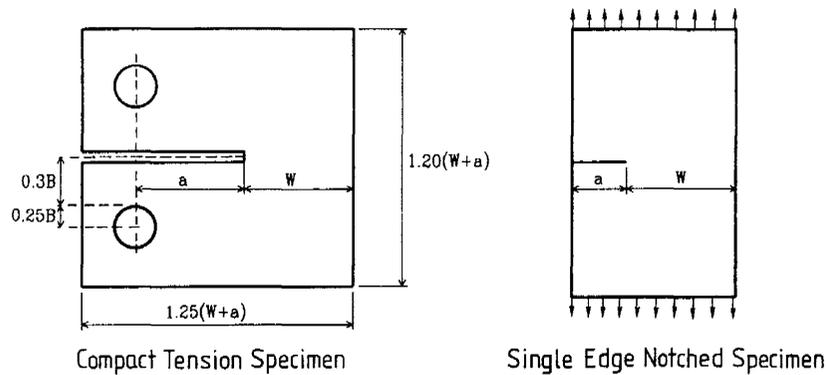
Figure 2.10 The Compact Tension and the Single Edge Notched specimens.

To experimentally determine K_{IC}, it is important that the size of the fracture process zone is negligible. If not, the process zone will influence the results, and a misleading value of the property will be acquired. It is, however, possible to compensate for the fracture process zone, if the length and the stress distribution of the fracture process zone are known at the maximum load.

In Figure 2.11, a theoretical calculated stress distribution in front of a notch at maximum load in a Compact Tension specimen is shown; see also Chapter 4. The actual specimen has the dimensions length:height:width = 50:48:20 mm and a notch length a=20 mm; see Figure 2.10. The mechanical properties are typical for wood perpendicular to the grain; see Chapter 4. The length of the fracture process zone is on the order of around 2 mm for this specific specimen. If now K_{IC} is determined from the maximum load, without compensation for the fracture process zone, a value of $K_{IC}=280$ kNm$^{-3/2}$ is obtained. On the contrary, the fracture process zone can be considered, and we can assume that the crack length is a bit longer than the initial length. Assume that the crack length should be the original crack length plus half the length of the fracture process zone. With this assumption the critical stress intensity factor is determined to be $K_{IC}=303$ kNm$^{-3/2}$, i.e. an 8% higher value than the value determined without compensation for the fracture process zone.

Other methods can also be utilized. In Chapter 4 one method is described that was proposed by Wright et al. (1987). The method is a graphic method that does not use the maximum load when determining the critical stress intensity factor. Instead a new load is determined graphically, and the newly resolved load is used in the determination of K_{IC}. The procedure

27

was developed to compensate for plastic deformations in the crack tip, and is not applicable to wood.
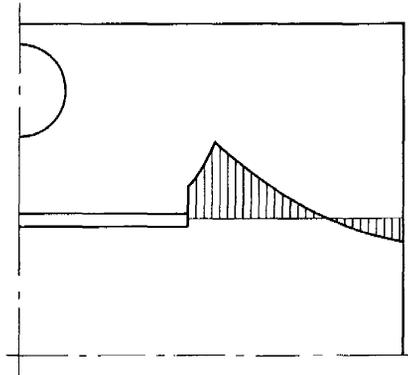
Figure 2.11 Principal sketch of the stress distribution in front of a notch at maximum load in a Compact Tension specimen, Boström (1990).

The Wright method gives an underestimation of K_{IC}. It has been shown by Petersson (1981), for concrete, that K_{IC} increases with increasing size of the specimen up to an asymptotic value, which is the true critical stress intensity factor. In a method where a load lower than the maximum load is employed for determination of K_{IC}, the obtained value will always be lower than the true critical stress intensity factor.

If the graphic method were used in the same example as above, the result would be $K_{IC} = 226$ $kN/m^{-3/2}$, i.e. more than 25% lower than when calculating K_{IC} with compensation for the fracture process zone.

2.4 Finite Small Area Theory

Linear elastic fracture mechanics has been derived from a singularity in a body, and therefore a singularity has to be present, i.e. a crack or a notch, if the method is to be applicable. This fact restricts the use of linear elastic fracture mechanics considerably. However, there is at least one method that avoids that particular limitation in linear elastic fracture mechanics, the Finite Small Area Theory, Landelius (1989). In the finite small area theory, a unification is made between the linear elastic fracture mechanics and an ordinary critical stress criteria. By this unification it is feasible to predict fracture loads of problems which do or do not have singular points, i.e. calculations can be made even on structures without notches or cracks.

The finite small area theory is based on the assumption that fracture occurs when the average

28

stress in a certain finite small area satisfies a stress criterion. It is therefore fundamental to determine the size of the finite small area. The length of the finite small area is determined so the finite small area method gives the same failure load for a brittle body with a sharp notch, as linear elastic fracture mechanics would give. The finite small area is then regarded as a material property.

The stress in front of a notch tip for a linear elastic material is

$$\sigma = \frac{K_I}{\sqrt{2\pi x}} \tag{2.30}$$

For an isotropic linear elastic material, with a thickness B, the resultant force over the length x can be calculated as

$$P = B \int_0^x \sigma \, dx = 2B \, K_I \sqrt{\frac{x}{2\pi}} = 2B \sqrt{\frac{E \, G_I \, x}{2\pi}} \tag{2.31}$$

The mean stress over the length x is thus

$$\bar{\sigma} = \frac{P}{B \, x} = \sqrt{\frac{2 \, E \, G_I}{\pi x}} \tag{2.32}$$

A length $x = x_0$ can now be determined so $\bar{\sigma} = f_t$ and $G_I = G_{IC}$. Accordingly the length of the finite area is determined by

$$f_t = \sqrt{\frac{2 \, E \, G_{IC}}{\pi \, x_0}} \tag{2.33}$$

or

$$x_0 = \frac{2 \, E \, G_{IC}}{\pi \, f_t^2} \approx \frac{2 \, l_{ch}}{\pi} \tag{2.34}$$

According to studies by Masuda (1988), the length of the finite small area in the longitudinal direction is 1-2 mm and in the radial and tangential directions 0.4 mm for Hinoki cypress

(*Chamaecyparis obtusa*). These lengths have led to the hypothesis that the finite small area is related to the length of the wood fibres. However, the model used by Masuda is different from the described model. In Masuda's model, the mean stress is calculated over a volume, instead of an area.

In Landelius (1989), finite small area theory was compared to nonlinear analysis. According to these results finite small area theory seems to be promising. However, there is still a lot of research that has to be done regarding the finite small area theory, and an important task is to verify if the length of the finite small area is a material property or not.

3 Method for determination of the softening behaviour of wood

The fictitious crack model, described in Chapter 2, is a nonlinear model that can be applied to many different materials. However, before the Fictitious Crack Model can be applied to wood, a number of material properties have to be known, such as
- orthotropic stiffness parameters
- strength of the material
- the softening behaviour of the material.

One major difference between fictitious crack model and more conventional strength and fracture mechanics approaches, is that the softening behaviour of the material is used in the model, i.e. the stress-displacement relation after the ultimate stress. Accordingly it is necessary to experimentally determine the softening behaviour for the actual material.

This kind of tension and/or shear experiment, for some materials, can be very difficult to carry out. The outstanding problem when trying to measure the complete stress-displacement curve is to acquire stability in the test. If the test is unstable, the results can be misleading depending on the magnitude of the instability. A comparison can be made between different materials with the same form of the σ-w curve regarding the degree of difficulty by using the characteristic length, l_{ch}. Higher values on l_{ch} give a more ductile behaviour and make it easier to get stable experiments, while low values on l_{ch} give a more brittle failure and the risk for instability is extensive.

3.1 Stability requirements

When a pure tension test is carried out, strain energy is stored in the specimen, and the longer the specimen is, the more strain energy is stored in the specimen. If the amount of internally stored strain energy is too high, a catastrophic failure will occur and the experiment is unstable. In other words, the amount of internal stored strain energy has to be minimized in order to maintain stability during the whole experiment, that is, the brittleness number d/l_{ch} has to be as small as possible. According to Table 2.1 in Chapter 2, wood perpendicular to the grain has a much lower value on the characteristic length than for example concrete, and consequently it is much more difficult to make a stable tension test on wood, than on concrete.

In Figure 3.1 the result from a hypothetical tension test where translation instability occurs is presented. According to the figure, the load suddenly drops from one value to another. The stability conditions depend on the dimensions of the specimen, the material properties and on

the experimental setup. Therefore it is necessary to carefully study the test arrangement with respect to stability before the experiments are carried out.
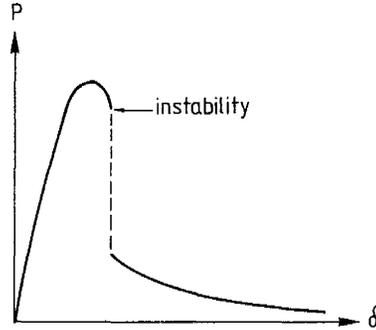
Figure 3.1 Translation instability.

In the thesis by Petersson (1981) an expression was derived in order to determine the maximum length of the specimen in a direct tensile test so translation instabilities are avoided. If the length of the specimen exceeds a theoretical maximum length, a stable tensile test cannot be obtained, with respect to translations. Figure 3.2 gives a schematic illustration of a tensile test. The maximum length of the specimen, 1, can thus be determined from the relation

$$S_{ntot} = \frac{S_{nm} S_{ns}}{S_{nm} + S_{ns}} > A_0 \left(-\frac{d\sigma}{dw} \right) , \quad S_{ns} = \frac{EA}{1} \tag{3.1}$$

where 1 = length of the specimen

$(d\sigma/dw)$ = slope of the σ-w curve

A = cross sectional area of the specimen outside the fracture process zone

A_0 = cross sectional area of the fracture process zone

E = modulus of elasticity of the specimen

S_{ntot} = translation stiffness of the complete testing system

S_{nm} = translation stiffness of the device outside the specimen

S_{ns} = translation stiffness of the specimen

For wood perpendicular to the grain with E=300 MPa and $(-d\sigma/dW)$=6 GPa/m , a maximum length of the specimen in the order of 8 mm applies if A=20·20 mm^2 and A_0=20·12 mm^2. This is valid if the stiffness of the testing arrangement is infinitely high. The stiffness of the

testing systems today usually is a minor problem when closed loop machines are used. The rather steep slope of the σ-w curve used above has been achieved in a few experiments, but usually the slope is greater than the given value, and consequently it is easier to get stable experiments. The modulus of elasticity is lower than usual, but that gives a shorter maximum length and thus a length on the safe side.
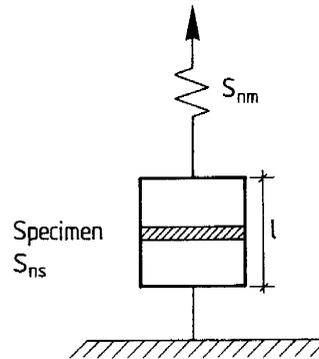
Figure 3.2 A schematic illustration of a direct tensile test, where S_{nm} is the stiffness of the testing arrangement.

The discussion so far has dealt with pure translations, but unfortunately there are also rotations of the crack surfaces that may occur in the specimen during the experiment. These rotations are almost unavoidable in a direct tension test. Small load eccentricities, asymmetry of specimen and imperfection of material can cause asymmetric deformations in the fracture process zone. In order to avoid these rotational instabilities, and obtain a reliable and stable stress-displacement curve, the rotational stiffness of the experimental setup must be high enough to counteract possible rotations.

In Figure 3.3 a hypothetical tension test is presented. On the specimen two clip-gauges are mounted, one on each side of the specimen. The result from the experiment could look like the diagram in the Figure 3.3 (in Appendix F a number of experimentally determined curves are shown). In the diagram three different curves are drawn, one curve for each clip-gauge, i.e. the displacement on each side of the specimen, and one curve for the mean value of the two clip-gauges. If rotational stability had been achieved, all three curves would coincide. However, if there are rotational instabilities, as shown here, the curves do not coincide. If, as in practice, the displacements are measured by the mean value of the two clip-gauges, it can be impossible to tell if rotational instabilities occur or not. The mean curve is often very

smooth and gives an impression of being correct.
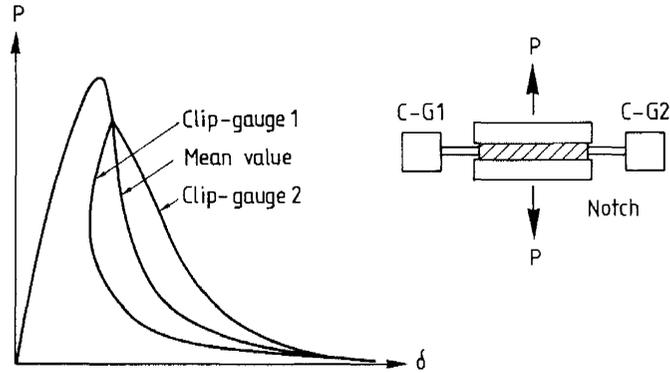
Figure 3.3 Rotational instability.

In order to avoid these instabilities and to get a reliable stress-displacement curve, the rotation stiffness of the test arrangement has to be high enough to counteract the possible rotations.

According to Hillerborg (1989) the needed rotation stiffness of the testing arrangement can be found by

$$S_{rtot} = \frac{1}{2\left(\dfrac{1}{S_{rm}} + \dfrac{1}{S_{rs}}\right)} > I_0\left(-\frac{d\sigma}{dw}\right) , \quad S_{rs} = \frac{2EI}{1} \tag{3.2}$$

where S_{rtot} = rotational stiffness of the complete testing system

S_{rm} = rotational stiffness of the test arrangement on each side outside the specimen

S_{rs} = rotational stiffness of the specimen on each side outside the fracture process zone

1 = length of the specimen

I_0 = moment of inertia inside the fracture process zone

I = moment of inertia outside the fracture process zone

E = modulus of elasticity

$(-d\sigma/dw)$ = slope of the σ-w curve

34

In the same way as Petersson (1981) derived an expression for stable tests in pure translation, a maximum length of the specimen can be determined to avoid rotation instabilities. According to equation (3.2) the maximum length, if the stiffness of the testing arrangement is very high, $S_{rm} = \infty$, is

$$1 < \frac{E\,I}{I_0\left(-\dfrac{d\sigma}{dw}\right)} \qquad (3.3)$$

If normal values for wood are used in equation (3.3), i.e. the same values used previously when determining the maximum length regarding translation stability, then the maximum length would be in the order of 8 mm for the specimen used. This is valid if the stiffness of the testing arrangement is assumed to be infinitely high.

Some of the experiments were made in order to find out if rotational instabilities occur. In these tests four clip-gauges were mounted, two on each side of the specimen; see Figure 3.4. One pair of the gauges was used for control of the machine, i.e. a mean value was taken from these two gauges. The other two gauges were separate and consequently the displacement on each side of the specimen was measured.
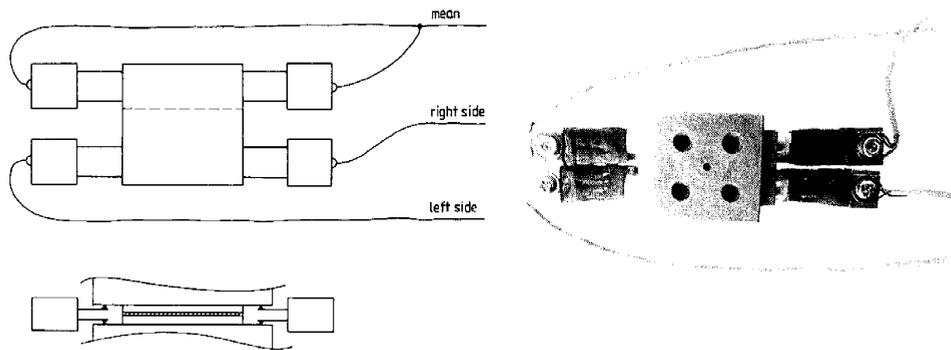
Figure 3.4 Arrangement of clip-gauges when determining rotational stability.

If the experiment is stable, the three load-displacement (or stress-displacement) curves should be equal. In Figure 3.5 these three curves are shown and they coincide, so the experiments have to be considered stable with regard to rotations. However, four clip-gauges were only utilized in a small number of tests, and hence it is possible that other tests were instable. More curves can be found in Appendix F.

35
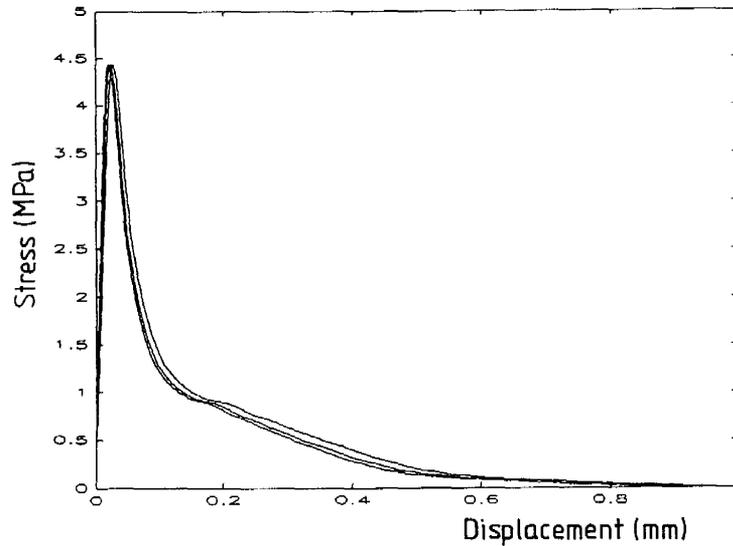
Figure 3.5 Stress-displacement curves for measurements of rotational instability.

In the experimental series made, two different servo valves were used in the testing machine. When the machine was delivered, it was supposed to be configured with two different servo valves, one small and one large servo valve, but by mistake it was delivered with two large servo valves. A small servo valve, which has a small flow of oil, is used for static tests where the piston moves slowly, but compensates for the errors between set-point and feed-back very quickly. A large servo valve, which can have a large flow of oil, is mainly utilized for dynamic tests where the piston has to move long distances and often very fast. However, it is more difficult to compensate for errors between set-point and feed-back with a large servo valve.

When the large servo valve was used a comparatively large number of specimens had instability failures, and around 10% of the tested specimen proved unstable. These instabilities were usually drastic, i.e. the load momentarily dropped to zero. Later, when one of the large servo valves was exchanged, and a small servo valve was attached to the machine, the number of complete instable failures decreased drastically. However, even if the severe instabilities were eliminated, i.e. the sudden drops to zero load, some instabilities sometimes occurred, especially in the shear tests. The magnitude of these instabilities was usually a drop of around 5-10 % of the maximum load. In the results presented here, a drop of 5% of the maximum load has been allowed. It should be noted that the small servo valve was utilized for most of the experiments presented in this chapter.

36

3.2 Experimental setup

In order to achieve a loading arrangement where no instabilities may occur, a completely new testing arrangement was developed by Hassanzadeh et al. (1987). The purpose of this arrangement was to produce a device, usable for Mixed Mode experiments, with a sufficient stiffness with respect to both translations and rotations. The device was mainly developed and designed for experiments on concrete, but it works as well for experiments on wood perpendicular to the grain. The objective of this study was initially to include the Mixed Mode behaviour. However, there were a lot of problems regarding the experiments, especially instability, and therefore the Mixed Mode tests were excluded from the series.

The experimental set-up is shown in Figure 3.6. The testing system used was a MTS-810. This machine is a closed loop machine, i.e. it has a regulating system which continuously compares the actual value (feed-back), measured by the gauges, and the set point programed to the testing machine, and subsequently compensates for the difference between these two values. With this type of machine, it is possible to control the crack opening by using clip-gauges mounted in the premade notch. The experiments are than made in control of the clip-gauges.
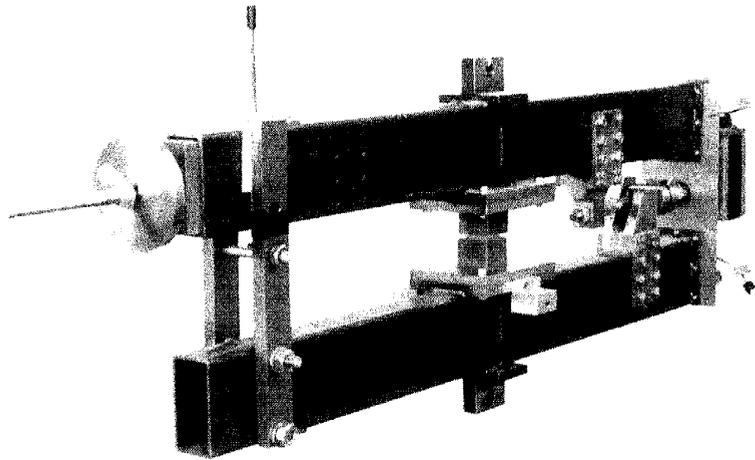

Figure 3.6 Experimental set-up.

According to Figure 3.6 the arrangement into which the specimen is glued consists of two beams that are connected at one end by a thin steel plate. By utilizing such a device, the loading of the specimen is not only pure tension, but also to some extent a rotation. The

37

reason this device is used is to prevent uncontrolled rotations of the specimen. It has been shown by Hassanzadeh et al. (1987) that the errors due to the nonuniform loading are minor compared to the errors due to rotational instabilities. A FEM calculation was made where the beams were modelled, and according to this calculation, presented later in this chapter, the equipment used produces satisfactory results.

In order to determine the complete stress-displacement curve in pure tension or pure shear, other more simple arrangements can be utilized. The actual testing arrangement was used because the initial purpose of the investigation also included Mixed Mode failure. However, after a few introductory experiments in Mixed Mode, all of which were completely unstable, this experiment was fully concentrated on Mode I (and to some extent Mode II).

Two clip-gauges were utilized, see Figure 3.7. These gauges were coupled so that a mean value of the two gauges was sent to the testing machine. This coupling was chosen to allow the machine to monotonously increase the displacement, even if rotational instability occurred.
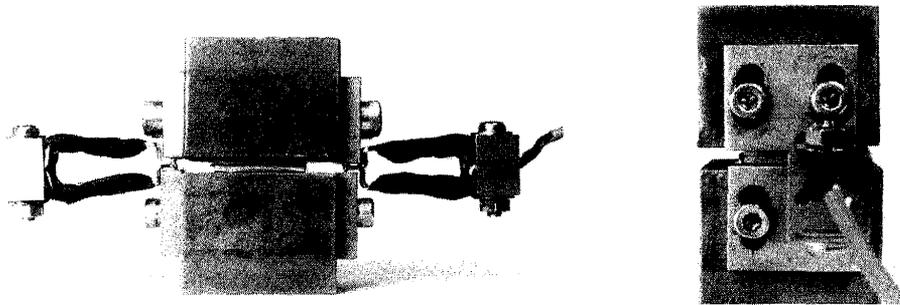
Figure 3.7 Arrangement of clip-gauges on the specimen.

3.3   Specimens used in the experiments

All results presented in this chapter are from specimens taken from one board. Therefore the results obtained cannot be taken as a representative behaviour for Scots pine. The results presented show the behaviour of one board of lumber, and nothing more.

As mentioned earlier, all specimens were sawn from one board, and the chosen geometry was $20 \cdot 20 \cdot 3$ mm^3; see Figure 3.8. After the specimens were sawn they were visually inspected, and only specimens without any defects, such as visible cracks or knots, were used in the experiments. Notches were made with a miller, and the width of the notch was chosen to be 0.5 mm. However, one test series was made with some different widths of the notch, and according to these results there was a great scatter, see Table 3.1. The length of the specimens was only 3 mm, and when the width of the notch was 1 mm and above, the

stiffness of the cantilever was insufficient to squeeze out the glue, and consequently the cantilevers bent. A notch width of 0.5 mm was chosen for two reasons. Firstly, from a practical point of view, the 0.5 mm notch was easiest to make. Secondly, it was noted that the cantilevers bent on the specimens with a notch width of 1 mm and 1.5 mm, which might influence the measured curve.
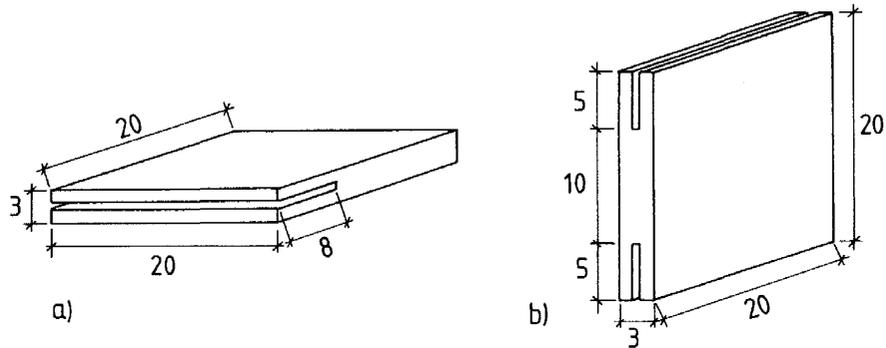
Figure 3.8 Geometry of specimens. a) Tension specimen b) Shear specimen

Table 3.1 Influences of notch width on tension strength and fracture energy

Notch width (mm)	Orientation	Tension strength (MPa)		Fracture energy (N/m)		Number of specimens
		mean	s.d.	mean	s.d.	
0.30	RL	6.3	1.0	390	120	9
0.50	RL	6.8	1.1	380	90	9
1.00	RL	5.4	1.1	500	50	8
1.50	RL	5.8	0.8	490	100	5

The tension specimens were made as single side notched specimens, Figure 3.8a, and the shear specimens had notches on both sides, Figure 3.8b. The reason why single side notched specimens were chosen for the tension specimens was the problem of multiple cracks. However, in one tension series, specimens conditioned in high relative humidity, 97% RH, double side notched specimens were used. These tests showed that two cracks could develop, propagating in different directions; see Figure 3.9. When more than one crack develops, the

amount of energy consumed by the specimen during the experiment will be higher than if only one crack is formed. In order to avoid these multiple cracks a single edge notched specimen was preferable.

Figure 3.9 Double side notched specimen with multiple cracks.

The depth of the notch for the tension specimens was 8 mm, which gives a relative notch depth $a/(W+a)=0.4$. The notches on the shear specimens were made 5 mm deep on both sides of the specimen, i.e. $2a/(W+2a)=0.5$. There is one exception to these geometries. The very moist tension specimens, conditioned in 97% RH, had the same geometry as the shear specimens. The high moisture content in these specimens affected the bond in the sense that the strength of the glue decreased. Therefore a shorter ligament length had to be obtained and a double side notched specimen was used.

3.4 Specimen attachment to the testing arrangement

The specimens were glued into the testing arrangement with a two component epoxy (Devcon epoxy). It was found that the curing time of the glue considerably influenced the experimental results. According to the instructions for the glue, the curing time would be roughly five minutes. However, even after two hours of curing, there could be considerable plastic deformations in the glue on some of the specimens; see Figure 3.10. After a number of introductory experiments with different curing times, a curing time of at least three hours was chosen. The thickness of the glueline influences the curing time. If the glueline is thick, the temperature developed during curing is higher than if the glueline is thin and the curing time is dependent on temperature. Higher temperature gives a shorter curing time. Unfortunately it was very difficult to make all gluelines with the same thickness, and consequently the needed curing time is different for each specimen. However, when the glue was cured for

40

three hours or more, there were no detected plastic deformations in the glue. In the introductory experiments, another type of epoxy was examined (Araldit Rapid). According to these tests, the strength of the glue was not sufficient even after four hours curing time.
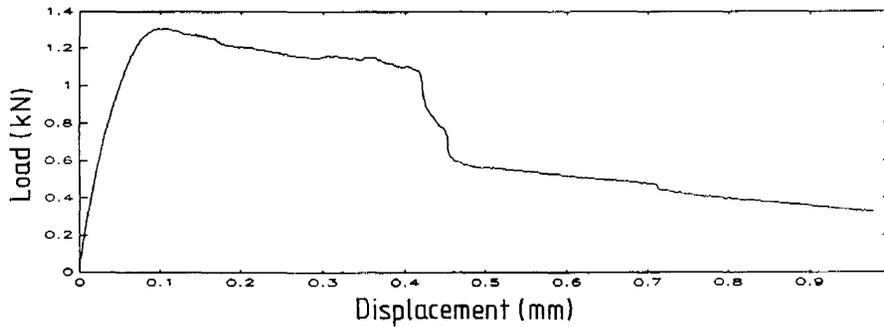
Figure 3.10 Result influenced by plastic deformations in the glue line.

To get wood failure in the specimens conditioned in 97% relative humidity, double side notched specimens had to be used. It was not possible to get wood failure on the single side notched specimens. Ten introductory tests gave a glue failure, and no wood failure. The double side notched specimens had a smaller ligament area, and consequently the maximum load was lower than for the single side notched specimens, resulting in a decreased stress in the glue line which was necessary in order to get a wood failure. For this series another glue was also examined, (Casco Polyurethane 1809). However, the glue had not enough strength, and consequently the failure occurred in the glue line. Another problem with the Polyurethane was the frothing. The glue that was pressed out beside the specimen was frothing and completely covered the specimen.

3.5   Speed of loading

The loading rate was not constant during the whole experiment. The loading rate here is defined as the speed with which the clip-gauges open. The first part of the curve was determined with a low loading rate in order to have a loading time of around 1-3 minutes to peak load. After the peak load was reached and the most difficult part of the curve measured, i.e. the part with the steepest slope of the descending branch of the curve, the loading rate was increased. Figure 3.11a shows the loading rate for the tension tests, and Figure 3.11b shows the loading rate for the shear tests.

41
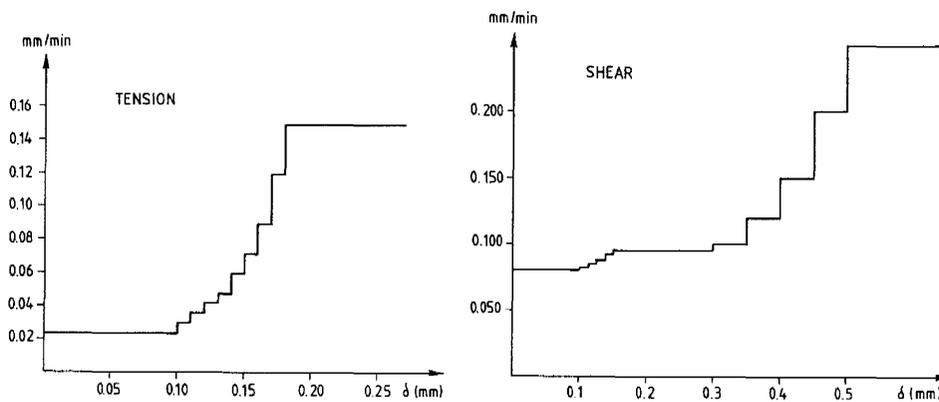
Figure 3.11 Loading rate for a) tension test and b) for shear test

3.6 Conditioning of specimens

As already mentioned, wood is a hygroscopical material, i.e. the mechanical properties are dependant on the moisture content. In order to investigate the moisture dependencies on the stress-displacement curve, specimens were conditioned in four different climates.
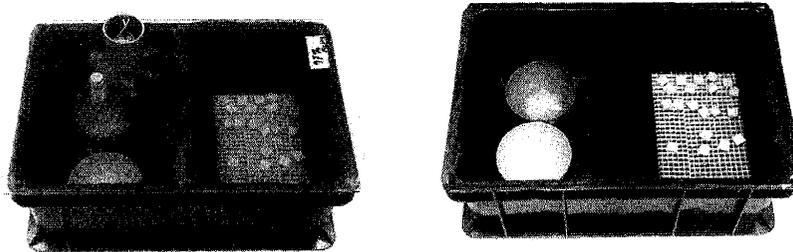
Figure 3.12 Conditioning box containing salt solution and specimens.

Specimens were kept in hermetic boxes containing different salt solutions; see Figure 3.12. These salt solutions are saturated and keep the relative humidity constant in the box. Depending on salt solution used, different climates can be obtained. In the present investigation the following salt solutions were employed:

- Magnesium Chloride, $MgCl_2$, gives 33% RH
- Sodium Bromide, NaBr, gives 59% RH
- Sodium Chloride, NaCl, gives 75% RH
- Potassium Sulphate, K_2SO_4, gives 97% RH

The relative humidity obtained with the different salt solutions is more or less dependent on temperature. The given relative humidities are valid for a temperature of 20°C which is the temperature at which the specimens were kept.

It was impossible to determine the moisture content for each specimen because of their small size and because they were glued into the testing arrangement and subsequently destroyed during the test. Therefore a number of larger specimens were made of the same material, i.e. taken from the same board close to the place where the specimens for load-displacement measurements where taken. These specimens were only used for determination of moisture content and density. The large specimens were kept in the same boxes until the weight had stabilized, i.e. they were in equilibrium with the climate in the climatisation boxes. After no changes in weight could be measured, the specimens were kept an additional two weeks in the boxes before determination of moisture content and density. At that time the weight was measured for each of the large specimens, and afterward they were placed in an oven and dried at a temperature of 105°C for 48 hours. Now a new measurement of weight and dimension was made, and moisture content, u, and density, $\rho_{0,0}$, were determined as

$$u = \frac{m_u - m_{dry}}{m_{dry}} \tag{3.4}$$

$$\rho_{0,0} = \frac{m_{dry}}{V_{dry}} \tag{3.5}$$

where m_u = weight at the actual moisture content
m_{dry} = weight when dry
V_{dry} = volume when dry

Table 3.2 Moisture content and density of the material

| Climate | Moisture content (%) | | Density $\rho_{0,0}$ (kg/m³) | | Number of |
(%RH)	mean	s.d.	mean	s.d.	specimens
33	7.6	0.1	450	20	6
59	9.7	0.1	470	20	6
75	13.8	0.1	470	20	6
97	26.5	0.2	460	30	6

Note: All results regarding measurements of moisture content and density are presented in Appendix B.

Note that the moisture content was determined immediately after the specimens were taken from the conditioning boxes. The specimens used for determination of the stress-displacement curve would have the same moisture content if the experiment had been carried out directly when the specimens were taken from the boxes. However, this was not possible. The specimens had to be glued into the testing arrangement, and thereafter cured for three hours. Consequently the moisture content would change because of the difference in relative humidity between the conditioning boxes and the laboratory. Therefore the time used to attach the specimen to the loading arrangement was minimized, and was around 5 minutes. When the specimens were attached, they were protected by the glue and the unprotected area of the specimens was very small. Note, however, that the specimens conditioned in 97% RH were protected with tape during the curing time of the glue in order to avoid moisture migration from the specimen.

In order to estimate the change in moisture content during the gluing and curing time, five specimens conditioned in 75% RH, and five conditioned in 97% RH, were examined. The weight of the specimens was measured when they were taken from the climatization box. Thereafter the specimens were kept in the same room as the testing machine for five minutes. The relative humitity in the room was 40%. Another measurement of the weight was now made. In order to simulate the curing time, i.e. when the specimen is protected on two sides by the epoxy, a PVC tape was attatched to the specimens. The specimens were then kept in the laboratory climate for three more hours, and finally the weight was measured once more.

According to these tests, the moisture content for the specimens conditioned in 97% RH decreased from u=26.5% to u=15.2% and had a standard deviation of 1.1%. The specimens conditioned in 75% RH showed that the moisture content decreased from u=13.8% to u=10.5% and the standard deviation was 0.1%. Note, however, that these tests give an overestimation of the decrease of moisture content, due to the extra loss of material when the PVC tape is removed from the specimen before the final measurement of weight. But it is important to recognize that the moisture content given is not in accordance with the true moisture content of the specimens.

3.7 Grain orientations examined

Three different grain orientations were examined for the tension specimens and one orientation, RL, for the shear specimens. The tension failure usually occurs in the weakest direction, that is perpendicular to the grain. There are, however, two different orientations perpendicular to the grain, the RL orientation and the TL orientation. It was therefore obvious that at least these orientations should be examined. But there exists an infinite number of orientations between the pure RL and TL orientations. In order to see if an

orientation between pure TL and RL had a completely different behaviour, a third orientation was chosen for examination. This third orientation is called 45°. The orientation of the grain in the 45° series was not exactly 45°, but varied between 35° and 55°. There was one exception, the specimens climatized in 97% RH. For these specimens only one orientation was examined, the RL orientation. The three different orientations are shown in Figure 3.13.
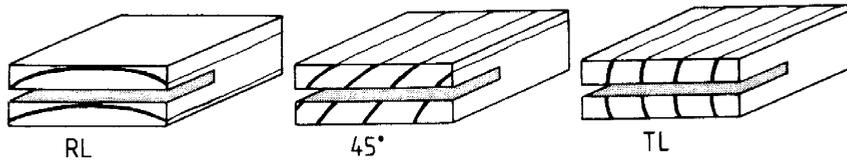
Figure 3.13 Different orientations examined. a) RL b) 45° c) TL

3.8   Theoretical analysis of the specimen

In order to determine the stress distribution along the crack path a finite element analysis was made. If the stress distribution is uniform, the maximum load from the experiment can be used for determination of the tensile strength. Another important aspect is that the input data can be compared with the output data. If this testing method gives the true softening behaviour, then the outcome from the computation should be equal to the softening behaviour used as the input material behaviour of the elements.

The FEM program used for these calculations was ABAQUS. In order to simplify the computation, the complete loading arrangement was not modelled in the FE-mesh. The error is very small because of the very high stiffness in the loading arrangement compared to the stiffness of the specimen. The chosen structure is shown in Figure 3.14.

The specimen was modelled with orthotropic stiffness parameters, and the softening behaviour was modelled by a bi-linear relation; see Figure 3.15. The material properties used in the calculation are given in Figure 3.15.

The computation was made by Palm (1991), who chose to use a smeared crack approach. The ABACUS program has a special element for crack simulations, developed for calculations on concrete. This element also takes nonlinearity on the stress-strain relation into account.

Figure 3.16 shows a calculated load-displacement curve, and a σ-w curve determined from the calculated load-displacement curve. The σ-w curve can be compared with the curve used as input in Figure 3.15, and these curves coincide very well.

45
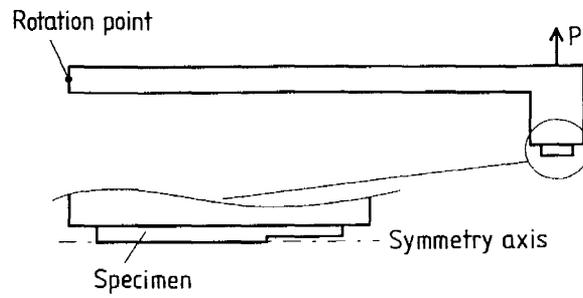
Figure 3.14 Structure used for FEM-analysis.

$E_{||}$ = 15000 MPa
$E_{\perp}$ = 350 MPa
G = 500 MPa
v = 0.05
G_F = 400 N/m
f_t = 5 MPa
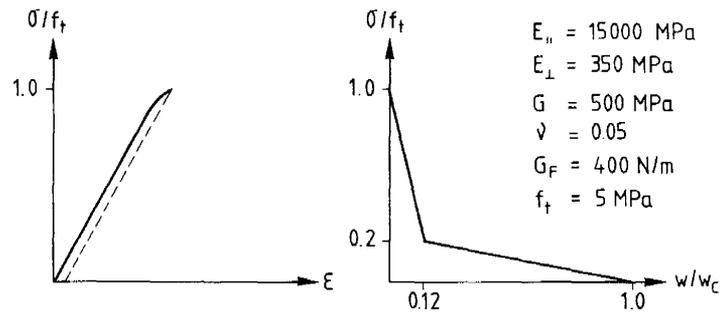
Figure 3.15 Material properties and softening relation used in FEM-calculation.
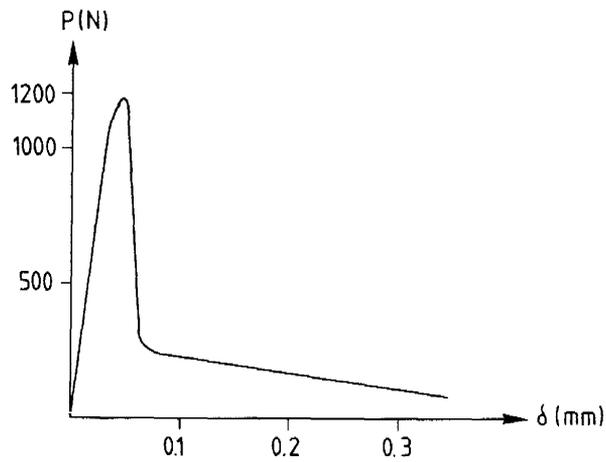
Figure 3.16 Calculated load-displacement and σ-w curve.

46

The tensile strength of the material can be calculated from the maximum load if the stress distribution over the crack propagation path is fairly even when the peak load is reached. In Figure 3.17 the calculated stress distribution is shown at peak load. According to this calculation the stress distribution is very even and varies at most less than 5%. The mean stress is 4.6 MPa. Consequently the maximum load can be utilized for calculation of the tensile strength of the material. This is also shown in the calculated load-displacement curve. The maximum load in the curve gives the tensile strength if divided by the ligament area.
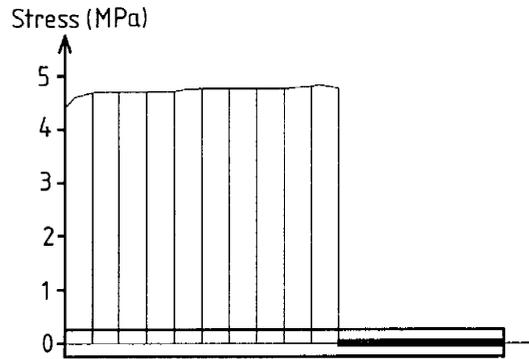
Figure 3.17 Calculated stress distribution over the crack propagation path at maximum load.

3.9 Interpretation of results

In order to measure the opening of the notch, clip-gauges were used. It was, however, impossible to mount these gauges directly into the notch, which is preferable; instead they had to be mounted on the steel-prismas on which the specimens were glued; see for example Figure 3.7. That is, the deformation of the glue line was also measured by the gauges. However, as long as the deformation in the glue line is elastic it would not influence the σ-w curve. As previously noted, there were problems with the curing of the glue, and if the curing time was insufficient, the result was plastic deformations and failure in the glue line. In the results presented, a curing time of at least three hours has been used and no plastic deformations in the glue have been observed.

In order to be certain that no failure occurred in the glue line, each specimen was visually inspected after the experiments, and all specimens with glue failures were excluded from the series. Accordingly there was an unavoidable selection where specimens with a high tension strength, higher than the glue, were dismissed. Figure 3.18 shows a photo of a specimen with partial glue failure. All specimens where some of the failure occured in the glue line have

been dismissed from the results presented here. However, in Appendix A a complete list of all results is presented.
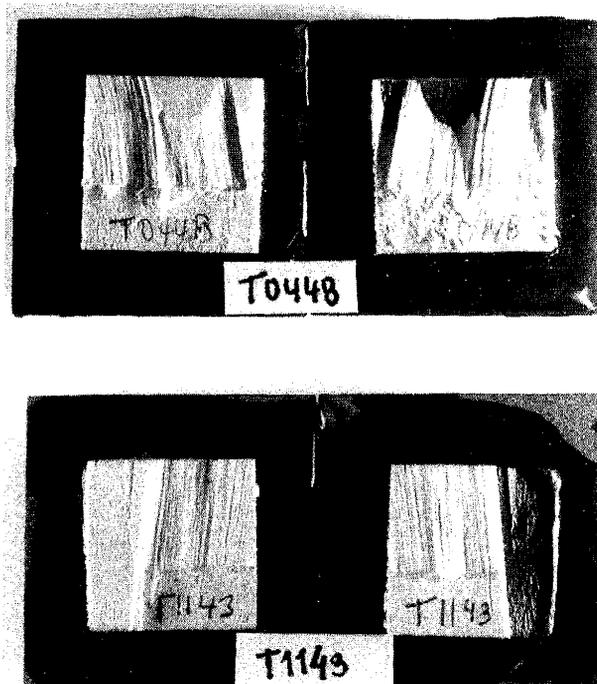
Figure 3.18. Specimen with partial glue failure.

Another factor that influences the measured results is the forces introduced to the testing arrangement by the clip-gauges. A clip-gauge acts as a spring, and thus introduces tension stresses in the specimen. The spring constant of each clip-gauge was measured to 6 N/mm. These forces from the gauges were added to the experimental results, even if they were so small that they would not influence the results. The introduced force from the clip-gauges was always less than 15 N and the maximum load in the experiment was normally more than 1000 N. There was also a spring mounted between the two beams in the testing arrangement. The purpose of this spring was to carry the weight of the lower beam under the specimen. The load introduced to the system by this spring was subtracted from the results.

All examination and transformation of the experimentally determined results was made with a computer program, MATLAB (1990). Different routines were written in the MATLAB language in order to compensate for the spring constants of the clip-gauges and the spring in the arrangement, determine the stress-displacement curve for the fracture process zone, the

σ-w curve, and finally to determine fracture energy and tensile strength or shear strength.

In order to determine the σ-w curve, only the slope of the ascending branch of the curve and the geometry of the specimen had to be given to the MATLAB program; see Figure 3.19. This line was then moved so it crossed the measured curve at the maximum point of the load. From this line, which acts as the new load axis, all displacements were calculated.
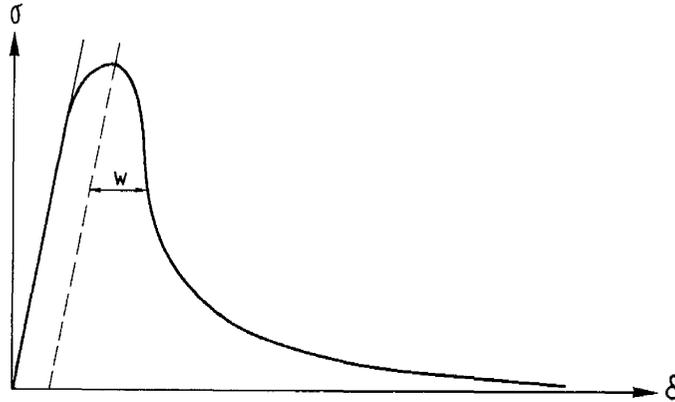
Figure 3.19 Calculation of σ-w curve from measured σ-δ curve.

The fracture energy is determined as the area under the σ-w curve. Routines were written in the MATLAB language that made it possible to determine the area in two ways. Firstly, a new curve represented by a number of straight lines could be drawn on top of the measured curve and the program calculated the area under the drawn curve. Secondly, the program calculates the fracture energy by using all the measured points of the curve.

The tension strength and the shear strength were determined from the maximum load as

$$f_t = \frac{P_{max, tension}}{A_0}$$

$$f_v = \frac{P_{max, shear}}{A_0}$$

(3.6)

3.10 Tension test results

More than two hundred experiments have been made in Mode I, about half of them in order to find a suitable specimen, a suitable glue and finally curing time for the glue. The results presented here are mainly from the final series made, after geometry and curing time had been established.

In Table 3.3 the mean values from each series are shown, and results for each specimen regarding fracture energy and tension strength can be found in Appendix A. The table also presents some of the introductory experiments.

Table 3.3 Mode I results

Moisture content (%)	Orientation	Fracture energy G_F (N/m)		Tensile strength f_t (Mpa)		Number of specimens
		mean	s.d.	mean	s.d.	
8	RL	460	115	5.3	1.1	14
8	45°	475	140	5.3	1.2	11
8	TL	550	70	4.1	0.3	4
10	RL	445	115	5.0	1.2	17
10	45°	515	125	5.3	1.4	6
10	TL	500	75	4.2	0.7	6
13	RL	535	100	4.5	0.8	11
13	45°	595	135	4.5	0.5	8
13	TL	460	105	4.0	0.4	6
26	RL	515	50	4.1	1.2	10
Laboratory	RL	380	90	6.8	1.1	7
Laboratory	30°	460	120	5.6	1.3	6
Laboratory	45°	505	95	5.5	0.9	16
Laboratory	TL	405	100	4.1	0.5	13

Note : The last four series presented in the table, i.e. the series with a moisture content expressed as "Laboratory", are some of the introductory experiments. These specimens were not conditioned in a controlled climate, and therefore the moisture content is unknown. The specimens were in equilibrium with the climate of the laboratory, and thus the moisture

50

content would be in the order of 10% to 15%.

The table shows that the scatter is extensive. It should be noted that the number of specimens in the series with a TL orientation is rather few. Nevertheless, if the scatter in fracture energy and tensile strength is extensive, the form of the softening curve is more constant. It will be shown later that the shape of an approximated σ-w curve is independent of moisture content and grain orientation, at least in the range of these tests. Figure 3.20 shows a number of measured load-displacement curves for specimens with a moisture content u=13% and in TL orientation.
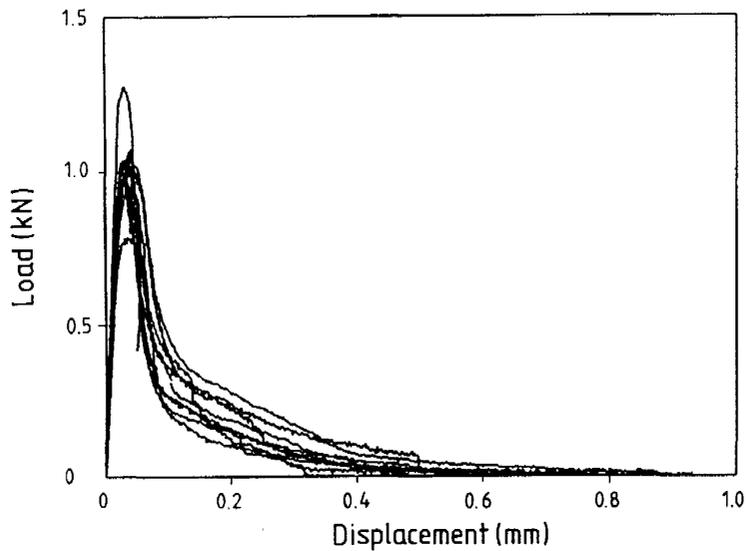
Figure 3.20 Measured load-displacement curves in TL direction and u=13%.

To make a comparison possible regarding the softening curve between the different series, a mean curve for each series was made. All curves in each series were plotted in one diagram and a mean curve was made. A number of points on the displacement axis were chosen, and at these points, a mean stress was calculated using the stress for the actual displacement from all tests in the series. This mean curve has the correct mean tensile strength, but not the complete tail. According to Petersson (1991) the first part of the softening curve is most important, especially when calculations are made on small structures as specimens. By making these mean curves the different series can be more easily compared. Figures 3.21 to Figure 3.24 show the mean softening curves for the different series examined.

σ(MPa)

RL-orientation
33% RH ⇒ u = 8 %
$\bar{G}_F$ = 460 N/m, s.d.= 115N/m
$\bar{f}_t$ = 5.3 MPa, s.d = 1.1 MPa
NOS = 14

5
4
3
2
1

0.1 0.2 0.3 0.4 0.5 0.6 w(mm)

σ(MPa)

45°-orientation
33% RH ⇒ u = 8 %
$\bar{G}_F$ = 475 N/m, s.d.=140N/m
$\bar{f}_t$ = 5.3 MPa, s.d = 1.2 MPa
NOS = 11

5
4
3
2
1

0.1 0.2 0.3 0.4 0.5 0.6 w(mm)

σ(MPa)

TL-orientation
33% RH ⇒ u = 8 %
$\bar{G}_F$ = 550 N/m, s.d.= 70 N/m
$\bar{f}_t$ = 4.1 MPa, s.d = 0.3 MPa
NOS = 4

5
4
3
2
1

0.1 0.2 0.3 0.4 0.5 0.6 w(mm)
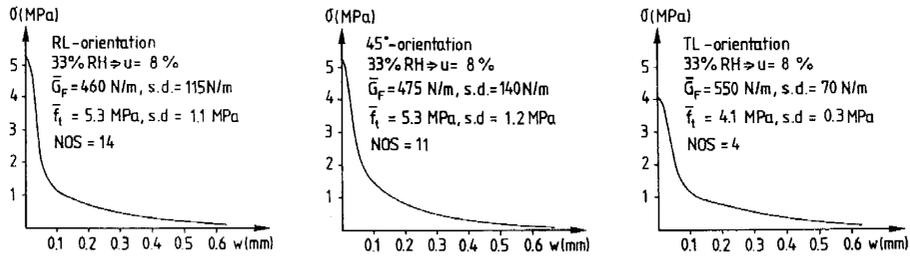
Figure 3.21 Softening curve, u=8%, *orientation*=RL, 45°, TL.

σ(MPa)

RL-orientation
59% RH ⇒ u = 10 %
$\bar{G}_F$ = 445 N/m, s.d.= 115N/m
$\bar{f}_t$ = 5.0 MPa, s.d = 1.2 MPa
NOS = 17

5
4
3
2
1

0.1 0.2 0.3 0.4 0.5 0.6 w(mm)

σ(MPa)

45°-orientation
59% RH ⇒ u = 10 %
$\bar{G}_F$ = 515 N/m, s.d.=125N/m
$\bar{f}_t$ = 5.3 MPa, s.d = 1.4 MPa
NOS = 6

5
4
3
2
1

0.1 0.2 0.3 0.4 0.5 0.6 w(mm)

σ(MPa)

TL-orientation
59% RH ⇒ u = 10 %
$\bar{G}_F$ = 500 N/m, s.d.= 75 N/m
$\bar{f}_t$ = 4.2 MPa, s.d = 0.7 MPa
NOS = 6

5
4
3
2
1

0.1 0.2 0.3 0.4 0.5 0.6 w(mm)
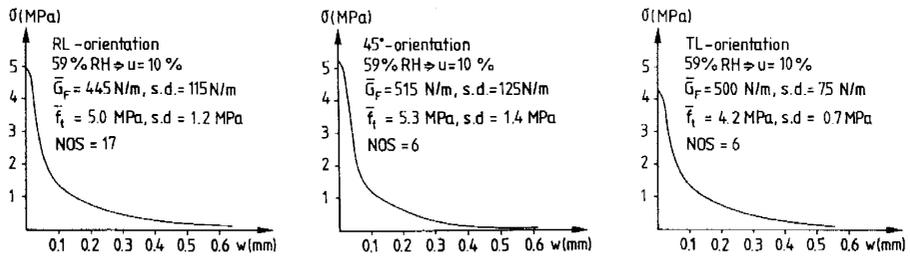
Figure 3.22 Softening curve, u=10%, *orientation*=RL, 45°, TL.

σ(MPa)

RL-orientation
75% RH ⇒ u = 13 %
$\bar{G}_F$ = 535 N/m, s.d = 100N/m
$\bar{f}_t$ = 4.5 MPa, s.d = 0.8 MPa
NOS = 11

5
4
3
2
1

0.1 0.2 0.3 0.4 0.5 0.6 w(mm)

σ(MPa)

45°-orientation
75% RH ⇒ u = 13 %
$\bar{G}_F$ = 595 N/m, s.d.=135 N/m
$\bar{f}_t$ = 4.5 MPa, s.d = 0.5 MPa
NOS = 8

5
4
3
2
1

0.1 0.2 0.3 0.4 0.5 0.6 w(mm)

σ(MPa)

TL-orientation
75% RH ⇒ u = 13 %
$\bar{G}_F$ = 460 N/m, s.d.=105N/m
$\bar{f}_t$ = 4.0 MPa, s.d = 0.4 MPa
NOS = 6

5
4
3
2
1

0.1 0.2 0.3 0.4 0.5 0.6 w(mm)
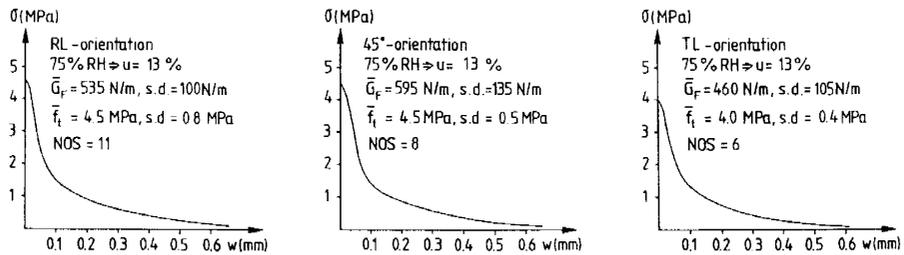
Figure 3.23 Softening curve, u=13%, *orientation*=RL, 45°, TL.

σ(MPa)

TL-orientation
97% RH ⇒ u = 26 %
$\bar{G}_F$ = 515 N/m, s.d.= 50 N/m
$\bar{f}_t$ = 4.1 MPa, s.d = 1.2 MPa
NOS = 10

5
4
3
2
1

0.1 0.2 0.3 0.4 0.5 0.6 w(mm)
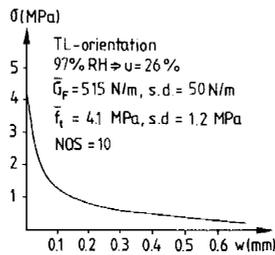
Figure 3.24 Softening curve, u=26%, *orientation*=RL.

52

With the intention to compare the different series, the softening curves were normalized, with respect to both stress and displacement. The normalized curves were made as bi-linear curves, i.e. the softening curves were approximated with two straight lines. The normalization procedure was as follows.

Two lines are drawn on top of the softening curve; see Figure 3.25. One line represents the first, steep, descending branch of the curve. This line starts at $\sigma = f_t$ and $w = 0$. A point on the line is chosen, to represent a break-point (σ_1, w_1). Now the final displacement of the two-line approximated softening curve can be calculated by

$$G_F = \frac{f_t w_1}{2} + \frac{\sigma_1 w_c}{2}$$

$$w_c = \frac{2 G_F - f_t w_1}{\sigma_1}$$

(3.7)

The second line can now be drawn from the chosen break-point to the calculated displacement w_c. If the bi-linear approximation differed from the original curve, a new break-point was chosen and a new approximation was made, until a satisfactory result was obtained. Figure 3.26 shows the normalized mean curves for all series.
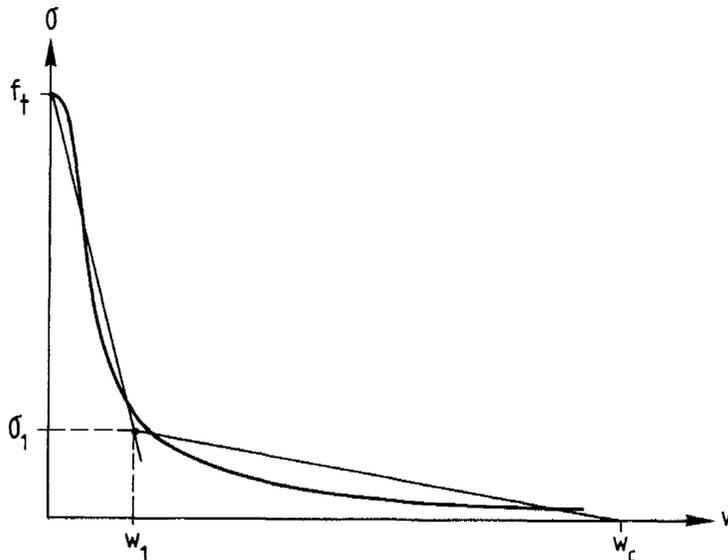
Figure 3.25 Approximation of σ-w curves.

53

According to these results, the form of the approximated softening curve is independent of both grain orientation and moisture content. Thus an approximated softening curve can be determined with a knowledge of tensile strength and fracture energy, both of which can easily be measured. The break-point of the curve is located at $(\sigma_1/f_t, w_1/w_C) = (0.20, 0.12)$. The location of the final displacement, w_C, can be calculated by

$$G_F = 0.16 f_t w_C \quad \Rightarrow \quad w_C = 6.25 \frac{G_F}{f_t} \tag{3.8}$$
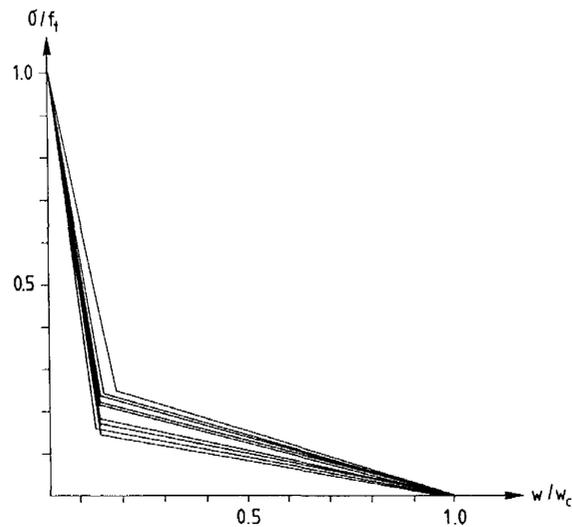
Figure 3.26 Normalized mean curves for all Mode I tests.

In Figure 3.27 the tensile strength is plotted as a function of moisture content. Three curves are shown, one curve for each orientation examined, and the standard deviation is plotted as vertical lines. The mean values decrease with increasing moisture content, but the scatter is too extensive to prove statistically significant variation in tensile strength with respect to the moisture content.

54
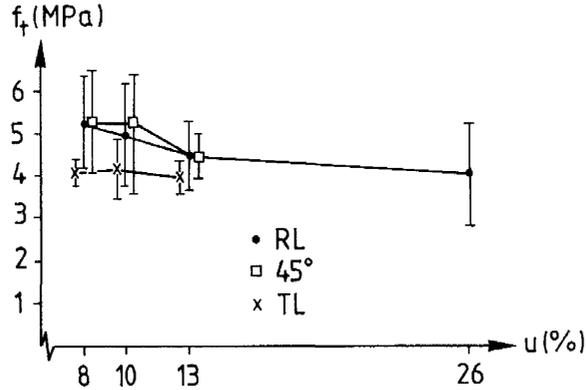
Figure 3.27 Tensile strength versus moisture content.

In literature the fracture toughness usually is examined, and the fracture toughness normally is calculated from the maximum load in the experiment. The experiments made in this study, however, are made on specimens where linear elastic fracture mechanics is not applicable. In order to compare values on fracture toughness and the fracture energy results presented here, the following relation can be used.

$$K_{IC} = \sqrt{G_F E^*}$$ (3.9)

where E^* is the orthotropic modulus of elasticity according to equation (3.10), Sih et al. (1965), where index x and y are principal directions and here represented as x=longitudinal direction (L), and y=direction perpendicular to the grain (R, T or 45°).

$$\frac{1}{E^*} = \sqrt{\frac{1}{2 E_x E_y}} \sqrt{\sqrt{\frac{E_x}{E_y}} + \left(\frac{1}{G_{xy}} - \frac{2 v_{yx}}{E_y}\right) \frac{E_x}{2}}$$ (3.10)

The modulus of elasticity has not been measured by standard methods for the material used for determination of the softening behaviour. However, an approximated value of the stiffness perpendicular to the grain has been determined from the tensile tests. These values have been obtained from the initial slope of the experimentally determined load-displacement curve as $E = \Delta Pl / \Delta \delta A_0$, where $l=3$ mm and A_0 is the area of the ligament. However, it should be noted that these values of the modulus of elasticity are not the true values, but they give an idea of the variation of the stiffness due to moisture content and grain orientation.

55

In order to determine the orthotropic stiffness, E^*, the modulus of elasticity in the grain direction, the modulus of elasticity perpendicular to the grain, the modulus of rigidity and Poisson's ratio have to be known. The modulus of elasticity perpendicular to the grain has been measured; see Table 3.4. Poisson's ratio has been chosen as $v_{yx}=0.05$. The modulus of elasticity in the grain direction and the modulus of rigidity are dependent on the moisture content, and the following relations were used to determine these parameters, Hillerborg et al. (1983).

$$E_L = 16000 - 100\,u$$

$$G_{LR} = 800 - 13.3\,u$$

(3.11)

where u is the moisture content where $0\% < u < 30\%$.

Table 3.4 Mode I results, fracture toughness and modulus of elasticity.

Moisture content (%)	Orientation	Modulus of elasticity E (MPa)		Fracture energy G_F (N/m)		Fracture toughness K_{IC} (kNm$^{-3/2}$)	
		mean	s.d.	mean	s.d.	mean	s.d.
7.6	RL	880	260	460	115	770	100
7.6	45°	860	290	475	140	790	180
7.6	TL	690	140	550	70	800	100
9.7	RL	760	250	445	110	730	180
9.7	45°	760	250	515	125	850	120
9.7	TL	770	230	500	75	780	140
13.8	RL	640	140	535	100	760	90
13.8	45°	670	170	595	135	820	170
13.8	TL	560	80	460	105	690	100
26.5	RL	700	180	515	50	720	100

Note: The modulus of elasticity given is the measured stiffness in the orientation given. The fracture toughness is, however, calculated from the orthotropic stiffness, E^*.

Even if the results obtained in this study are not general, but only show the characteristics of one board, a comparison is made with results from other researchers. In a round-robin test, fracture energy was measured from three-point bending experiments, Larsen and Gustafsson

56

(1990). The results from these tests are presented in Figure 3.28, and the results from the present study are shown in the figure as rings.
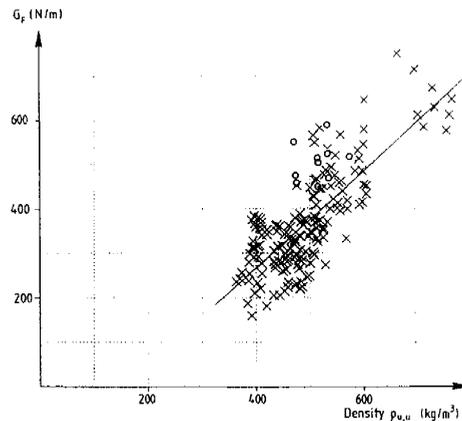
Figure 3.28 Fracture energy versus density, Larsen and Gustafsson (1990).

The density, for the specimens in the present study, has been approximately calculated as $\rho_{u,u}$, which is used in Figure 3.28. The fracture energy obtained here is higher than the fracture energy in the round-robin test. However, the values obtained are not extremely high, and fit into the cluster.

According to Petterson and Bodig (1983) the fracture toughness decreases with increasing moisture content. Ewing and Williams (1979) showed that the fracture toughness increased with moisture content up to around $u = 10\%$, and thereafter the fracture toughness decreased. The same behaviour was shown by Kretschmann et al. (1990).

In Figure 3.29 fracture toughness is plotted versus moisture content and no statistically significant tendencies can be found. However, when looking at the mean values, these results coincide, but only for the 45°-orientation, to the results obtained by the previously mentioned researchers. The RL orientation has an almost constant fracture toughness over a moisture content of $u = 10\%$. Below $u = 10\%$ the fracture toughness increases. For the TL-orientation, the fracture toughness decreases with increasing moisture content.

In the fracture energy measurements the scatter is too big to show any statistically significant variations regarding moisture content. However, some tendencies can be found in Figure 3.30. For the TL orientation the fracture energy decreases with increasing moisture content. On the other hand the fracture energy increases with increasing moisture content for the 45° orientation. The values for the RL orientation go up and down, so it is difficult to draw any conclusions.

57
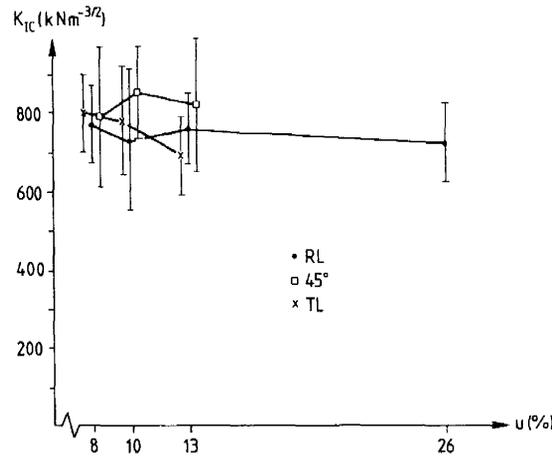
Figure 3.29 Fracture toughness versus moisture content.
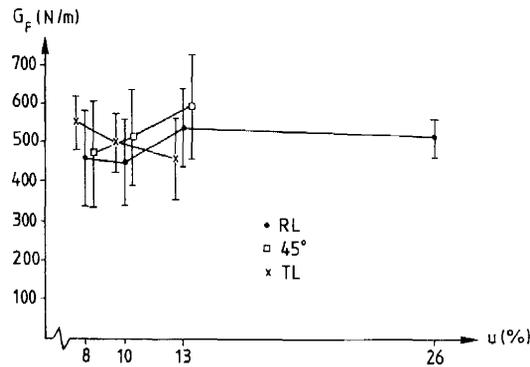
Figure 3.30 Fracture energy versus moisture content.

In a study by Riipola and Fonselius (1988), the critical value from the J-integral, J_c, was determined for spruce with a moisture content of $u = 10.9\%$, 12.3% and 14.6%. According to their study, the J-integral increases with increasing moisture content. The tests were made in TL orientation. Smith and Chui (1991) measured fracture energy by means of a three-point bending test on plantation-grown red pine. They examined the TL orientation and found that the fracture energy decreased with increasing moisture content from $u = 16\%$ to fibre saturation point.

The tendencies found for the TL orientation coincide with the results obtained by Smith and

Chui, i.e. that the fracture energy decreases with increasing moisture content. However, Riipola and Fonselius showed an opposite behaviour. Yet, the results obtained by Smith and Chui cannot directly be compared with the results obtained by Riipola and Fonselius and the actual results presented here. The moisture contents examined by Smith and Chui were much higher than the moisture contents used in this study and by Riipola and Fonselius. The results obtained in the present investigation, on the other hand, are uncertain because the number of specimens in the TL series was low.

3.11 Shear test results

In Mode II only one orientation and one moisture content was examined. The chosen orientation was RL, the examined moisture content was 13% and the density $\rho_{0,0} = 460 \text{ kg/m}^3$. More than 50 experiments were made before the main series was carried out. The introductory experiments were made in order to find a suitable geometry of the specimen and loading arrangement, and to find a curing time for the glue so no failures would develop in the glueline.

A single side notched specimen was examined in the introductory experiments. According to these tests, the crack started propagating from the notch and then propagated out into the glueline. Therefore a double sided notched specimen had to be used, to be sure that the crack propagated between the two notches. A disadvantage with the double sided notched specimen is that multiple cracks could develop. However, in the experimental series made, only a few specimens had multiple cracks, and these were dismissed from the series.

The geometry of the specimen was defined from the beginning, except for the width. A number of tests were made with a width of 10 mm, but these tests were always unstable. Therefore, a specimen with a shorter width, 3 mm, was chosen. With this short width the instability problem was overcome.

Another problem was the glue. The same type of two component glue as for the tension tests was utilized. In the first experiments the steel device on which the specimen is glued was constructed without the nick. However, with this construction the glue failed, so a nick had to be made. With the nick and a curing time for the glue of at least three hours no glue failures were observed.

One problem with shear tests is the difficulty of designing a test where only shear stresses are introduced, and with a well defined state of stress. In the chosen testing arrangement, see Figure 3.31, the stress distribution is reasonably even according to a FEM calculation. However, it was unavoidable to introduce tension or compression stresses with the testing arrangement used. Depending on the orientation of the steel pieces on which the specimen

59

was glued, a tension or compression load was introduced. The magnitude of this load was determined at around 10 N, both in tension and in compression.
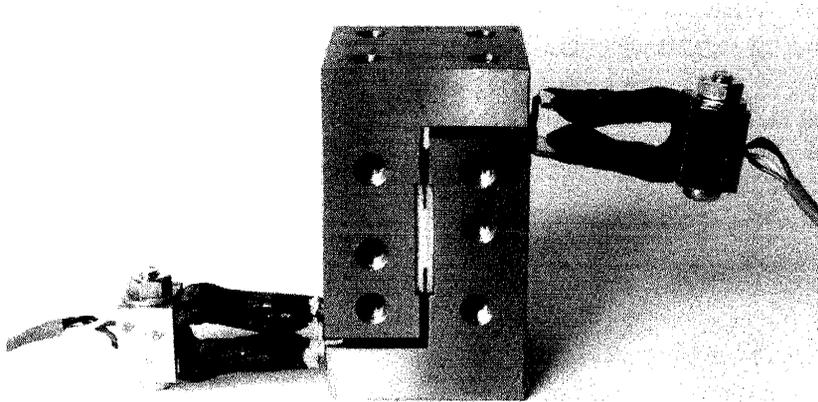
Figure 3.31 Testing arrangement for Mode II experiments.

Therefore a number of experiments were carried out where a known tension or compression load was applied. The tension or compression load used in these tests was chosen as $P = \pm 20$ N. Thus the ratio between maximum shear load and applied tension or compression load was always greater than 50. Four tests were made with a tension component and four with a compression component. A comparison was made between specimens with a tension component and specimens with a compression component, and there was no significant difference between them.

According to the results presented in Table 3.5, there is a some difference between tests with a tension component and tests with a compression load. However, these differences are small and therefore these experiments are regarded as pure shear tests, even if there is a small component of tension or compression.

The results from the shear tests are shown in Figure 3.32. In contrast to the Mode I tests, the scatter is much less in the Mode II tests regarding the form of the softening curve. The mean fracture energy from these experiments is $G_{F,II} = 815$ N/m and with a standard deviation of 150 N/m, all results from the series can be found in Appendix E. The mean shear strength was determined as $f_v = 11.0$ MPa with a standard deviation of 0.8 MPa. The shear strength coincides well with values found in the literature, e.g. Kollmann (1951).

60

Table 3.5 Effect of tension or compression load on Mode II fracture energy

Load P (N)	Fracture energy G_F (N/m)	Shear strength f_v (MPa)
20 (Tension)	870	10.1
20 (Tension)	800	11.4
20 (Tension)	770	11.8
20 (Tension)	790	10.2
Mean	810	10.9
s.d.	40	0.9
20 (Compression)	780	9.6
20 (Compression)	910	10.9
20 (Compression)	860	11.7
20 (Compression)	840	11.3
Mean	850	10.9
s.d.	50	0.9

Figure 3.32 Experimentally determined τ-v curves.

According to a literature survey, fracture energy has not been measured in Mode II. All results published are stress intensity factors. In order to compare the present results, a stress intensity factor has been determined from the measured fracture energy by

$$K_{IIC} = \sqrt{E_{II}^* \, G_{F,II}}$$

(3.12)

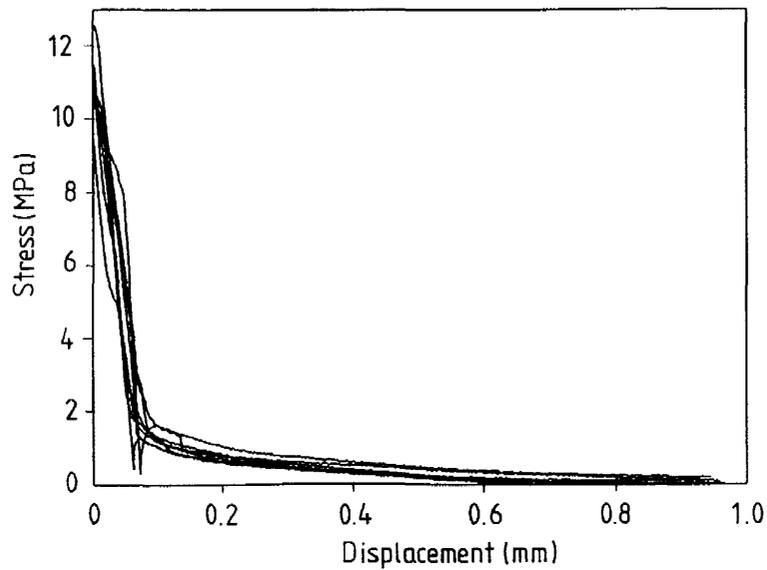where E_{II}^* is the orthotropic stiffness in Mode II. According to Sih et al. (1965) a relation can be derived between the Mode I and Mode II orthotropic stiffnesses.

$$\frac{E_I^*}{E_{II}^*} = \sqrt{\frac{E_x}{E_y}}$$

(3.13)

where in this case x=grain direction and y=radial direction. By using the stiffness properties $E_L = 15000$ MPa, $E_R = 700$ MPa, $G_{LR} = 700$ MPa and $v_{RL} = 0.05$ an orthotropic stiffness for Mode II can be determined. The critical stress intensity factor is hence determined as $K_{IIC} = 500 kNm^{-3/2}$. This stress intensity factor is much less than values obtained by other researchers, e.g. Valentin et al. (1991). A normal figure for the stress intensity factor found in the literature is $K_{IIC} = 2000$ kNm$^{-3/2}$.

A possible explanation for the big difference in fracture energy can be the size of the specimen. The specimens used in this study are very small, and the path where the crack propagates is a straight line. But if a large specimen is used, the crack propagation path is usually not straight, but jumps from annual ring to annual ring. The fracture surface is therefore much larger for a large specimen than for a small specimen. This occurs even if the critical stress intensity factor is determined from, for example, the maximum load. In this case no real crack has started to propagate, but rather a fictitious crack. If now the path for the fictitious crack is very rough, and not straight as in the small specimens, the amount of energy the specimen can store is larger, and subsequently the maximum load will be larger.

The curves shown in Figure 3.32 are different from the Mode I results in the sense that they are almost perfectly bi-linear. Valentin (1991) suggested that the curves show two different events. The first part of the curve, the steep descending branch, is the real fracture. The second part of the curve is some sort of friction or fibre pull-out. If this is true, the fracture energy in Mode II would be of the same order as for Mode I. However, it is impossible to tell from this study if there are two different events or not.

4 Examination of the Compact Tension Specimen

The Compact Tension (CT) specimen was originally developed for determination of the critical stress intensity factor or fracture toughness in Mode I on metals. This method is accepted today as one of the standard methods for metals, ASTM (1981). However, the method is also widely used for determination of critical stress intensity factors of wood, and then the question arises, "Is the CT test a suitable method for orthotropic materials like wood?". The intention of this investigation is not to give an absolute answer to the question, but rather to show the usefulness of nonlinear fracture mechanics and, hopefully, to start a discussion regarding testing methods for determination of fracture mechanics properties of wood.

When measuring material properties, it is of greatest importance that from the output of the experiment the material property can be determined. This is not always the case. Therefore it is important to deeply examine a testing method before it is accepted as a standard method or universally accepted. Consequently it can be very dangerous to directly adopt a method developed for a completely different material, which is the case with the CT specimen and its use on wood.

Because of the completely different behaviour of wood, as compared to metals, a comprehensive study of the testing arrangement has to be performed. This study is made in order to find out how the different properties, as compared to those of metals, might affect the applicability of the test method and to show the advantages of nonlinear fracture mechanics, especially the fictitious crack model.

With the CT specimen, the fracture energy can be measured. In the experimental series made, both fracture energy and critical stress intensity factor were determined.

4.1 Experimental study of the Compact Tension specimen

An experimental series was made in order to obtain data for the theoretical analysis, and to get results with which the theoretical results could be compared. The test series were made of seven different sizes of the specimen, while all other parameters were kept constant. There are of course other parameters that may drastically influence the results, like moisture content, temperature and loading rate. However, it should be noted that the loading rate was constant for the piston. That is, the loading rate in the fracture process zone alters for different geometries. However, in the actual series all these parameters were kept constant, and only the size of the specimen was altered. The normalized effective notch depth for all specimens was $a/(W+a)=0.5$, which is the prescribed notch depth according to ASTM.

63

Figure 4.1 displays the geometry of the standard CT specimen.
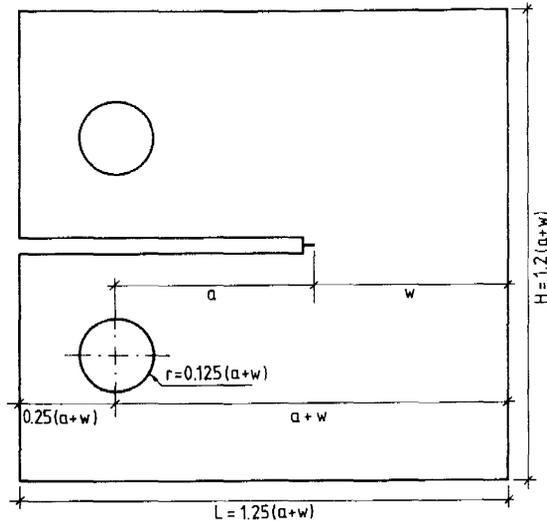
Figure 4.1 Geometry of the CT specimen, ASTM (1981).

4.1.1 Specimen preparation

The specimens were manufactured from Scots pine timber. Unfortunately the material used in these series is not the same as the material used for determination of the softening behaviour in the previous chapter.

When the specimens were sawn, a notch was cut to a depth of 0.9 times the total effective notch depth. Thereafter the specimens were kept in a conditioning chamber. After the conditioning, just before the test, the remaining 10% of the notch was made with a razor blade.

Only one grain orientation was examined, and the orientation chosen was radial-longitudinal (RL), i.e. the crack propagates along the grain and the normal to the crack plane is in the radial direction of the annual rings; see Figure 1.1. Because of the cylindrical growth of wood, it was impossible to find sufficient good pieces of wood for the larger specimens, the specimens with a total length of 75 mm and 100 mm. Therefore these specimens were glued from three pieces of wood, where the middle piece had the correct RL grain orientation, see Figure 4.2. The effect of this procedure on the results has not been considered.

64

The specimens were conditioned two months in a climate chamber at 20°C and 65% RH. The moisture content and density of each specimen were measured immediately after the test. Moisture content was determined by weighing the specimen after the test and then drying it in an oven at 105°C for two days, and afterwards measuring the dry weight. For the whole population the moisture content was $u=13\%$ with a standard deviation of 1%, and the density was determined as $\rho_{0,13}=410$ kg/m^3 with a standard deviation of 22 kg/m^3. All results are presented in Appendix C.

In these experimental series only size dependencies were examined and no other parameters. To examine the size dependency of the specimen seven different geometries were chosen; see Table 4.1. The "standard" width of the specimen, according to ASTM, is 0.4 times the total length of the specimen, but in this investigation a width of 0.3 times the total length was also examined.

Table 4.1 Geometry of CT specimens.

Notch length a (mm)	Ligament length W (mm)	Specimen width B (mm)
10	10	10
20	20	10
20	20	20
30	30	20
30	30	30
40	40	30
40	40	40

4.1.2 Experimental setup

In the test series made, a MTS 810 testing system was used. The loading was made in displacement control, i.e. the feed-back signal was transmitted from displacement gauge placed on the piston. The stroke velocity for all specimens was set at to 0.6 mm/minute. The displacements of the specimen were measured both by the movement of the piston, i.e. the stroke, and by clip-gauges mounted at different positions on the specimens. The number and position of clip-gauges differed among specimens because of their different sizes. On the smallest series, no clip-gauges were used, and on the largest series, four clip-gauges were mounted at different positions in the pre-made notch. In Figure 4.2 the position of the clip-

gauges is shown for two specimens.
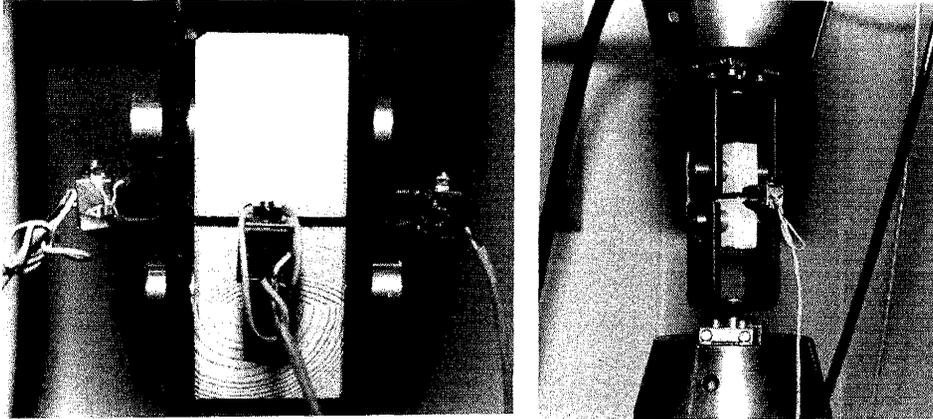
Figure 4.2 Position of clip-gauges.

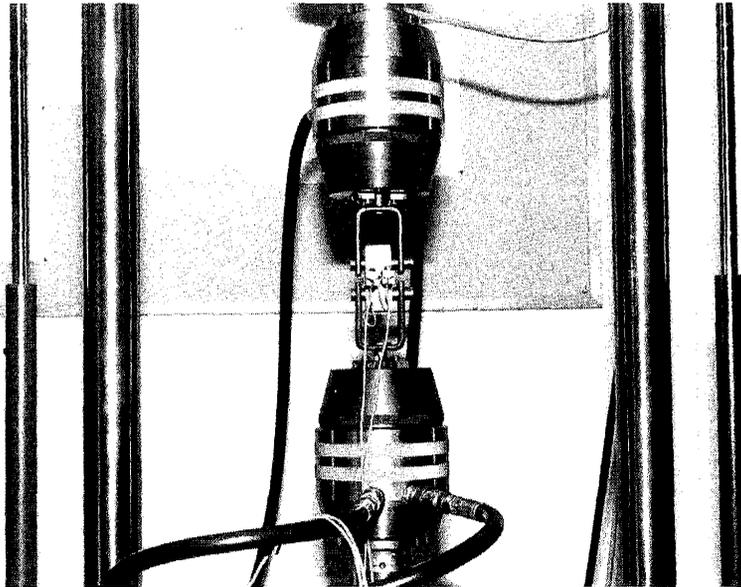*Figure 4.3 Experimental setup.*

The load was measured with a 2 kN load-cell for all series except the series with the smallest specimens, where a 100 kN (!) load-cell was used. Consequently the results from the smallest series do not have the same accuracy as the other series. The 100 kN load-cell was used by mistake. In order to control the accuracy of the big load-cell, it was calibrated with weights

according to the small loads obtained with the smallest specimens. According to this calibration the error was of such size, $\pm 10\%$, that it was not negligible. Nevertheless, the smallest series is presented here, and these results should be regarded carefully.

In the test, displacement has to be measured at the loading point of the specimen for later determination of fracture energy. Displacements measured at other points on the specimen are not to be used for determination of fracture energy. For other materials or other geometries of specimens it might be possible to calibrate displacement measurements at other points, such as the notch, and from here determine the displacement in the loading point. However, the results from these test series showed that the relation between displacement measurements in the notch and displacement measurements at the loading point were not linearally related, which might depend on the friction between the steel bolt and the specimen.

There can be problems measuring the displacement at the loading point. Usually the movement of the piston is measured. If the arrangement between the piston and the loading point on the specimen does not have a sufficient stiffness, additional deformations will be measured. However, when the specimen is unloaded these additional deformations will also go back if the arrangement is elastic, and a correct fracture energy can be determined. On the other hand, if there are plastic deformations in the loading arrangement, the result will be wrong. In these tests the measurements were recorded from the movement of the piston. However, the arrangement between the piston and the loading point on the specimen was examined with respect to extra displacements due to plasticity in the arrangement, and according to these tests, no plastic deformation was observed.

4.1.3 Interpretation of the results

Usually when the CT tests are made for determination of critical stress intensity factors, only the load when the crack starts propagating is interesting. However, in this study the fracture energy was also determined, and thus the complete load-displacement curve has to be measured. It is necessary that the experiment is completely stable during the test. The CT specimen is a good specimen in that sense, but a stiff testing arrangement is preferable.

To determine the fracture energy from the test, the complete load-displacement curve is used, even the descending branch of the curve. The fracture energy is thus equal to the area under the complete curve divided by the ligament area of the specimen. This is valid as long as the material outside the fracture process zone behaves elastically.

$$G_F = \frac{1}{A_0} \int P \, d\delta \tag{4.1}$$

where A_0 = ligament area

$\quad\quad$ P = load

$\quad\quad$ δ = displacement in the loading point

As previously noted in Chapter 3, a clip-gauge acts as a small spring on the specimen. Therefore corrections on the recorded load-displacement curve had to be made due to the forces introduced in the specimens by the clip-gauges. The spring constant of each clip-gauge was determined as 6 N/mm.

The CT specimen is a very suitable specimen for fracture energy measurements in the sense that there are usually no problems with instabilities. But on the other hand, the tail of the load-displacement curve is very long and thus the area under the curve is difficult to measure. For example, a specimen with a total length of 100 mm is not completely unloaded before the displacement has reached around 60 mm. Even if the load is very small when the displacement has exceeded a couple of millimetres, it makes a contribution to the energy consumed during the crack propagation. There are, however, methods which can be used in order to avoid the problem of these long tails, which will be discussed later.

When determining critical stress intensity factors with the CT specimen, only the load when the crack starts propagating is measured. Thereafter the critical stress intensity factor is calculated from the series, Rolfe and Barsom (1977)

$$K_{IC} = \frac{P}{B\,(W+a)^{-1/2}} \left[29.6 \left(\frac{a}{W+a} \right)^{1/2} - 185.5 \left(\frac{a}{W+a} \right)^{3/2} \right.$$
$$\left. + 655.7 \left(\frac{a}{W+a} \right)^{5/2} - 1017.0 \left(\frac{a}{W+a} \right)^{7/2} + 638.9 \left(\frac{a}{W+a} \right)^{9/2} \right] \tag{4.2}$$

Equation (4.2) was derived for an isotropic linear elastic material. Even if the equation was not developed for materials like wood, it is still universally used. In order to estimate the error by assuming isotropic material, an FEM analysis was made. The size of the studied specimen was according to ASTM with a notch length a=20 mm and a/(W+a)=0.5. The modulus of elasticity for the isotropic case was E=350 MPa and the orthotropic modulus of elasticity, according to equation (3.10), E*=735 MPa. The element length was 1 mm and the compliance method was employed for calculation of the stress intensity factor. That means two calculations were made, for both the isotropic and the orthotropic case. The symmetry

68

of the specimen has been used and thus only the upper half of the specimen is modelled. In the first calculation the compliance was determined for a specimen with a crack length $a_1 = 20$ mm. In the second computation, the compliance was determined for a specimen with a crack length of $a_2 = 21$ mm. The released strain energy is then

$$G = \frac{P^2 (C_2 - C_1)}{2 B (a_2 - a_1)}$$

(4.3)

where   C = compliance
      P = load
      B = width of the specimen
      a = notch length

By normalizing the compliance with modulus of elasticity and specimen width, i.e. $C_{norm} = C \cdot E \cdot B$, and crack length with effective specimen length, i.e. $a_{norm} = a/(W+a)$, and by using the relation $K^2 = EG$ the stress intensity factor can be determined. According to these analyses, the following expressions were found

$$K_{I,orth} = \frac{P_{max}}{B \sqrt{W+a}} 9.2426$$

(4.4)

$$K_{IC,isot} = \frac{P_{max}}{B \sqrt{W+a}} 9.8995$$

(4.5)

which can be compared to equation (4.2) with the same relative notch length

$$K_{I,eq(4.6)} = \frac{P}{B \sqrt{W+a}} 9.6033$$

(4.6)

According to equations (4.4) and (4.5), by using an isotropic assumption, the calculated stress intensity factor will be overestimated by around 7% compared to an orthotropic assumption. However, there are also other errors that may occur when determining the stress intensity factor. If the length of the fracture process zone is not negligible, the stress intensity factor will be underestimated.

In the ASTM standard the maximum load is not always used for determination of the critical stress intensity factor. Fonselius (1986) published a procedure for determination of K_{IC} where a plasticity at the crack tip was assumed. The method is similar to the procedure used for

metals, where a compensation is necessary for yield deformations at the crack tip. Even if this procedure in principle is not applicable to wood, and underestimates K_{IC}, it has been used here. The method from Fonselius (1986) is as follows.

The maximum load P_{max} is located in the recorded load-displacement curve. Then two points are marked on the curve where the load is equal to $P_{max}/10$ and $P_{max}/2$. A straight line is drawn through these two points; see Figure 4.4. The slope of this line is then decreased by 5%, and a new line is drawn from origo with the calculated slope. The point where this new line crosses the original curve is the location of a load called P_Q. This load is utilized for determination of the critical stress intensity factor, i.e. $P = P_Q$ in equation (4.2). However, there are restrictions on this method. The ratio between P_{max} and P_Q must fulfil the relation $P_{max}/P_Q \leq 1.20$.
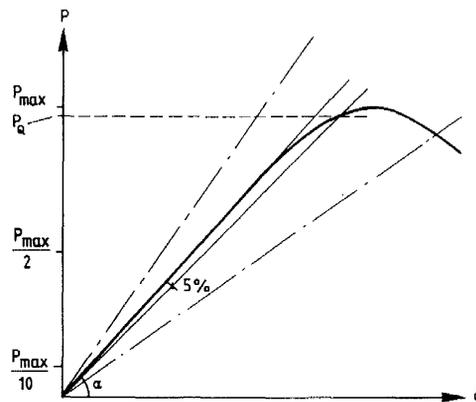
Figure 4.4 Method for finding the load used for determination of K_{IC}, Fonselius (1986).

Both critical stress intensity factor and fracture energy are regarded as material properties, and if this is true, there would be a relation between these two parameters. There exists a theoretical relation derived by linear elastic assumptions, see Chapter 2 equation (2.27) and (2.29), and this relation has been further improved by Sih, Paris and Irwin (1965) for orthotropic materials. They gave a relation with which an orthotropic stiffness could be determined, equation (3.10).

According to equation (2.27) and (2.29), the stress intensity factor can be calculated if fracture energy and stiffness are known. By using the orthotropic stiffness, the critical stress intensity factor is thus

$$K_{IC} = \sqrt{G_F E^*} \qquad\qquad (4.7)$$

In this study, it was impossible to determine all stiffness parameters, so the relation between stress intensity factors and fracture energy is only used to compare the scatter in the three methods.

To compare the two different material properties, critical stress intensity factor and fracture energy, equation (4.7) was used. From the measured fracture energy and an assumed orthotropic stiffness, a critical stress intensity factor was calculated. The difficulty with this technique, as mentioned before, is the choice of orthotropic stiffness parameters. In this report, the parameters were chosen according to normal values found in the literature, Kollmann (1951).

$E_L = 12000$ MPa

$E_R = 460$ MPa

$G_{LR} = 1000$ MPa

$v_{RL} = 0.05$

and thus

$E^* = 1060$ MPa

4.1.4 Experimental results

The results from the experimental series are assembled in Table 4.2, where $K_{IC,calc}$ is the critical stress intensity factor calculated from the fracture energy measurements, using equation (4.7). Each series contained six specimens, except for the smallest specimens where the series contained seven specimens. All results are presented in Appendix C.

According to the results, regarding the scatter of the total population, there is no big difference between measurements of critical stress intensity factors and fracture energy. If the whole population is considered, the scatter in the two parameters is on the same order, around 10%. There is, of course, a difference when regarding the absolute values in the measurements, but this probably depends on the stiffness parameters used in equation (4.7).

For the different geometries there is a divergence. In the individual series the scatter is greater for the critical stress intensity factor measurements than for the measurements of fracture energy. An explanation for the greater scatter in the K_{IC} measurements can be that there were probably errors when choosing the load for determination of K_{IC}. This would give wrong values for the critical stress intensity factor, and the problems regarding choice of load will be shown later in the theoretical study. For the fracture energy measurements the scatter was much less in the individual series than in the total population. An explanation may be that

a size dependency exists when measuring fracture energy on the CT specimen.

Table 4.2 Experimental results from Compact Tension tests.

a	B	G_F	sd	$K_{IC,calc}$	sd	$K_{IC,orth}$	sd	$K_{IC,iso}$	sd	$K_{IC,eq4.6}$	sd	$K_{IC,Fons}$	sd
40	40	227	23	490	29	317	7	340	8	330	8	317	9
40	30	220	21	483	28	334	38	358	41	347	40	330	30
30	30	191	14	450	19	293	35	314	37	305	37	298	38
30	20	230	11	494	14	300	20	321	22	312	21	309	24
20	20	165	12	418	18	342	16	366	17	356	16	306	27
20	10	174	54	430	80	345	28	371	31	358	29	346	24
10	10	233	21	497	26	327	36	350	38	340	37	332	9
		206	36	467	51	323	32	346	35	335	33	320	31

Note: a = effective notch length (mm)

B = width (mm)

G_F = fracture energy (N/m)

$K_{IC,calc}$ = fracture toughness calculated from measured fracture energy (kNm$^{-3/2}$)

$K_{IC,orth}$ = fracture toughness based on equation (4.4) (kNm$^{-3/2}$)

$K_{IC,iso}$ = fracture toughness based on equation (4.5) (kNm$^{-3/2}$)

$K_{IC,eq4.6}$ = fracture toughness based on equation (4.6) (kNm$^{-3/2}$)

$K_{IC,Fons}$ = fracture toughness according to the Fonselius method (kNm$^{-3/2}$)

In Figure 4.5 the critical stress intensity factor is plotted versus length of the specimen. The diagram only shows results from the series with a thickness to length ratio of 0.4. There are two curves in the diagram, one curve for K_{IC} based on equation (4.4), and one curve based on equation (4.7) where fracture energy has been measured. The diagram could of course have been plotted with fracture energy on the y-axis instead of critical stress intensity factor. The only difference would then be the scatter, because of the quadratic relation between stress intensity factor and fracture energy. The reason why stress intensity factor has been chosen is to minimize the scatter in the diagram.

Even if there is a big scatter, as there usually is when measurements are performed on wood, some observations can be based the present results.

- The scatter is bigger for K_{IC} measurements than for G_F in the individual series.
- There might be a size dependency in the G_F measurements.
- The absolute values of fracture energy are lower than those found in the literature, Valentin et al. (1991), while the measured stress intensity factors agree well
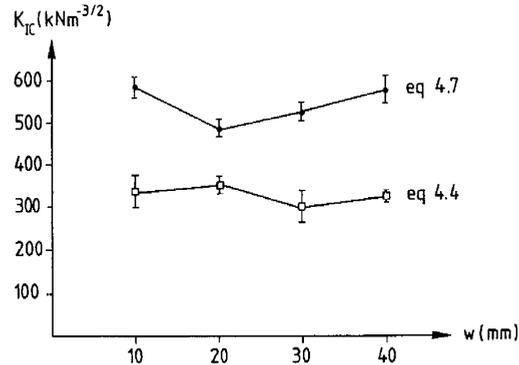
with values in literature.

Figure 4.5 Critical stress intensity factor versus length of specimen.

The measurements of fracture energy show a statistically significant size dependency on the 0.05 level, *if* the smallest series, the 25 mm specimens, is dismissed. As mentioned earlier, the data for the smallest series are very unreliable, because the load-cell used was far too big for the small loads obtained with these small specimens. Therefore these tests show a significant size dependency in the measurements of fracture energy. The fracture energy increases with increasing size of the specimen. However, it is important to note that the experimental series was small, and to get truly reliable results a much larger experimental series has to be carried out.

In the stress intensity factor measurements the scatter was much greater, and no statistically significant size dependency could be found. However, when looking at the mean values from the different series, they show a decreasing stress intensity factor with increasing size of the specimen. But the scatter is too great to statistically prove a size dependency.

One interesting observation is that the values for the fracture energy are much lower than the values found in literature, and that the values on stress intensity factors show good agreement with literature, Valentin et al. (1991). The fracture energy is around 200 N/m, while a formal figure on fracture energy for the same species is in the range 300-500 N/m. However, in a round-robin test, Larsen and Gustafsson (1990), where a three-point bending test was analysed, it was found that there is a large scatter, and that the values obtained here not are completely out of the range. In Figure 4.6 the results from the round-robin test are presented, and in this figure the results obtained here have been plotted as small circles.
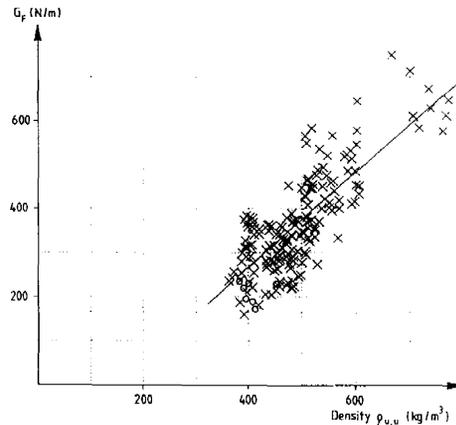
Figure 4.6 Results from a round-robin test with a three-point bending test, Larsen and Gustafsson (1990). The circles represent results obtained here.

Another explanation for the low values for the fracture energy is the difficulties of measuring the complete load-displacement curve on the CT specimens. The curve was normally cut at around 5 mm displacement at the loading point, but the specimen was able to transfer load up to a displacement of around 60 mm for the largest specimens. When the curve is cut, all energy in the tail of the curve is dismissed and the measured value of fracture energy would be less than the true value. The amount of energy the tail of the curve consists of is difficult to tell. The last 90% of the curve was almost impossible to measure. The ratio between maximum load and load after 4 mm displacement was on the order 1/50.

There are methods which can be used to make the determination of fracture energy easier, and probably more accurate, than when using the whole tail of the load-displacement curve. In the proposal by RILEM (1985) for determination of fracture energy of concrete by three-point bending tests, a method developed by Petersson (1981) was used. The method cuts the tail of the curve and an approximative value of the fracture energy can be determined. This approximative method probably gives better results than when the complete load-displacement curve is used, due to the difficulties measuring the very small loads in the tail. The method was developed for three-point bending tests and the CT test is very similar; the method would therefore be usable for the CT tests.

In Figure 4.7 the result from a CT test is shown. The area corresponding to the total fracture energy can be divided into three parts. That means, in the complete load-displacement curve, a load, P_1, is chosen where a new coordinate system with the same scale is drawn. At the point where the descending branch of the load-displacement curve crosses the new

74

displacement axis the displacement δ_0 is located. The area A_1 can easily be determined from the plot, and the area A_2 can be calculated by

$$A_2 = P_1 \delta_0 \qquad\qquad (4.8)$$

It can be shown that the area A_3 is approximately equal to the area A_2, Petersson (1981), so the total fracture energy can be determined as

$$G_F = \frac{A_1 + 2 P_1 \delta_0}{B W} \qquad\qquad (4.9)$$

This approximation is valid if the stress-strain curve for the material is almost linear up to failure. Otherwise too much energy is absorbed outside the fracture process zone, which is the case for metals.
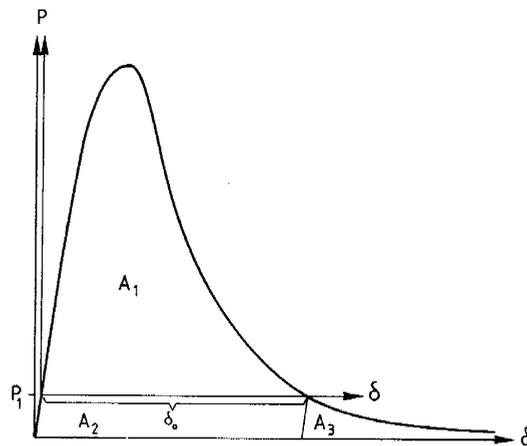
Figure 4.7 Method for determination of fracture energy from CT tests.

The computations, discussed later, indicated that the load-displacement curve is very sensitive regarding tensile strength, modulus of elasticity perpendicular to the grain and fracture energy. Therefore additional measurements had to be performed in order to determine tensile strength and modulus of elasticity perpendicular to the grain. The pieces left over from the CT tests were used for these measurements; see Figure 4.8. Only two of the different series could be used for these experiments, the specimens with a total length of 50 mm and depths of 10 and 20 mm. The other series were either too small or glued from different pieces. In

the tensile tests, the specimens were glued to a loading arrangement free of moments. The specimens had a reduced cross sectional area in order to get failure in the wood. Prismatic specimens were utilized for determination of modulus of elasticity in tension. These specimens were glued into the testing arrangement. Moreover, with some prismatic pieces compression tests were made, where the modulus of elasticity in compression was measured. According to the tensile tests, the strength perpendicular to the grain was $f_t = 6$ MPa, and the modulus of elasticity perpendicular to the grain was determined at $E_R = 180$ MPa. In the compression tests the modulus of elasticity perpendicular to the grain was determined at $E_R = 320$ MPa. There was a great scatter in the measurements of modulus of elasticity; the values varied from 90 MPa up to 490 MPa, see Appendix D.
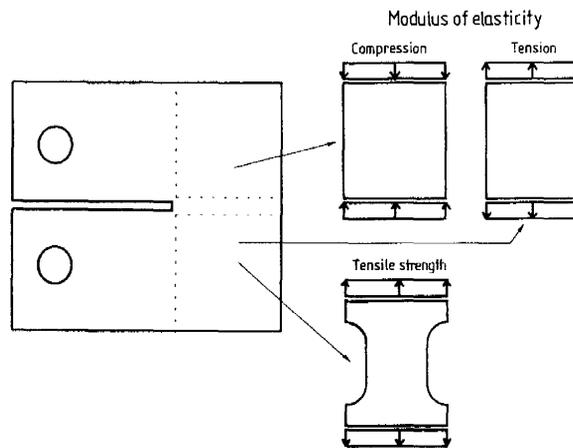
Figure 4.8 Material utilized for determination of tension strength and modulus of elasticity.

4.2 Theoretical study of the Compact Tension specimen

As mentioned earlier, the CT specimen is widely used for determination of the critical stress intensity factor of wood. No critical investigation of the specimen nor of the testing arrangement, when used on wood, has been located in a literature survey made. It is obvious that the testing arrangement and the behaviour of the specimen have to be examined because of the completely different behaviour of wood as compared to metals, for which the method was developed.

With the fictitious crack model, it is possible to follow a crack when propagating through the material. It is then possible to see when a real crack, with no stress transferring abilities, start developing in the specimen, and to see where on the load-displacement curve this happens.

The critical stress intensity factor can be calculated if the stress distribution along the crack propagation path is known at maximum load, and the maximum load can be utilized. By assuming a plastic behaviour of the material according to the Dugdale model, see for example Hellan (1984), a new notch length can be determined which is approximately the original notch length plus half the length of the fracture process zone. The critical stress intensity factor can thus be determined with equation (4.4) where the maximum load is used and the notch length is the original notch length plus half the length of the fracture process zone according to a FEM analysis with the fictitious crack model.

In this study not only the theoretical load-displacement curve has been determined, but also the behaviour of the loading point, the influence of the form of the softening curve and how sensitive the output is regarding the material parameters used as input to the calculations.

4.2.1 FEM modelling

To apply the fictitious crack model, a numerical method is necessary, and here the finite element method is utilized. The finite element program used was CAMFEM, developed by Dahlblom et al. (1985). In order to automatize the computations some original routines have been developed. The big advantage of CAMFEM is the openness of the program, i.e. it is very simple to make your own problem-related routines and link them to the finite element code.

The elements used in the calculations were four node orthotropic isoparametric elements, and the crack propagation path had 21 nodes; see Figure 4.9. All nodes except the node in the loading point and the nodes along the crack propagation path were condensed in order to save computer space and minimize computing time. The fracture process zone and the crack propagation path were modelled by elastic springs. The stiffness of the springs was chosen according to the state of the node. In the elastic state, i.e. before the tensile strength had been reached, the springs had a near infinitely high stiffness. After the tensile strength had been reached, and the state of the spring was softening, the stiffness of the spring was chosen according to the softening curve; see Figure 4.10 and 4.11. When a real crack, without stress transferring abilities, had developed the stiffness of the spring was zero. It should be noted that these calculations were made before the softening curves shown in Chapter 3 were determined.

P

Hole

B

Steel bolt

P
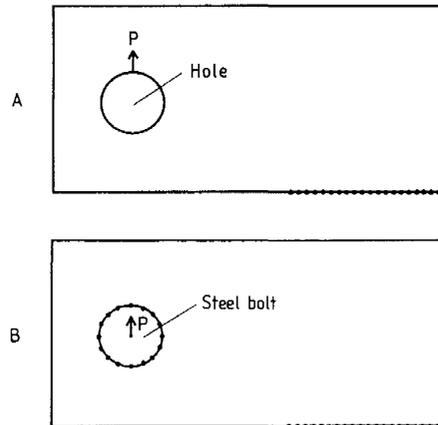
Figure 4.9 Element mesh. Loading case a) without steel bolt b) with steel bolt

In the calculations plane stress condition was assumed. The material properties were chosen according to the literature, Hillerborg et al. (1983) and Bodig and Jayne (1982), and all parameters used in the calculations were examined with respect to the sensitivity. The parameters used were

E_R=400, 660 MPa

E_L=12500, 15150 MPa

G_{LR}=500, 1000 MPa

v_{RL}=0.05

f_t=2.5, 3.5 MPa

G_F=150, 180, 210 N/m

L=25, 50, 75, 100, 150, 200 mm

σ-w curve, see Figure 4.10 and 4.11. The normal curve was a bi-linear curve with a break-point at σ/f_t=0.175 and w/w_c=0.55.

The underlined values are the "normal" values chosen. This means that when a parameter is examined, all other parameters correspond to the underlined values shown above.

4.2.2 Effect of loading arrangement

The loading point was modelled in two different ways; see Figure 4.9. In the first model the load was applied in one node immediately on the wood; see Figure 4.9a. This case is the most severe concerning plastic deformations and compression failure in the loading point. The

78

second model of the loading arrangement coincides more with reality, although not completely; see Figure 4.9b. A steel bolt was attached to all nodes in the hole of the specimen, and the load was applied in the center node of the steel bolt. These two cases yield what can be call an upper and a lower limit concerning the deformations in the loading point.

The computations with the different loading arrangements showed almost no difference. The deformation in the material around the loading point was so small that it would probably not affect the results. But this is purely theoretical. In practice there is not a perfect fitting between the steel bolt and the wood, and there are always small particles between the steel bolt and the wood. Therefore the experimentally determined curve always shows a strain hardening behaviour in the beginning of the ascending branch of the curve. In all of the following calculations the loading arrangement has been modelled as in Figure 4.9a, i.e. a load acting on one node immediately on the wood.

4.2.3 How the softening curve influences the results

Different shapes of the softening curve were used to study how the form of the curve might influence the computation and the result. When a step-wise computation is made, as described in Chapter 2, it is important to configure the mesh in such a way that numerical instabilities are avoided. In Figure 4.10 three different examples are shown of how different shape of the softening curve affects the stability of the computation. These instabilities can be avoided if a finer mesh is utilized. The more elements in the fracture process zone, the more stable computation. Another way to avoid this kind of numerical instability is to use an iterative method in the computation. However, the iterative methods are more complex, and they also consume more computer time.
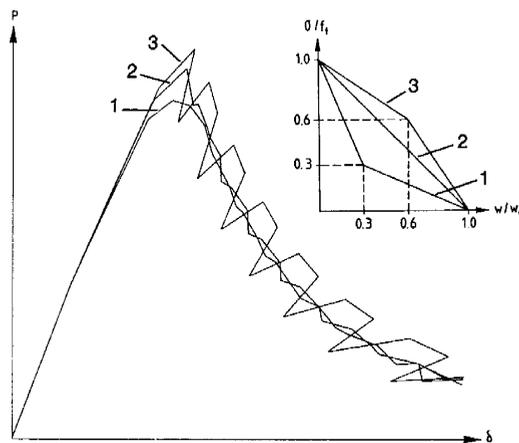
Figure 4.10 How the form of the softening curve affects the stability of the computation.

79

Three different softening curves were examined, one single-line approximation and two bi-linear approximations. These calculations were made in the beginning of the investigation concerning the CT specimen, and the FEM mesh was too coarse. The crack propagation path had only eleven nodes, and therefore the instabilities are so severe. In all other calculations the mesh was in accordance with Figure 4.9a.

The softening curve (1) is typical for wood, curve (2) is the most simple approximation and curve (3) is a typical Dugdale approximation. If the tensile strength and the fracture energy are equal for the three curves, the fracture process zone would be longest for curve (1) and shortest for curve (3). In the computation the length of the fracture process zone for curve (1) was four nodes, curve (2) two nodes and for curve (3) only one node. As Figure 4.10 shows, there are severe numerical instabilities for both the single line approximation and the Dugdale approximation. To avoid these numerical instabilities the mesh has to be made finer, i.e. a shorter distance between the nodes. A good rule is that the fracture process zone should have a length of at least five nodes.
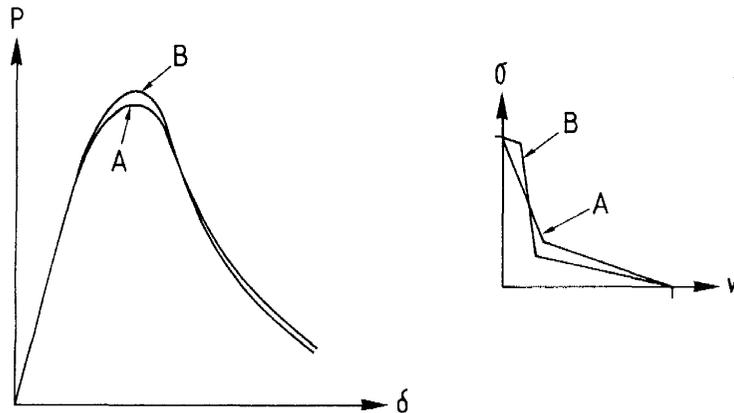
Figure 4.11 How different approximated softening curves affect the result.

Figure 4.11 presents two curves where different behaviour in the fracture process zone was assumed. As the figure indicates, the form of the softening curve can influence the result. However, this influence is rather small as long as the curve used fairly coincides with the real behaviour of the material. This means that a two line approximation is usually sufficient. However, according to Petersson (1991), the slope of the first descending branch of the softening curve is crucial. The tail, with a lower absolute value of the slope, has a rather

small effect on the result. In the case shown, the three-line approximation has a somewhat higher maximum load than the two line approximation. Otherwise the curves are almost identical.

4.2.4 How tensile strength influences the result

The tensile strength has a more dramatic effect on the computed load-displacement curve. In Figure 4.12 the effect of different values of tensile strength is shown, and as the figure indicates, the tensile strength mainly affects the maximum point of the curve. The tensile strength also affects the tail of the curve, in the sense that a higher value of the tensile strength gives a shorter tail and vice versa, but this is not shown in the figure. The values of tensile strength in this calculation were f_t=2,5 and 3.5 MPa. If only the tensile strength is altered, the shape of the softening curve changes. If the tensile strength is increased, the fracture process zone will be shorter.
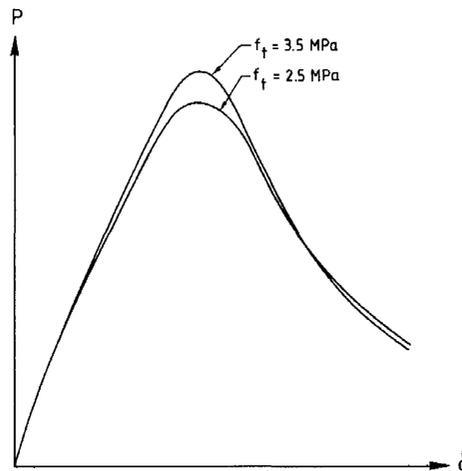
Figure 4.12 Effect of tensile strength on the calculated load-displacement curve.

4.2.5 How fracture energy influences the result

There is also, which is obvious, a clear effect of the chosen value of fracture energy on the calculated load-displacement curve. The load-displacement curves presented in Figure 4.13 are calculated with three different values of the fracture energy, G_F=150, 180 and 210 N/m. The calculations show that when the fracture energy increases, not only does the maximum point of the curve increase, but also the descending branch of the curve is affected. If the

81

fracture energy increases, the load-displacement curve will be enlarged. The enlargement of the load-displacement curve is not linearly related with the fracture energy. According to the computation the maximum load is enlarged proportionally to the fracture energy raised to 0.35, i.e. $P_{max} = const \cdot G_F^{0.35}$. This relation is probably only valid for the case studied. The effect on the fracture process zone, with respect to the fracture energy, is that higher values of fracture energy give a longer fracture process zone.
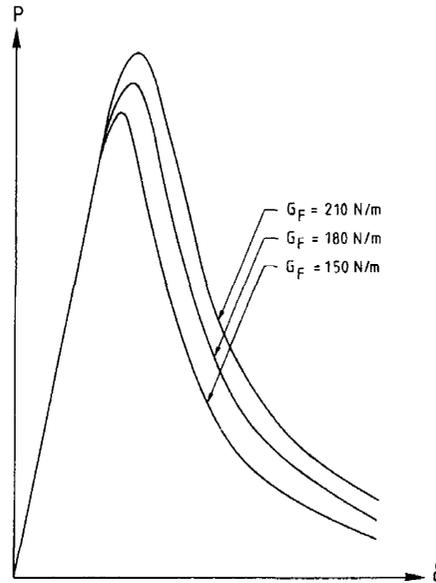
Figure 4.13 Effect of fracture energy on the computed load-displacement curve.

4.2.6 How stiffness influences the result

Another very important parameter which influences the computed load-displacement curve is the stiffness perpendicular to the grain, i.e. the stiffness in the loading direction. In Figure 4.14 two curves are drawn, valid for a modulus of elasticity in the radial direction $E_R = 400$ and 660 MPa. The stiffness perpendicular to the grain affects the slope of the load-displacement curve. A high value of the stiffness gives a steep slope of the curve, both on the ascending branch and the descending branch of the curve. This means that the tail of the curve for a specimen with a low value of the stiffness will be longer, while the tail will be shorter for a specimen with a high stiffness. The stiffness does not only influence the slope of the curve, but also affects the maximum load. The higher modulus of elasticity, the higher the load the specimen can support.

82
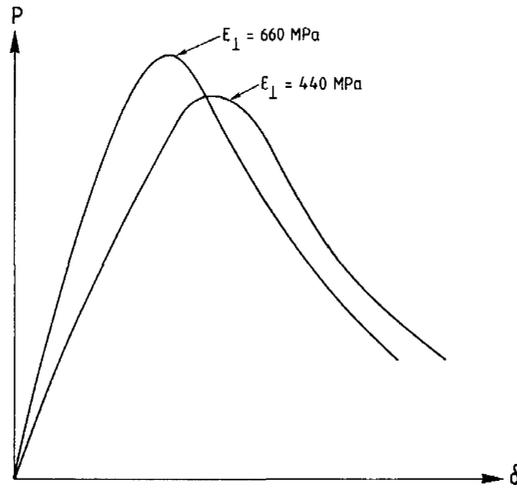
Figure 4.14 Effect of modulus of elasticity perpendicular to the grain on the load-displacement curve.

The stiffness in the grain direction has no influence at all on the computed load-displacement curve. The shear stiffness, on the other hand, has a small influence but not at all in the same proportions as the other parameters already described. Figure 4.15 displays two curves where the whole orthotropic stiffness matrix has different values. The curves are valid for a stiffness matrix [D], see equation (4.10), where $E_L = 15150$ MPa, $E_R = 660$ MPa and $G_{RL} = 500$ MPa, and for a stiffness matrix that is 11% higher, i.e. 1.11[D]. As can be seen in Figure 4.15, the effect is not especially dramatic.

$$[D^{-1}] = \begin{bmatrix} \dfrac{1}{E_L} & -\dfrac{v_{RL}}{E_R} & 0 \\[2ex] -\dfrac{v_{LR}}{E_L} & \dfrac{1}{E_R} & 0 \\[2ex] 0 & 0 & \dfrac{1}{G_{LR}} \end{bmatrix} \qquad\qquad (4.10)$$
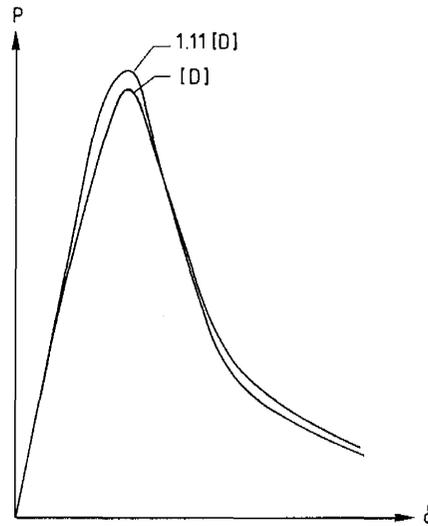
Figure 4.15 Effect of total stiffness matrix on the load-displacement curve.

4.2.7 How specimen size influences the result

It is important to know how the size of the specimen may influence the result. In this theoretical analysis six different geometries are analyzed, and all dimensions are scaled according to the ASTM standard specimen. The length to height to depth ratio is thus 1.25:1.20:0.50, and the length of the effective notch is 0.50 times the effective length. Note that the ratio of length to effective length is 1.25:1.00. The specimens examined had a total length of L=25, 50, 75, 100, 150 and 200 mm. The results are shown in Figure 4.16. Notice that the load in the diagram is made dimensionless by dividing by the ligament area of the specimens and the tensile strength used in the computation. These curves show clearly that there is a size dependency on the CT specimen with respect to the normalized maximum load.

What this calculation shows, if the fracture energy is a material parameter independent of size, is that there is a strong size dependency when stress intensity factor is measured. But as the experimental series showed, there is probably a size dependency in the fracture energy measurements, so it is difficult to draw any conclusions from these theoretical results other than that there exits a size dependency in the CT test. According to these results the influence of size is on the order of $P_{max}/A_0f_t = const \cdot L^{-0.26}$.

84
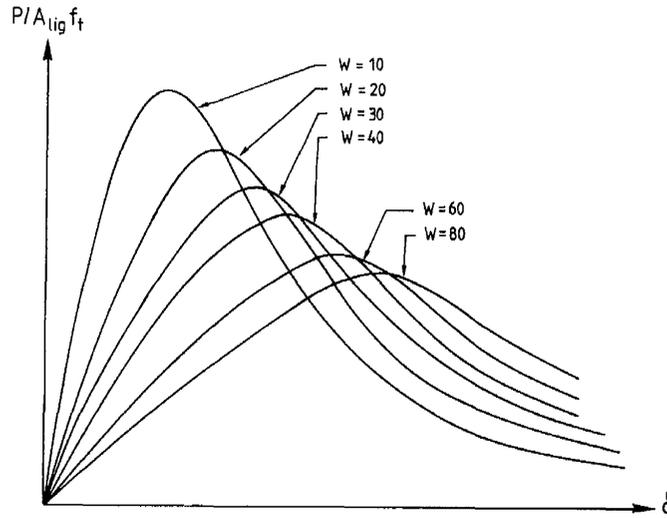
Figure 4.16 Effect on the load-displacement curve with respect to size of specimen. The load is made dimensionless by dividing by ligament area and tensile strength.

4.2.8 The effect of the sensitivity of the material parameters on the result

The sensitivity of the different parameters used in the computation can be analyzed in a normalized diagram, where we have $P_{max}/[f_t WB]$ on the y-axis and W/l_{ch} on the x-axis; see Figure 4.17. These plots are usually given in logarithmic form, Hillerborg et al. (1986), and if the plot is approximated to a straight line the following expression is obtained.

$$\frac{P_{max}}{f_t WB} = f\left(\frac{W}{l_{ch}}\right) \approx \left[\frac{Wf_t^2}{EG_F}\right]^n \tag{4.11}$$

By using the log-log relation, a sensitivity factor, n, can be calculated. If the material is linear elastic and the linear elastic fracture mechanics would be applicable, the sensitivity factor should be n = -0.5. On the other hand, if the material is linear elastic plastic the sensitivity factor should be n = 0. In this case, when the material is wood and the CT specimen is utilized, the sensitivity factor is n=-0.29.

85
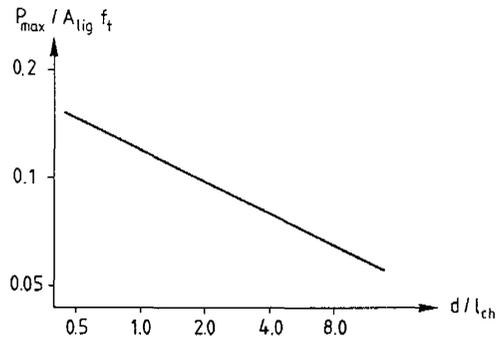
Figure 4.17 Sensitivity of the material parameters on the result.

4.2.9 Comparison between G_C and G_F

In Figure 4.18 a comparison is made between the linear elastic parameter G_C, the critical strain energy release rate, and the fracture energy G_F. The critical strain energy release rate has been calculated with equation (2.27) and with the orthotropic stiffness parameter. Thus the critical stress intensity factor has to be known, and K_{IC} has been calculated from the maximum load according to equation (4.6) in the computed load-displacement curves and without corrections of the notch length according to the fracture process zone. In the diagram in Figure 4.18 we can see that for a $W/l_{ch} > 3$ linear elastic fracture mechanics can be applied. However, in this calculation was $l_{ch} = 19$ mm, and hence the ligament length of the specimen has to be longer than 60 mm. This gives a specimen with a length of at least 150 mm. This is of course unacceptable, at least for wood perpendicular to the grain.
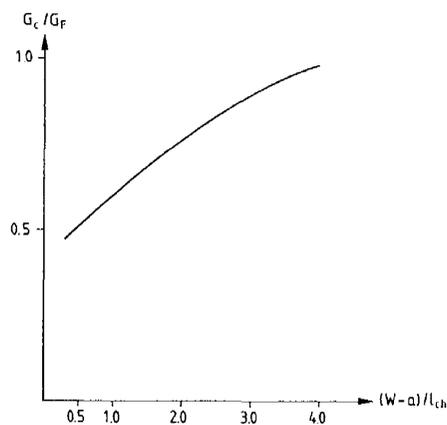
Figure 4.18 Comparison between G_C and G_F.

4.2.10 Comparison between measured and theoretically determined load-displacement curve

As previously discussed, the form of the theoretically determined load-displacement curve is influenced by fracture energy, tensile strength and modulus of elasticity perpendicular to the grain. These parameters were measured, and all other parameters used in the computation were collected from literature, Bodig and Jayne (1982). Hence the following parameters were used in the computation.

$E_L = 15000$ MPa

$E_R = 350$ MPa *

$G_{LR} = 500$ MPa

$v_{RL} = 0.05$

$f_t = 6$ MPa *

$G_F = 170$ MPa *

* measured parameters

The comparison was made on a specimen with the dimensions $50 \cdot 48 \cdot 20$ mm^3, and plane stress condition was assumed. The result from the computation is presented in Figure 4.19, where two curves are shown, one theoretical curve, obtained by the computation, and one experimentally determined curve. The experimental curve is a mean curve for all curves obtained in the experimental series with the actual geometry. The theoretical curve and the experimentally determined curve coincide very well.
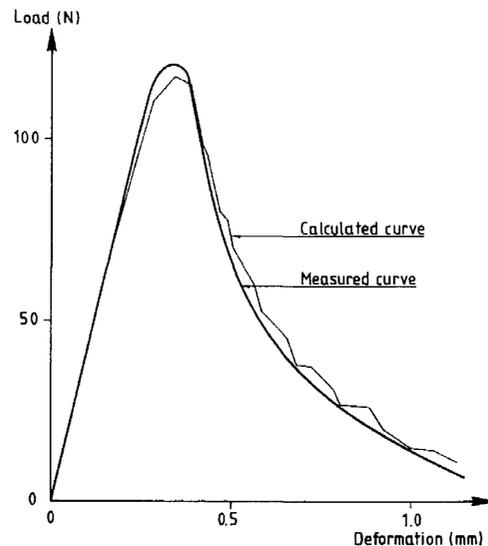
Figure 4.19 Comparison between measured and calculated load-displacement curve.

On the basis of the theoretical model utilized, the fictitious crack model, it is possible to follow the crack propagation through the material. It is also possible to determine the stress distribution along the crack propagation plane in each step of the calculation. Thus it is possible to determine the load of the specimen when a real crack, without stress transferring abilities, starts developing. In Figure 4.20 the calculated stress distribution is shown at different displacements of the specimen. The location of these stress distributions on the load-displacement curve is presented in Figure 4.21.
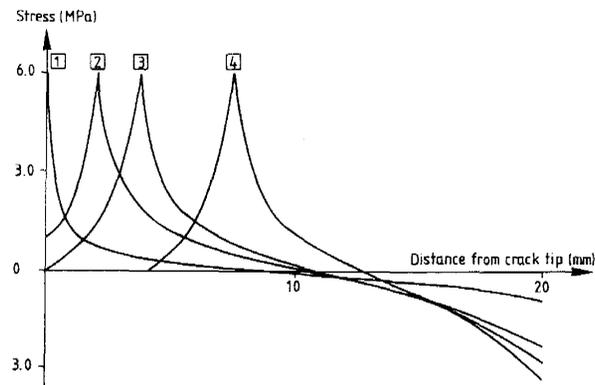
Figure 4.20 Stress distribution along the crack plane.
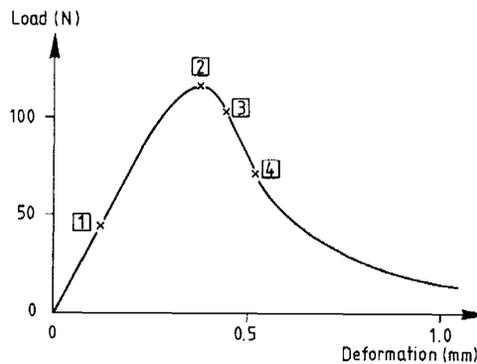
Figure 4.21 Calculated load-displacement curve.

At the tip of the notch, or crack, the theoretical stress according to the theory of elasticity approaches infinity as soon as the specimen is loaded. This means that a fracture process zone starts developing directly when the load is applied to the specimen. The theoretical analysis would also indicate this if the elements used in the calculation were infinitely small, i.e. the smaller the elements used, the closer to zero load the fracture process zone starts developing.

88

The theoretical analysis shows for the actual specimen geometry and the actual σ-w curve, that a real crack, with no stress transferring abilities, starts developing when the load is approximately 85% of the peak load on the descending branch of the curve. Accordingly there are difficulties in choosing a load for determination of the critical stress intensity factor. A correction has to be made where the length of the fracture process zone at maximum load is used.

5 Formation of drying cracks in wood

A major problem in the production of timber products is the drying process. When boards are dried, they will warp and twist depending on where in the log the boards are cut. Because of the different shrinkage in the different directions, internal stresses develop. These stresses often reach the ultimate strength of the material, and consequently cracks are formed and the quality of the board is decreased. The uneven shrinkage distribution developed is a result of two different mechanisms. Firstly the moisture distribution is uneven when the material is dried, that is, during the drying a more or less pronounced moisture content gradient develops so the moisture content increases from the surface in to the middle of the board. The second mechanism is the orthotropic behaviour of wood. The shrinkage in the radial direction differs from the shrinkage in the tangential direction. The closer to the pith the board is sawn, the greater is the risk for cracks to develop, because of the higher stresses that develop for a board sawn near the pith due to the greater curvature of the annual rings.

A classical case when cracks almost always develop, is boards sawn so that both sapwood and heartwood are located at the surface of the board, see Figure 5.1. When water migrates from the board, shrinkage occurs when the moisture content is below the fibre saturation point (FSP). In green wood the sapwood has a moisture content of much more than 100%, i.e. well over FSP, while the heartwood only has a moisture content of around 35%, i.e. on the same order as FSP. For a board with both sapwood and heartwood at the surface, shrinkage immediately starts in the heartwood, but the sapwood will stay undeformed until the moisture content reaches FSP. The sapwood will now prevent deformations in the heartwood, and consequently stresses develop. These stresses are almost always high enough for formation of cracks. In the described example cracks often develop before the boards reach the kiln, i.e. the short drying process the board goes through during the transportation from the saw mill to the kiln is enough to introduce cracks in the material.
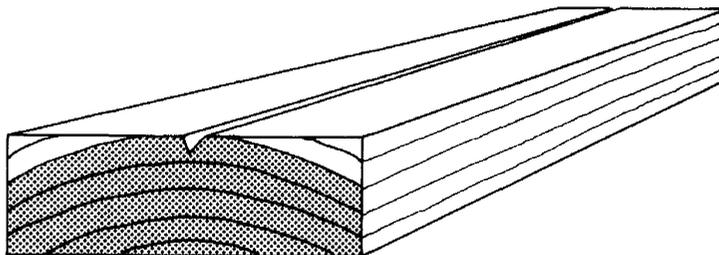
Figure 5.1 Board with both sapwood and heartwood at the surface.

Many studies of the drying process and quality changes of boards when subjected to drying have been carried out. The thesis presented by Salin (1990) gives a good overview of the theoretical improvements of the drying process, and a comprehensive literature list is presented.

The aim of the present study is to present a fracture mechanics model with which the formation and growth of cracks can be studied. Usually when development of cracks due to drying is studied, it is said that the board has cracks when the tensile strength is reached at a point in the board. But this kind of study does not say anything about how serious the damage to the board is. If the tensile strength is reached at a point in the board, a fracture process zone starts developing and a damaging process begins. The board is neither weakened nor destroyed, at least not severely damaged. But if the drying continues in such a way that the crack can grow, the quality of the board can be reduced. Therefore it is important to know the depth of the cracks a certain drying process develops. The optimum is not necessarily to avoid cracks or fracture process zones, but to dry boards without quality reductions. This probably means that a certain amount of cracks or fracture process zones can be allowed. To achieve this goal, models have to be introduced in a simulation of the drying process where the formation and progress of cracks can be studied.

The simulation presented here uses the simplest possible model to simulate the moisture movements in two dimension. Effort has been focused on the fracture process, i.e. the development and the growth of a crack due to internal stresses formed by shrinkage. This work has also previously been presented in Boström (1987a) and Boström (1987b).

5.1 Moisture content simulation

When a piece of wood is very wet, the body contains three phases of water, 1) free water, 2) water vapour and 3) bound water. When moisture is removed from the body, it is the free water that decreases first. When all the free water is gone, the bound water starts decreasing. It is the point where the free water is gone, and the bound water starts decreasing, that defines the fibre saturation point, FSP.

The amount of water a hygroscopic body can contain is expressed in the form of a sorption isotherm. This is a curve that shows what the moisture content would be if the body were in equilibrium with the surrounding air which has a certain relative humidity (RH). Figure 5.2 demonstrates an example of a sorption isotherm for Scots pine. It is important to notice that these curves change with temperature, and hence a spectrum of sorption curves is necessary when analysis is made on drying of wood with nonconstant temperature.
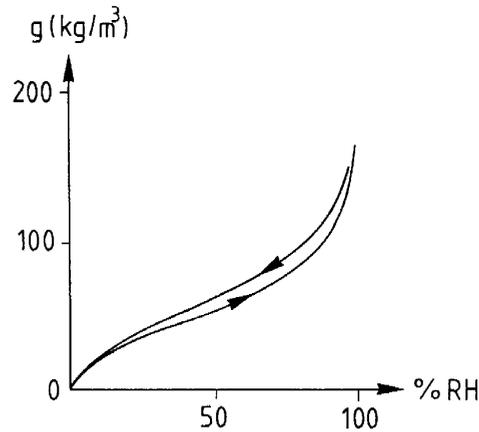
Figure 5.2 Sorption isotherm for Scots pine, Nevander and Elmarsson (1981).

The starting point of determining the physical laws that govern moisture movements in porous bodies is Fick's law. The law describes how differences in mass concentration level out due to Brownian molecular movements, i.e. diffusion. The purest form of this phenomenon is found in the gas phase. If an area contains a component in the gaseous mixture with a higher concentration than the surrounding areas, more molecules will move out from this area than into the area, and a resulting flow of molecules will start. The net flow of molecules from the area with a higher concentration is proportional to the difference in the concentration or the concentration gradient. Fick's law in one dimension can thus be formulated as

$$F = -\beta \frac{\partial g}{\partial x} \qquad (5.1)$$

where F = mass flow (kg/m²s)
β = diffusion coefficient (m²/s)
g = evaporable moisture concentration (kg/m³)
x = spatial coordinate (m)

This form of Fick's law is not suitable for calculations, so another form has to be derived. By using the law of mass conservation and introducing Fick's law in the mass conservation equation, a differential equation is obtained. This differential equation, the so-called diffusion equation, is more useful than Fick's law. The law of mass conservation for a one-dimensional case is

93

$$\frac{\partial g}{\partial t} = -\frac{\partial F}{\partial x}$$ (5.2)

where t=time

The diffusion equation in one dimension is thus

$$\frac{\partial g}{\partial t} = \frac{\partial}{\partial x}\left(\beta\frac{\partial g}{\partial x}\right)$$ (5.3)

and for a more general case in three dimensions

$$\frac{\partial g}{\partial t} = \nabla(\beta \nabla g)$$ (5.4)

where $\nabla \equiv i(\partial/\partial x) + j(\partial/\partial y) + k(\partial/\partial z)$ and i, j, k are unit vectors.

The diffusion equation does not generally describe the moisture migration. A moisture concentration gradient is not the only driving force behind moisture migration. Luikov (1966) emphasized the influence of temperature and total internal pressure on the moisture migration. However, the diffusion equation is a special case of Luikov's theory and can be utilized when flows induced by temperature and total pressure gradients can be neglected. This is the case for slow drying processes where the temperature is far below the boiling point of water. Usually for timber drying in Scandinavia these approximations can be made, so the diffusion equation can be used.

To solve the diffusion equation, appropriate boundary conditions have to be applied. The simplest approximation is that the surface of the material instantly obtains equilibrium with the surrounding air. This is of course a very rough approximation; nevertheless it has been chosen for the present calculation, that is $g(0,t) = g_1$ and $g(2d,t) = g_1$, see Figure 5.3. The initial conditions of the body were $g(x,0) = g_0$. Under these conditions the diffusion equation has been solved in one dimension. The results are shown in Figure 5.3. This solution is very approximative, not only because of the very rough boundary conditions, but also due to the diffusion coefficient which has been assumed constant, $\beta = 0.2 \cdot 10^{-6}$ m^2/s.

The diffusion coefficient is a questionable material parameter regarding theoretical simulations of the drying process. One problem is that the diffusion coefficient varies with both moisture content and temperature. There are different ways to determine the diffusion coefficient. One way is to make simulations with a theoretical model and correct the diffusion coefficient so a good fit is obtained with the measured drying curves. Another way is to experimentally

94

determine the diffusion coefficient.
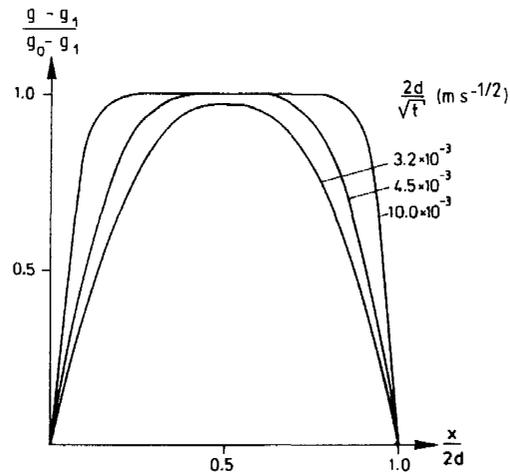
Figure 5.3 Moisture distribution at different 2d/√t, *Boström (1987a).*

One advantage of the fitting procedure for determination of the diffusion coefficient is that the errors the model may contain are usually corrected by the chosen diffusion coefficient. Another advantage is that the model will show a result that coincides with the measured drying curve. One disadvantage of the method is that many experiments and simulations are required, due to the fact that the diffusion coefficient varies with moisture content and temperature. Another disadvantage is that the obtained diffusion coefficient does not necessarily coincide with the real diffusion coefficient for the material because of errors in the model.

To experimentally determine the diffusion coefficient, there are mainly two different methods, the cup method and the sorption method. The advantage of these methods is that they give reliable results if a sufficiently big experimental series are carried out. The diffusion coefficient has been experimentally determined for different species and at different relative humidity; see for example Bertelsen (1984), where spruce was examined. The disadvantages of these experiments are that they are conducted on small clear specimens and that the conditions used in the experiments may differ from the conditions in which the final model will be used.

To conclude the moisture migration calculations presented, the following approximations have been made.

- The diffusion coefficient has been considered constant and not changing with either moisture content or temperature.
- The calculation was made in one dimension.
- The material was considered homogeneous and isotropic.
- The diffusion equation was used and the initial condition of the material was an even moisture distribution with a moisture concentration of $g(x,0) = g_0$.
- The moisture concentration in the surface of the body was assumed to instantly obtain equilibrium with the surrounding air, $g(0,t) = g_1$ and $g(2d,t) = g_1$.
- The temperature was constant.

5.2 Stress calculation

The objective of the present chapter is to present a possible technique to theoretically analyze how a crack forms and propagates in a body. The stress calculations are, however, very rough estimations due to the fact that no consideration has been given to the influence of moisture and temperature on the mechanical properties. Furthermore, no creep has been considered. However, the objective of this analyze is not to give a complete model, but to show the possibility of applying a nonlinear fracture mechanics model, the fictitious crack model, in the drying model. With the fictitious crack model development of a crack, the crack propagation and the final depth of the crack can be simulated.

Concerning stresses developed by moisture migration, a lot of different mechanisms will influence the magnitude of the stresses. The following points out some of the problems regarding stress calculations in a drying model.

The moisture content and the temperature affect a number of material properties, but it should be noted that moisture content only influences the material properties as long as it is below FSP. The modulus of elasticity decreases when moisture content increases and when temperature increases. In calculations by Thelandersson and Morén (1990), the influence of moisture dependent modulus of elasticity was examined. The relation between modulus of elasticity and moisture content was established by equation (5.5).

In the study, λ was chosen as $\lambda = 1$, i.e. a constant elastic modulus, and $\lambda = 3$, i.e. an elastic modulus that depends on moisture content. According to their investigation, no pronounced difference was found on the restraint stress during drying between these two cases.

96

$$E(u) = E_f \left[1 + (\lambda - 1)\frac{u_f - u}{u_f} \right] \qquad (5.5)$$

where u = moisture content

    u_f = moisture content at fibre saturation point

    E_f = modulus of elasticity for $u \geq u_f$ (green material)

    λE_f = modulus of elasticity for u=0

The strength of the material also decreases with increasing moisture content, but the most dramatic effect is in the longitudinal direction of the fibres, and the variations of strength in the other directions are minor.

A drying process usually takes a comparatively long time, and thus the long-time behaviour is of importance. The mechanism accentuated here is creep. It should be noted that the following is not included in the calculations presented. According to the literature, Salin (1990), the mechano-sorptive creep is the major creep, and thus viscoelastic and plastic creep can be excluded. The creep in one dimension is described with the following constitutive equation, Salin (1990):

$$\frac{\partial \epsilon}{\partial t} = C \frac{\partial \sigma}{\partial t} + \frac{\partial \epsilon_v}{\partial t} + (\alpha + m\sigma)\frac{\partial g_b}{\partial t} \qquad (5.6)$$

where ϵ = total strain

    t = time (s)

    σ = tensile stress (Pa)

    C = compliance (Pa^{-1})

    ϵ_v = viscoelastic strain

    α = unrestrained shrinkage coefficient (m^3/kg)

    m = mechano-sorptive creep coefficient ($m^3/kgPa$)

    g_b = bound water content (kg/m^3)

According to equation (5.6), the total creep strain is divided into three additive and independent parts. The first term is the pure elastic instantaneous response. The second term is a time-dependent viscoelastic creep that can be expressed by some rheological model, for instance, Maxwell's, Kelvin's or Burger's equations. The third term consists of two parts, of which the first part describes the normal shrinkage or swelling below FSP, and the second part describes the mechano-sorptive creep.

Another important mechanism regarding development of stresses is the difference between "free" shrinkage and shrinkage under load. According to Thelandersson (1991) there is a big

difference between "free" shrinkage, where the specimen can deform freely, and a shrinkage where stress develops and prevents the deformations. It is therefore unrealistic to make pure elastic calculations. Thelandersson (1991) suggests that a good approximation would be to assume that the "free" shrinkage due to drying, used in the calculations, is around 10% of the real shrinkage in practice. This would give a fair representation of stresses developed in the material. Unfortunately this fact was discovered only after the calculations were made, and therefore the "free" shrinkage is utilized in the following.

The "free" shrinkage, ψ, is approximately linear with the moisture content below FSP. Above FSP is there no shrinkage; see Figure 5.4. The shrinkage can thus be calculated by the relation

$$\psi = \psi_{max} \frac{u_0 - u_1}{u_f} \qquad (5.7)$$

where u_0 = moisture content at the start of the drying process

u_1 = moisture content at the end of the drying process

u_f = moisture content at FSP

ψ_{max} = "free" shrinkage when dried from FSP to $w_b = 0$
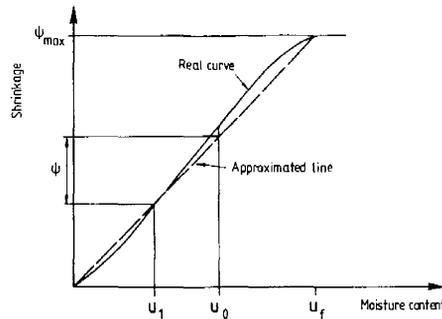
Figure 5.4 Shrinkage versus moisture content. The dotted line is the approximated linear relation.

The maximal shrinkage, ψ_{max}, i.e. the shrinkage developed when dried from green condition to completely dry, varies in the orthotropic directions and for species. In Table 5.1 the maximal shrinkage is assembled for some different species, Kollman (1951). The table shows that the shrinkage in the tangential direction is twice as high as in the radial direction. The shrinkage in the longitudinal direction is very small compared with the other two directions. However, the modulus of elasticity in the longitudinal direction can be up to twenty-five times higher than perpendicular to the grain, and thus large stresses can develop in the longitudinal

98

direction even if the shrinkage is much smaller. The modulus of elasticity is also presented in Table 5.1.

Table 5.1 Shrinkage coefficient and modulus of elasticity for different species, Kollman (1951).

Species	Shrinkage			E-module	(MPa)
	Tangen-tial	Radial	Longitu-dinal	Longitu-dinal	Perpen-dicular
Ash	8.0 %	5.0 %	0.2 %	13400	1100
Birch	7.8 %	5.3 %	0.6 %	16500	800
Beech	11.8 %	5.8 %	0.3 %	16000	1500
Oak	7.8 %	4.0 %	0.4 %	11700	1000
Pine	7.7 %	4.0 %	0.4 %	12000	460
Spruce	7.8 %	3.6 %	0.3 %	11000	550

Note once more that in the calculations presented no creep is included, and all material parameters are assumed independent of moisture content. By using the moisture distribution in Figure 5.3 and equation (5.7), a shrinkage, or internal strain, distribution is calculated. When calculating the shrinkage, the material has been assumed isotropic and the shrinkage coefficient has been equal in the two dimensions. And as for the moisture distribution, the internal strain distribution is calculated at different times in the drying process. The internal strain distribution is then used as prescribed "load" in the finite element calculations. The internal strain distribution is shown in Figure 5.5.
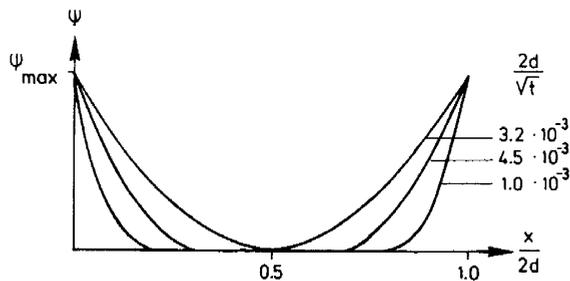
Figure 5.5 Internal strain as a function of depth in the specimen.

In the computation a specimen with the dimensions 2d·2h=44·64 mm² has been examined; see Figure 5.6. In the computation two symmetry lines have been used; hence only one quarter of the complete specimen has been examined. Along the shortest symmetry line, see Figure 5.6, the crack is supposed to propagate, and therefore "crack" elements are used at this line. The element mesh is presented in Figure 5.7, and the spring elements shown are the so-called "crack" elements.
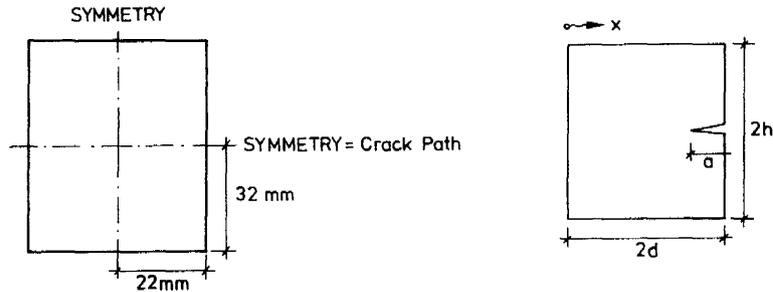
Figure 5.6 Specimen geometry.
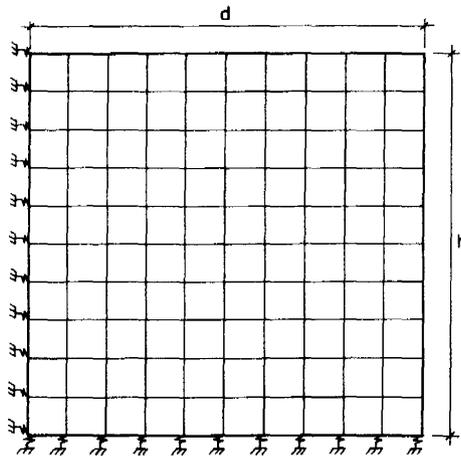
Figure 5.7 Element mesh.

To simulate crack propagation, a fracture mechanics model has to be utilized. In this study the fictitious crack model has mainly been used, but some results are presented where the linear elastic fracture mechanics has been employed. In this computation both the σ-ϵ-curve and the σ-w-curve were approximated by a straight line, see Figure 5.8, and the material properties used were chosen as follows

100

f_t = 3 MPa

E = 460 MPa

v = 0.015

thickness = 1 m

G_F = 360 N/m

ψ_{max} = 5%
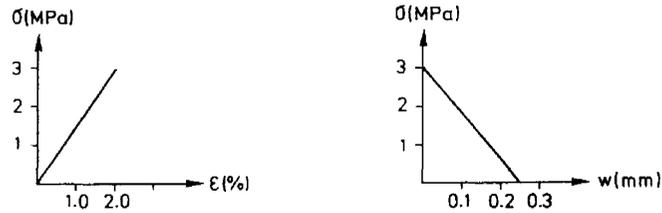
Figure 5.8 σ-ε curve and σ-w curve used in calculations.

FEM calculations were made for different internal strain distributions, corresponding to different time in the drying process. In that way, and if a suitable fracture mechanics model is coupled to the stress calculations, it is possible to simulate a crack propagating into the body.

5.3 Results

The usual result from a drying model is a drying schedule for the kiln. Nevertheless, here the results are presented in a completely different way, as the depth of the developed crack.

When the tensile strength of the material is reached at a point, a fracture process zone start developing. As a result cracks can be classified as real cracks or as fracture process zones. A real crack has no stress transferring abilities, in contrast to the fracture process zone which can transfer stresses. In the fracture process zone the material is somewhat destroyed, but in practice a fracture process zone is harmless. A fracture process zone can never be localized visually, due to its invisible nature, i.e. you can never see a fracture process zone.

In Figure 5.9 the depth of the developed crack is presented as a function of the shrinkage, ψ, in the specimen. The shrinkage, on the y-axis, is the free shrinkage corresponding to a change in moisture content from u_1 to u_0. This means, or represents, a climate change that gives a total shrinkage ψ. Notice that two curves are plotted in the figure. The continuous line represents a real crack with no stress transferring abilities, and the dotted line represents the

101

depth where a fictitious crack starts.
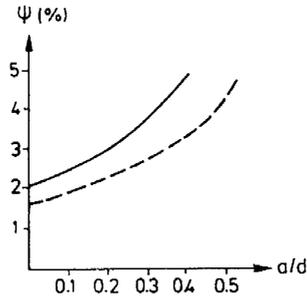
Figure 5.9 Normalized depth of a crack, a/d, when subjected to drying corresponding to a shrinkage, ψ. The dotted line shows where in the body the fracture process zone starts.

Figure 5.9 shows, for the actual specimen, that a real crack will develop if the climate conditions are so chosen that the shrinkage is greater than 2%. For instance, if the shrinkage is 3%, the crack developed in the specimen due to the shrinkage has a depth of a/d=0.20. According to the symmetry of the specimen, two cracks develop, one on each side of the specimen. The depth of each crack is thus a=0.20·22=4.4 mm.

However, even if no real crack has developed in the material, it is possible that a fracture process zone develops. According to Figure 5.9, a fracture process zone starts developing when the total shrinkage is 1.6%. For a shrinkage of 2%, when the real crack starts propagating, the depth of the fracture process zone is a/d=0.13, i.e. 6.5% of the total specimen width on each side of the specimen.

In Figure 5.10 the results are presented in another way. On the x-axis is the relative humidity in the material at the start of the drying process. And on the y-axis is the developed depth of a real crack with no stress transferring abilities. The curves in the figure represent different relative humidity in the environment.

According to Figure 5.10 the relative humidity in the environment cannot be less than 85% if no cracks are to develop in a wet specimen. The figure also shows that the most severe part of the drying is at the high relative humidities, when the moisture gradient is steepest.

102
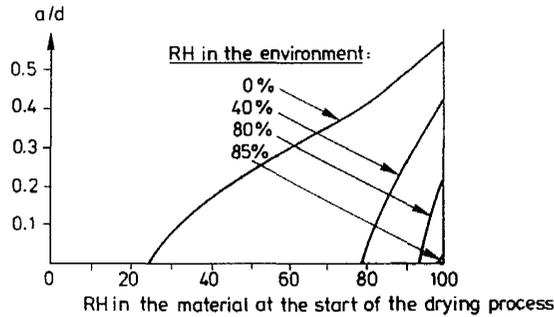
Figure 5.10 Crack depth for drying in different conditions.

Regarding wood and fracture mechanics, the most widely used model is linear elastic fracture mechanics. A comparison has been made between linear elastic fracture mechanics and the fictitious crack model. One disadvantage of linear elastic fracture mechanics is that the model cannot be utilized on bodies without an initial crack, or with very short cracks. When simulating drying, it is obvious that the material is free of cracks in the initial stage, and therefore linear elastic fracture mechanics cannot be used. However, a comparison has been made and the results are presented in Figure 5.11.
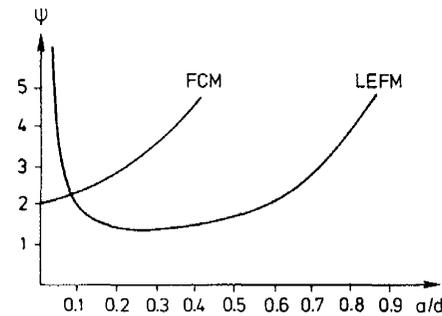
Figure 5.11 Comparison between LEFM and FCM.

As Figure 5.11 shows, a strong singularity can be found for LEFM due to the lack of crack. However, if an initial crack is assumed, LEFM can be used. According to Figure 5.11, there is a big difference between the two models regarding the length of the developed crack. One explanation is that in this small specimen, the developed fracture process zone is relatively long and a significant part of the potential energy is stored in the fracture process zone.

103

Another important aspect is the size dependency. The size dependency is a well-known phenomenon for researchers involved in fracture mechanics. Calculations have been made for specimens of different sizes, and the results are presented in Figure 5.12. The results show that the relative depth of the crack increases with increasing dimensions of the specimen, especially for small and normal dimensions.
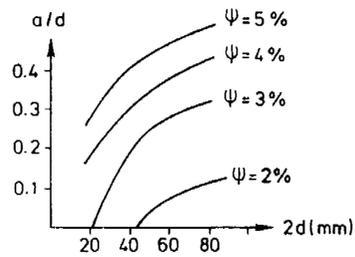
Figure 5.12 How size of specimen influences the relative depth of the crack.

6 Conclusions and future research

It is possible by means of direct tension or shear tests to determine the complete stress displacement relation for Scots pine. There are, however, a number of factors that can spoil the experiment. The complete experiment has to be stable, in order to determine both the right form of the curve and the fracture energy. The test can be unstable both regarding translation and rotation, and in order to avoid these instabilities the specimen has to be very short and the testing arrangement has to have a sufficient stiffness, regarding both translation and rotation.

The specimens have been glued into the testing arrangement, and the glue could affect the result in different ways. If the glue was not strong enough, the failure would occur in the glueline. Another problem was the curing time of the glue. For the epoxy utilized, a curing time of at least three hours had to be applied. Otherwise there could be plastic deformations in the glueline.

The complete stress displacement curve was determined for specimens conditioned in four different climates and for specimens with different grain orientation, RL, TL and one orientation between RL and TL. It was found that the normalized stress displacement relation for the fracture process zone, the σ/f_t-w/w_c curve, was independent of both moisture content and orientation of the grain, i.e. the curve had the same shape for all series. However, the moisture content in the specimens was in a very narrow range, except for one series, and accordingly it would be interesting to make a larger experimental series, where the effect of moisture content on the softening behaviour could be determined.

All experiments regarding the softening behaviour were made on specimens taken from only one board, and thus they are not representative for Scots pine. Therefore it would be of interest to examine a more representative material, and also to determine the behaviour for other species.

The softening behaviour is necessary when utilizing the fictitious crack model, which is a nonlinear fracture mechanics model. In order to show the applicability of the fictitious crack model, two different specimens have been analysed. One is the CT specimen, which is one of the most commonly used specimens for determination of fracture mechanics properties. The other specimen is a piece of wood exposed to drying, and thus the formation and growth of drying cracks have been analysed.

Regarding the CT specimen, both an experimental and a theoretical examination were made. These investigations showed that linear elastic fracture mechanics cannot directly be

adopted to small specimens. Futhermore, it was demonstrated that with the fictitious crack model, it is possible to theoretically determine the behaviour of a specimen. Accordingly, the fictitious crack model is an extraordinary tool for examination of specimens for determination of material properties such as fracture energy or stress intensity factors. Today, there exists no standard method for determination of fracture mechanics properties of wood, and consequently, if fracture mechanics is to be utilized by wood researchers in the future, there is a large demand of standardised methods. Here the fictitious crack model can be very useful.

One of the largest problems regarding wood today is the drying process. It has been shown in the present study that it is possible with fracture mechanics and the fictitious crack model, to theoretically determine the crack formation and propagation during drying. However, there is still a lot of research needed before the complete drying process can be theoretically simulated, but the fictitious crack model is a suitable tool for the fracturing simulation.

106

Appendix A Experimental results, Mode I

Num	RH	Ligament (mm^2)	Load$_{max}$ (kN)	f_t (MPa)	G_F (N/m)	E (MPa)	K_{IC} kNm$^{-3/2}$	Notes
T0145	58	12.6·20.1	0.708	2.8	485	640	560	
T0245	58	12.4·19.8	1.216	4.9	630	570	600	
T0345	58	12.4·20.0	0.683	2.8	745	460		Glue
T0445	58	12.6·19.8	0.728	2.9	785	490		Glue
T0545	58	12.6.19.8	1.512	6.0	445	900	630	
T0645	58	12.5·20.2	1.437	5.7	450	1010	680	
T0745	58	12.4·19.6	1.487	6.1	380	1060	630	
T0845	58							Glue
T0945	58	12.4·19.8	1.603	6.5	700	990	830	
T1045	58							Instable
T1145	58	12.3·19.8	2.055	8.4	1175	1470	1310	Glue
Mean	58			5.3	515	765	660	
s.d.				1.4	125	250	90	
T0195	58	12.4 19.6	1.181	4.8	580	710	640	
T0295	58							Instable
T0395	58	12.5·20.0	0.828	3.3	500	460	480	
T0495	58							Mistake
T0595	58	12.8·20.0	1.286	5.0	585	1120	810	
T0695	58	12.6·20.1	0.909	3.6	470	660	560	
T0795	58	12.8·20.3	1.211	4.6	490	710	590	
T0895	58	12.6·20.0	0.994	4.0	375	950	600	
Mean	58			4.2	500	770	610	
s.d.				0.7	75	230	110	
T0105	58	12.9·20.1	0.849	3.3	295	800	490	
T0205	58	12.6·20.0	0.919	3.6	565	680	620	
T0305	58	12.5·20.0	1.181	4.7	325	860	530	

Num	RH	Ligament	$Load_{max}$	f_t	G_F	E	K_{IC}	Notes
T0405	58	12.4·20.1	1.236	4.9	450	780	590	
T0505	58	13.0·20.0	1.121	4.3	405	650	510	
T0605	58	12.6·20.0	1.909	7.6	615	1340	910	
T0705	58	12.6·20.1	1.055	4.2	380	870	580	
T0805	58	12.8·20.2	1.201	4.7	390	620	490	
T0905	58	12.8·20.2	1.120	4.3	335	550	430	
T1005	58	12.6·19.9	0.989	4.0	375	260	310	
T1105	58	13.0·19.8	1.698	6.6	615	1030	790	
T1205	58							Glue
T1305	58							Glue
T1405	58	12.9·20.0	1.231	4.8	520	520	520	
T1505	58	12.8·20.2	1.176	4.6	495	480	490	
T1605	58	12.8·20.1	1.317	5.1	560	820	680	
T1705	58	12.5·20.2	1.532	6.0	435	1020	670	
T1805	58	12.6·20.3	1.794	7.0	510	760	620	
T1905	58	12.6·20.0	1.231	4.9	270	830	470	
Mean	58			5.0	445	760	570	
s.d.				1.2	110	250	140	
T0143	33	12.2·20.1	1.256	5.1	390	750	540	
T0243	33	12.6·20.0	1.472	5.9				Instable
T0343	33	12.4·20.0	1.663	6.7	645	1070	830	
T0443	33	12.4·19.9	0.935	3.8	405	530	460	
T0543	33	12.5·19.9	0.754	3.0	270	660	420	
T0643	33	12.5·20.0	1.447	5.8	435	1000	660	
T0743	33	12.4·19.8	1.829	7.4	425	1540	810	
T0843	33							Instable
T0943	33	12.9·20.0	1.563	6.1	700	850	770	
T1043	33	12.8·19.7	1.211	4.8	375	1030	620	
T1143	33	12.3·19.8	1.311	5.4	610	720	660	
T1243	33	12.2·19.8	1.316	5.4	600	670	630	
T1343	33	12.8·20.2	1.020	4.0	370	650	490	

Num	RH	Ligament	Load$_{max}$	f_t	G_F	E	K_{IC}	Notes
Mean	33			5.3	475	860	630	
s.d.				1.2	140	290	140	
T0193	33							Instable
T0293	33	12.5·20.1	0.362	1.4	410	100	200	Glue
T0393	33	12.8·20.0	1.005	3.9	470	540	500	
T0493	33							Mistake
T0593	33	12.9·20.0	1.156	4.5	530	870	680	
T1093	33	12.8·19.9	1.000	3.9	635	670	650	
T1193	33	12.9·20.1	1.030	4.0	560	670	610	
Mean	33			4.1	550	690	610	
s.d.				0.3	70	140	80	
T0103	33	12.8·20.0	1.346	5.2	590	930	740	
T0203	33							Glue
T0303	33	12.5·20.1	1.100	4.4	285	900	500	
T0403	33	12.9·19.8	0.960	3.8	385	630	490	
T0503	33	12.8·19.7	1.618	6.4	390	1060	640	
T0603	33	12.8·20.1	1.174	4.5	395	500	440	
T0703	33	12.9·20.0	1.261	4.9	550	840	680	
T0803	33	12.9·20.2	1.271	4.9	430	710	550	
T0903	33	12.9·20.0	1.236	4.8	470	720	580	
T1003	33							Glue
T1103	33	12.9·20.1	1.286	5.0	440	840	610	
T1203	33	12.8·20.3	1.201	4.7	595	630	610	
T1303	33	12.4·20.0	2.010	8.1	310	1520	690	
T1403	33	12.4·20.0	1.372	5.5	420	1050	660	
T1503	33	12.8·20.0	1.638	6.4	710	1090	880	
T1603	33	12.8·20.1	1.407	5.5	460	960	670	
Mean	33			5.3	460	880	620	
s.d.				1.1	115	260	110	
T0108	75	13.0·20.2	1.065	4.1	465	710	570	
T0208	75							Glue

Num	RH	Ligament	Load$_{max}$	f_t	G_F	E	K_{IC}	Notes
T0308	75							Glue
T0408	75	12.9·20.4	1.306	5.0	540	800	660	
T0508	75	12.8·20.4	1.417	5.4	405	760	560	
T0608	75	12.9·20.5	1.552	5.9	545	870	690	
T0785	75							Machine
T0885	75	12.8·20.3	1.346	5.2	510	640	570	
T0908	75	12.9·20.4	0.970	3.7	550	620	580	
T1008	75							Mistake
T1108	75							Mistake
T1208	75							Glue
T1308	75	12.8·20.2	0.955	3.7	545	590	570	
T1408	75	12.4·20.4	1.020	4.0	560	360	450	
T1508	75							Machine
T1608	75	12.9·20.2	1.075	4.1	560	640	600	
T1708	75	12.8·20.7	1.296	4.9	785	530	650	
T1808	75	12.8·20.5	1.025	3.9	430	520	470	
T1908	75							Glue
Mean	75			4.5	535	640	580	
s.d.				0.8	100	140	70	
T0148	75	12.9·20.2	1.030	3.9	510	510	510	
T0248	75	12.8.20.2	1.105	4.3	660	520	590	
T0348	75	12.8.20.0	1.261	4.8	865	1020	940	
T0448	75	12.9·20.6	1.156	4.4	420	770	570	
T0548	75	12.8·20.4	1.025	3.9	480	710	580	
T0648	75	12.7·20.4	1.226	4.7	565	630	600	
T0748	75	12.9·20.3	1.281	4.9	610	640	630	
T0848	75	12.8·20.3	1.326	5.1	635	560	600	
Mean	75			4.5	595	670	630	
s.d.				0.5	135	170	130	
T0198	75	13.0·20.4	0.964	3.7	540	460	500	
T0298	75	12.8·20.3	0.970	3.7	420	610	510	

110

Num	RH	Ligament	Load$_{max}$	f$_t$	G$_F$	E	K$_{IC}$	Notes
T0398	75	12.8.20.4	1.020	3.9	390	540	460	
T0498	75	12.8·20.5	1.226	4.7	605	660	630	
T0598	75	12.9·19.9	0.960	3.8	320	480	390	
T0698	75	12.8·20.2	1.075	4.2	495	620	550	
Mean s.d.	75			4.0 0.4	460 105	560 80	510 80	
T1309	97	10.6·20.6	0.635	2.9	545	850	680	
T1409	97	10.3·21.0	1.515	7.0	420	990	640	
T1509	97	10.6·21.1	0.985	4.4	505	560	530	
T1609	97	10.3·21.2	1.025	4.7	485	580	530	
T1709	97	10.1·20.8	0.860	4.1	550	990	740	
T1809	97	10.8·21.0	1.000	4.4	535	740	630	
T1909	97	10.2·21.0	0.580	2.7	475	550	510	
T2009	97	10.4·20.8	0.850	3.9	485	625	550	
T2209	97	10.4·21.0	0.770	3.5	585	470	520	
T2309	97	10.4·21.0	0.715	3.3	555	690	620	
Mean s.d.	97			4.1 1.2	515 50	700 180	600 80	

Note : The digit before the last digit in the specimen name represents the orientation as follows

0 = RL orientation
4 = 45° orientation
9 = TL orientation

Appendix B Moisture and density measurements

Num	Volum dry (10^{-5}m³)	Weight dry (10^{-3}kg)	Weigth dry (10^{-3}kg)	Weight H$_2$O (10^{-3}kg)	Density $\rho_{0,0}$ (kg/m³)	Moisture content (%)
			33% RH			
31	7.362	36.958	34.375	2.583	467	7.51
32	7.349	37.924	35.295	2.629	480	7.45
33	7.344	35.559	33.040	2.519	450	7.62
34	7.228	35.229	32.740	2.489	453	7.60
35	7.186	33.923	31.511	2.412	439	7.65
36	7.176	33.546	31.139	2.407	434	7.73
Mean					454	7.59
s.d.					17	0.10
			59% RH			
51	7.097	35.464	32.319	3.145	455	9.73
52	7.237	38.870	35.453	3.417	490	9.64
53	7.327	38.818	35.372	3.446	483	9.74
54	7.521	37.762	34.418	3.344	458	9.71
55	7.433	37.098	33.807	3.291	455	9.73
56	7.452	38.537	35.131	3.406	471	9.70
Mean					469	9.71
s.d.					15	0.04
			75% RH			
71	7.267	41.741	36.668	5.073	505	13.84
72	7.379	39.501	34.667	4.824	470	13.91
73	7.304	40.001	35.123	4.878	481	13.89
74	7.266	38.092	33.436	4.656	460	13.93

75	7.224	38.344	33.691	4.653	466	13.81
76	7.361	37.150	32.596	4.554	443	13.97
Mean					471	13.81
s.d.					21	0.06

			97% RH			
91	7.401	39.600	31.239	8.361	422	26.76
92	7.259	39.098	30.895	8.203	426	26.55
93	7.358	44.873	35.518	9.355	483	26.34
94	7.467	43.358	34.259	9.099	459	26.56
95	7.414	44.076	34.915	9.161	471	26.24
96	7.375	45.179	35.704	9.475	484	26.54
Mean					458	26.50
s.d.					28	0.18

Appendix C Results obtained with the Compact Tension specimen

Name	u	Rings	$\rho_{0,13}$	G_F	$K_{IC,ortho}$	$K_{IC,iso}$	$K_{IC,Eq4.2}$	$K_{IC,Fons}$
80401	13.0	15	382	212	320	343	333	321
80402	13.0	13	387	220	314	336	326	311
80403	13.3	9	389	246	320	343	333	313
80404	13.2	12	405	194	320	343	333	320
80405	13.5	8	411	255	325	348	338	332
80406	13.7	15	394	235	304	326	316	307
Mean	13.3		395	227	317	340	330	317
s.d.	0.3		11	23	7	8	8	9
80301	12.5	14	381	209	405	413	421	377
80302	12.7	13	405	185	318	341	330	316
80303	12.8	9	405	218	346	371	360	352
80304	13.1	11	394	231	314	336	326	315
80305	13.4	13	408	235	326	349	338	325
80306	13.6	11	409	242	296	317	308	295
Mean	13.0		400	220	334	358	347	330
s.d.	0.4		11	21	38	41	40	30
60301	13.4	8	407	182	245	263	255	243
60302	13.1	11	402	217	322	345	335	327
60303	13.2	11	398	186	336	360	349	345
60304	13.2	10	388	180	298	319	310	304
60305	13.2	14	398	191	298	319	310	302
60306	13.4	13	395	189	259	278	269	267
Mean	13.2		398	191	293	314	305	298
s.d.	0.1		7	14	35	37	37	38

114

60201	13.2	12	444	240	298	319	310	303
60202	12.8	9	442	239	287	307	298	287
60203	12.7	10	444	235	340	364	353	352
60204	12.3	7	470	225	291	311	302	293
60205	12.9	13	446	210	291	311	302	298
60206	12.8	12	475	232	292	313	304	298
Mean	12.8		454	230	300	321	312	305
s.d.	0.3		15	11	20	22	21	24
40201	12.2	23	417	168	323	346	336	329
40202	12.1	24	416	156	356	381	370	328
40203	12.2	21	413	163	347	371	360	278
40204	12.0	24	425	185	358	383	372	331
40205	12.2	26	407	167	323	346	336	274
40206	12.2	25	413	150	347	371	360	296
Mean	12.2		415	165	342	366	356	306
s.d.	0.1		6	12	16	17	16	27
40101	13.6	25	399	141	296	317	307	302
40102	13.7	16	420	95	365	391	379	363
40103	13.7	17	420	178	365	391	379	365
40104	13.4	26	419	177	351	376	365	353
40105	13.7	15	419	255	365	398	379	358
40106	13.6	31	400	198	328	351	341	337
Mean	13.6		413	174	345	371	358	346
s.d.	0.1		10	54	28	31	29	24

20101	14.5	12	407	210	281	301	292	285
20102	14.1	8	391	230	363	388	377	373
20103	14.4	7	392	222	353	378	367	363
20104	14.1	8	391	219	327	350	340	334
20105	14.6	9	386	275	353	378	367	348
20106	14.0	10	394	234	340	364	353	348
20107	14.6	8	384	242	274	294	285	272
Mean	14.3		392	233	327	350	340	332
s.d.	0.3		7	21	36	38	37	39

Note: Name represents the specimen number. The first two digits represents the ligament length plus the length of the effective notch, i.e. W+a. The third and fourth digit represents the width of the specimen and finally the last digit represents the number of the specimen in each series.

Rings represents the number of rings per centimeter on the specimen where the notch is made.

$\rho_{0,13}$ represents density (kg/m^3)

G_F represents fracture energy (N/m)

$K_{IC,ortho}$ represents fracture toughness calculated by equation 4.4 (kNm$^{-3/2}$)

$K_{IC,iso}$ represents fracture toughness calculated by equation 4.5 (kNm$^{-3/2}$)

$K_{IC,eq4.2}$ represents fracture toughness calculated by equation 4.2 (kNm$^{-3/2}$)

$K_{IC,Fons}$ represents fracture toughness calculated by Fonselius method (kNm$^{-3/2}$)

Appendix D Additional measurements for the analysis of the CT specimen

| Specimen	Modulus of elasticity in tension E_{tens} (MPa)	Modulus of elasticity in compression E_{comp} (MPa)	Tension strength f_t (MPa)	Compression strength f_c (MPa)
40104			5.8	
40105			6.2	
40106			4.1	
40201	220	490		5.5
40202	220			
-"-	200			
40203	210	265		5.4
60201	240	320		5.8
60202	200	160		4.8
60203	130	340		7.1
60301	160			
60302	90			
60303	100			

Appendix E Experimental results, Mode II

Specimen	Shear strength f_v (MPa)	Fracture energy $G_{F,II}$ (N/m)	Note
S01	12.6	1210	
S02	10.2	850	
S03	10.4	1520	
S04			Glue
S05	10.9	650	
S06	9.6	640	
S07	11.0	760	
S08	10.9		Instable
S09			Double crack
S10			Double crack
S11	10.7	800	
S12	11.5	740	
S13	11.0		Instable
S14	11.5	1070	
S15	10.9	820	
S16	12.6	960	

Appendix F Measurements for detection of rotational instability

The following diagrams are stress-displacement relations, i.e. σ-δ curves. In each figure three curves are drawn representing stress-displacement relations measured on both sides of the specimen and a mean value measured by two clip-gauges, one on each side of the specimen.
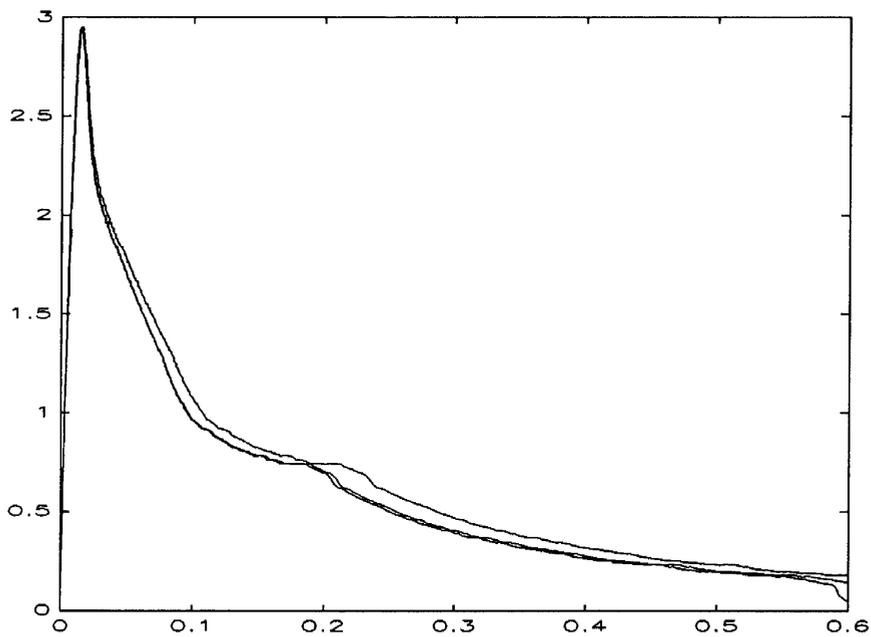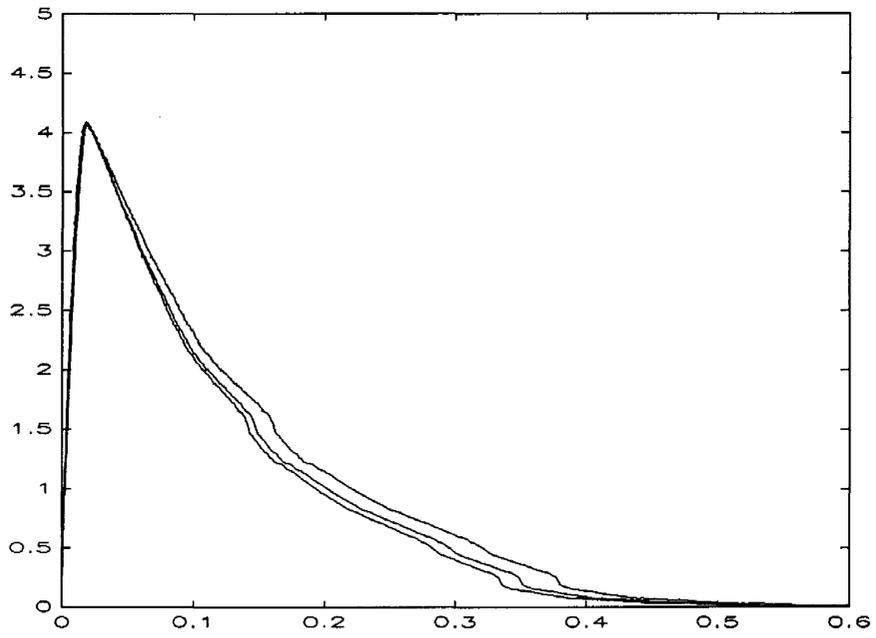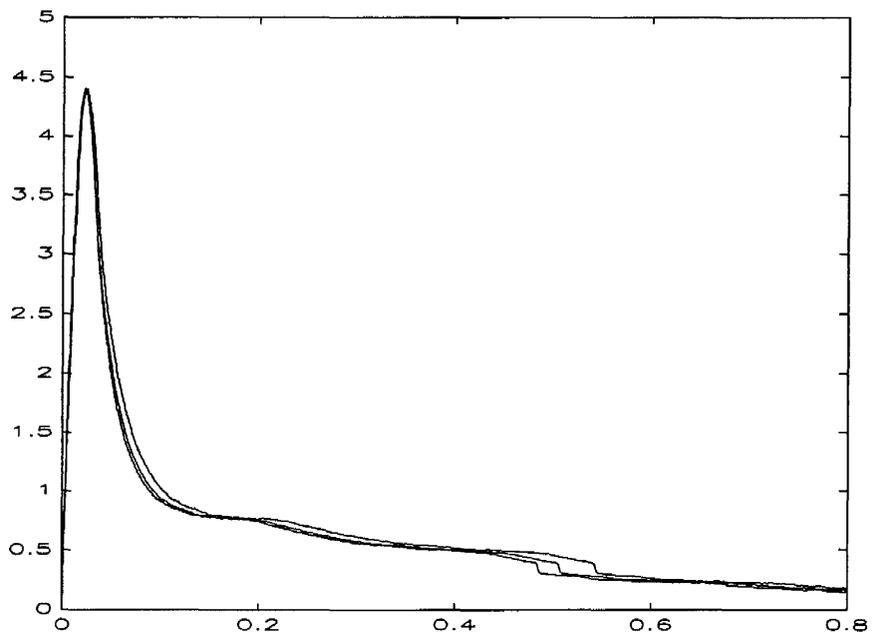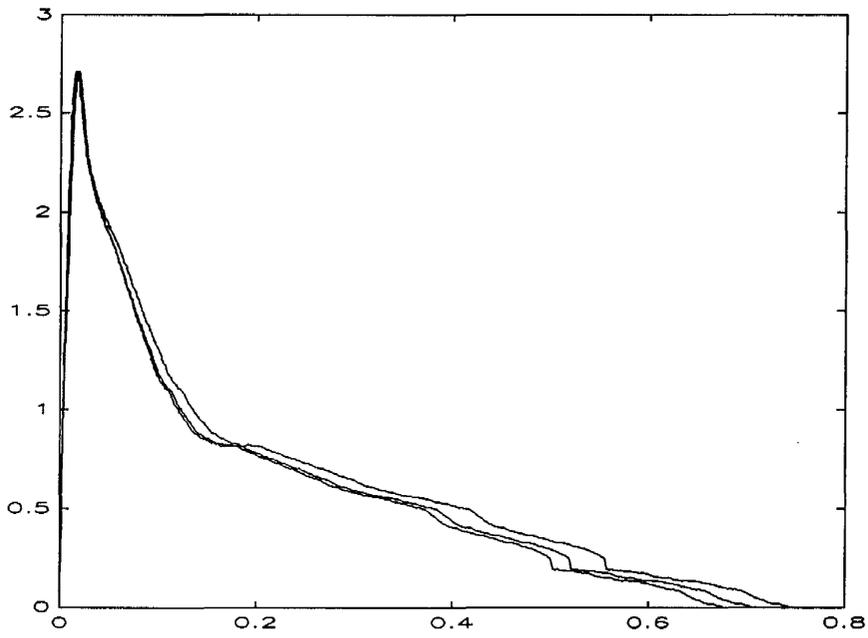

Specimen T1309
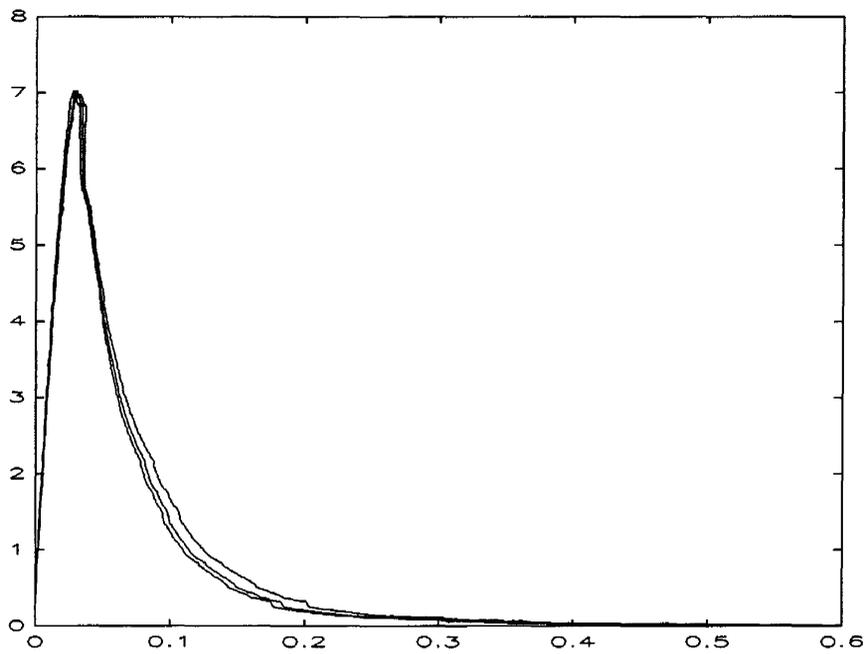
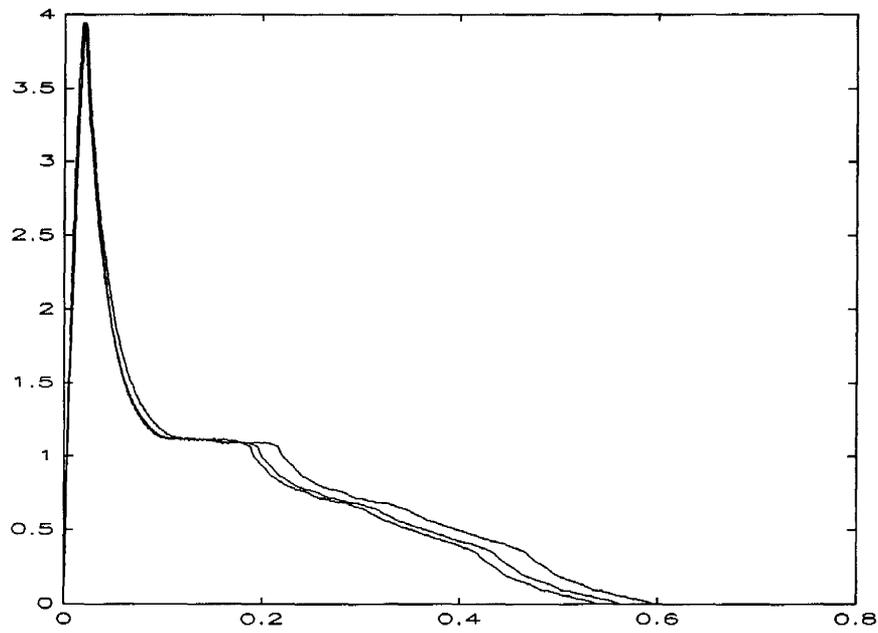Specimen T1409
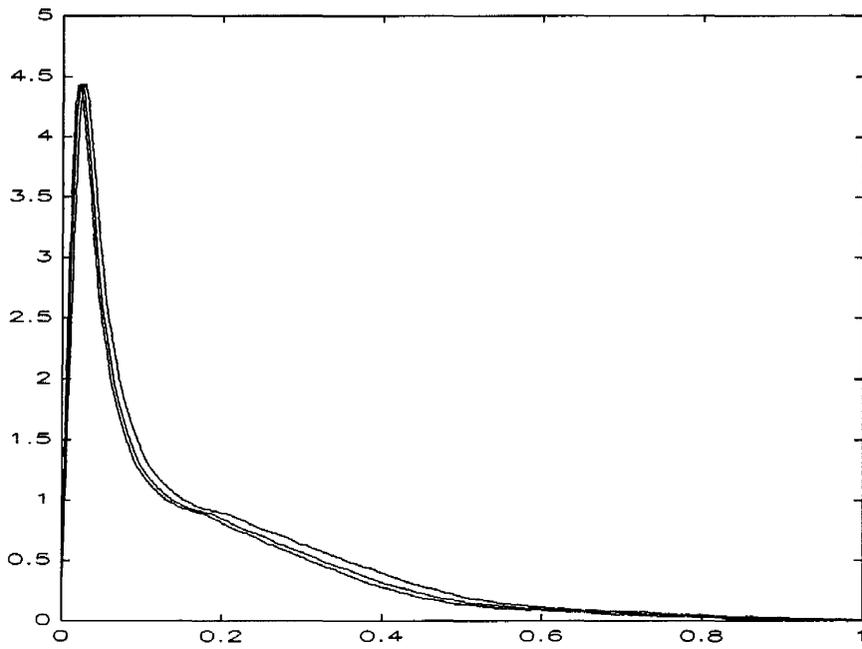
Specimen T1509
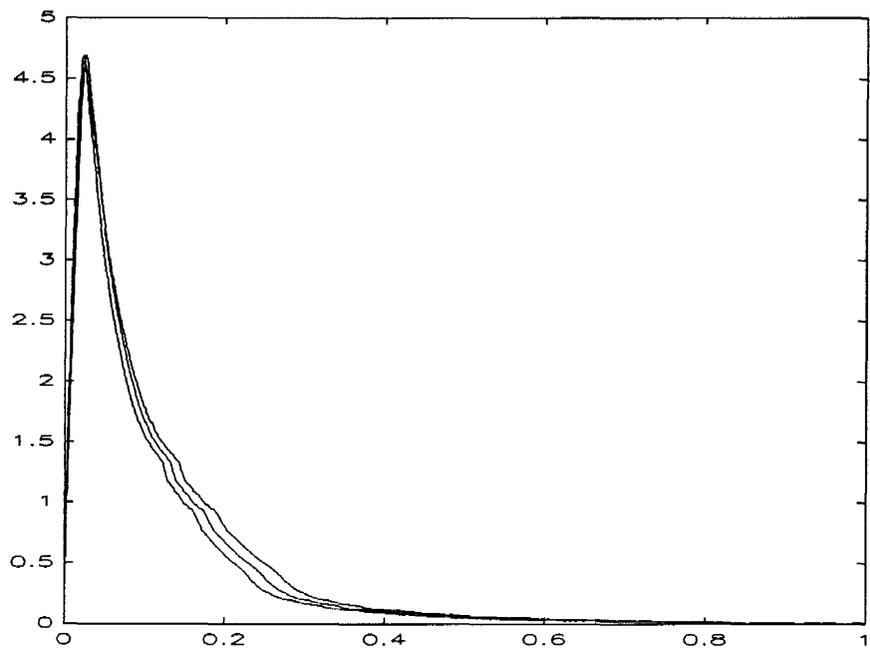
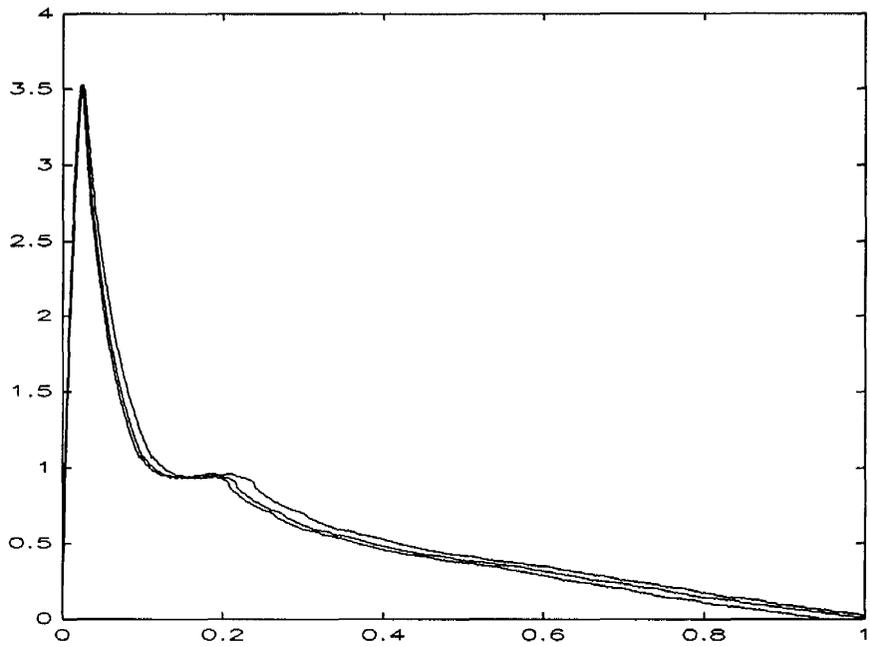Specimen T1609

Specimen T1709

Specimen T1809

Specimen T1909

Specimen T2009

Specimen T2209

References

Aronsson C-G. (1984) "Tensile fracture of composite laminates with holes and cracks", Report No 84-5, Dep of Aeronautical Structures and Materials, The Royal Institute of Technology, Stockholm, Sweden

ASTM 399-81 (1981) "Standard test method for plane strain fracture toughness of metallic materials", Am. Soc. for Test. and Mater.

Bertelsen N.H. (1984) "Diffusionsmålning med kopmetoden på rödgran. (Measurements of diffusion coefficients with the cup-method on spruce.)", Report No 129/83, Dept. of Civ. Eng., Building Materials Lab., Tech. Univ. of Denmark, (in Denish)

Bodig J., Jayne B.A. (1982) "Mechanics of wood and wood composites", Van Nostrand Reinhold Company, New York, USA

Boström L. (1987a) "Analysis of shrinkage cracks in wood by means of fracture mechanics", Report TVBM-3027, Lund Inst. of Tech., Sweden

Boström L. (1987b) "The fictitious crack model applied on shrinkage cracks in wood", Proc. Stress development and degrade during wood drying, Sept. 28 - Oct. 2, Skellefteå, Sweden

Boström L. (1990) "The Compact Tension test used on wood - an analysis of a testing method", IUFRO 5.02 Meeting, Saint John, Canada

Bäcklund J. (1982) "Fracture mechanics", Skrift 82-18, Royal Institute of Technology, Stockholm, Sweden (in Swedish)

Carlsson J. (1976) "Fracture mechanics", Ingenjörsförlaget (in Swedish)

Dahlblom O., Peterson A., Petersson H. (1985) "Manual to CALFEM", Div. of Struct. Mech., Lund Inst. of Tech., Sweden, (in Swedish)

Dugdale D.S. (1960) "Yielding of steel sheets containing slits", J. of Mech. Phys. Solids, Vol 8, pp. 100-104

Eshelby J.D. (1956) Solid State Phys., Vol 3, pp. 79-144

Ewing P.D., Williams J.G. (1979) "Thickness and moisture content effect in the fracture toughness of Scots pine", J. of Material Science, No 14, Vol 12

Fonselius M. (1986) "Fracture mechanics of spruce and PLV" Report 80, Div. of Structural Engineering, Helsinki University of Technology, Espoo, Finland (in Swedish)

Griffith A.A. (1921) "The phenomena of rupture and flow in solids", Trans. Royal Soc London, Vol 221

Gustafsson P.J. (1985) "Fracture mechanics studies of nonyielding materials like concrete", Report TVBM-1007, Lund Inst. of Tech., Sweden

Hassanzadeh M., Hillerborg A., Zhou F. (1987) "Tests of material properties in mixed mode I and II", SEM/RILEM Int. Conf. on Fracture of Concrete and Rock

Heilmann H.G., Hilsdorf H.H., Finsterwalder K. (1969) "Festigkeit und verformung von beton unter zugspannungen", Deutscher Ausschuss für Stahlbeton, Heft 203, W. Ernst & Sohn, Berlin

Hellan K. (1984) "Introduction to fracture mechanics", McGraw-Hill Book Company

Hillerborg A., Modéer M., Petersson P.E. (1976) "Analysis of crack formation and crack growth in concrete by means of fracture mechanics and finite elements", Cem. and Concr. Res., Vol 6, pp. 773-782

Hillerborg et al. (1983) "Building materials, basic course", Div of Building Materials, Lund Institute of Technology, Lund, Sweden (in Swedish)

Hillerborg et al. (1986) "Building materials, advanced course", Div of Building Materials, Lund Institute of Technology, Lund, Sweden (in Swedish)

Hillerborg A. (1989) "Stability problems in fracture mechanics testing", Fracture of Concrete and Rock, Elsevier Applied Acience, pp 369-378

Inglis C.E. (1913) "Stresses in a plate due to presence of cracks and sharp corners", Trans. Inst. Nav. Archit., Vol 55, p 163-241

Irwin G.R. (1958) "Fracture", pp 551-590 in Encyclopedia of Physics, vol 6, Springer, Berlin

Knott J.F. (1973) "Fundamentals of fracture mechanics", Butterworths, London

Kollman F. (1951) "Technologie des holzes und der holzwerkstoff", Second ed., Springer-Verlag

Kretschmann D.E., Green D.W., Nelson W.J. (1990) "The effect of moisture content on Mode I fracture toughness in Southern pine", IUFRO 5.02 Meeting, Saint John, Canada

Landelius J. (1989) "Finite area method", Div. of Struct. Mech, Lund Inst. of Tech., Sweden, (in Swedish)

Larsen H.J., Gustafsson P.J. (1990) "The fracture energy of wood in tension perpendicular to the grain - results from a joint testing project", CIB-W18A, Meeting 23, Lisbon, Portugal

Luikov A.V. (1966) "Heat and mass transfer in capillary-porous bodies", Pergamon Press

Masuda M. (1988) "Theoretical consideration on fracture criteria of wood - proposal of finite small area theory", Int. Conf. on Timber Eng. Seattle, Vol 2, pp. 584-595

MATLAB for 80386-based MS-DOS Personal Computers (1990), The Math Works Inc, South Natick, USA

Nevander L.E., Elmarsson B. (1981) "Fukthandboken (The moisture handbook)", Sweden, (in Swedish)

Palm J. (1991) Personal communication

Petersson H. (1991) Personal communication

Petersson P.E. (1981) "Crack growth and development of fracture zones in plain concrete and similar materials", Report TVBM-1006, Lund Inst. of Tech., Sweden

Petterson R.W., Bodig J. (1983) "Prediction of fracture toughness of conifers", Wood an Fibre Science, Vol 15, no 4

Rice J.R. (1968) "Path independent integral and approximate analysis of strain concentration by notches and cracks", J. of Applied Mechanics, Transactions, ASME, Vol 35, pp. 379-386

RILEM (1985) "Determination of the fracture energy of mortar and concrete by means of three-point bending test on notched beams", Materials and Structures, Vol 18, No 106, pp. 285-290

Riipola K., Fonselius M. (1988) "Evaluation of critical J-integral for wood material", Report 528, VTT, Espoo, Finland (in Swedish)

Rolfe S.T., Barsom J.M. (1977) "Fracture and fatique control in structures. Applications of fracture mechanics." Prentice-Hall, New Jersey

Salin J.G. (1990) "Simulation on the timber drying process. Prediction of moisture and quality changes", Ekono Oy, Helsinki, Finland

Sih G.C., Paris P.C., Irwin G.R. (1965) "On cracks in rectilinearly anisotropic bodies", Int. J. of Fracture Mechanics, Vol 1, pp. 189-203

Smith I., Chui Y.H. (1991) "Mode I fracture energy of plantation-grown Red pine", 1991 Int. Timber Engineering Conf., London, England

Thelandersson S., Morén T. (1990) "Tensile stresses and cracking in drying timber", IUFRO/5.02 Timber Engineering Meeting, New Brunswick, Canada

Thelandersson S. (1991) Personal communication

Valentin G., Boström L., Gustafsson P-J., Ranta-Maunus A. and Gowda S. (1991) "Application of fracture mechanics to timber structures RILEM state-of-the-art report", Research Note 1262, VTT, Espoo, Finland

Valentin G. (1991) Personal comunication.

Valentin G., Adjanohoun G. (1991) "Applicability of classical isotropic fracture mechanics specimens to wood crack propagation", to be published

Walsh P.F. (1972) "Linear fracture mechanics in orthotropic materials", Eng. Fract. Mech., Vol. 4, pp. 533-541.

Wright K., Fonselius M. (1987) "Fracture mechanics testing of wood. Methods for Mode I and Mode II", 1st RILEM Int. Congr.